

**NUMERICAL AND ANALYTICAL MODELING OF
SANDING ONSET PREDICTION**

A Dissertation

by

XIANJIE YI

Submitted to the Office of Graduate Studies of
Texas A&M University
in partial fulfillment of the requirements for the degree of

DOCTOR OF PHILOSOPHY

August 2003

Major Subject: Petroleum Engineering

**NUMERICAL AND ANALYTICAL MODELING OF
SANDING ONSET PREDICTION**

A Dissertation

by

XIANJIE YI

Submitted to Texas A&M University
in partial fulfillment of the requirements
for the degree of

DOCTOR OF PHILOSOPHY

Approved as to style and content by:

Peter P. Valkó
(Co-Chair of Committee)

James E. Russell
(Co-Chair of Committee)

W. John Lee
(Member)

Dimitris C. Lagoudas
(Member)

Hans C. Juvkam-Wold
(Head of Department)

August 2003

Major Subject: Petroleum Engineering

ABSTRACT

Numerical and Analytical Modeling of Sanding Onset Prediction. (August 2003)

Xianjie Yi, B.S.; M.S., Southwest Petroleum Institute

Chair of Advisory Committee: Dr. Peter P. Valkó

Dr. James E. Russell

To provide technical support for sand control decision-making, it is necessary to predict the production condition at which sand production occurs. Sanding onset prediction involves simulating the stress state on the surface of an oil/gas producing cavity (e.g. borehole, perforation tunnel) and applying appropriate sand production criterion to predict the fluid pressure or pressure gradient at which sand production occurs. In this work, we present numerical and analytical poroelastoplastic stress models describing stress around producing cavity and verify those models against each other. Using those models, we evaluate the stress state on the cavity surface and derive sanding onset prediction models in terms of fluid pressure or pressure gradient based on the given sand production criterion. We then run field case studies and validate the sanding onset prediction models.

Rock strength criterion plays important roles in sanding onset prediction. We investigate how the sanding onset prediction results vary with the selection of one or another rock strength criterion. In this work, we present four commonly used rock strength criteria in sanding onset prediction and wellbore stability studies: Mohr-Coulomb, Hoek-Brown, Drucker-Prager, and Modified Lade criteria. In each of the criterion, there are two or more parameters involved. In the literature, a two-step procedure is applied to determine the parameters in the rock strength criterion. First, the Mohr-Coulomb parameters like cohesion S_0 and internal friction angle ϕ_f are regressed from the laboratory test data. Then, the parameters in other criteria are calculated using the regressed Mohr-Coulomb

parameters. We propose that the best way to evaluate the parameters in a specific rock strength criterion is to perform direct regression of the laboratory test data using that criterion. Using this methodology, we demonstrate that the effect of various rock strength criteria on sanding onset prediction is less dramatic than using the commonly used method. With this methodology, the uncertainties of the effect of rock strength criterion on sanding onset prediction are also reduced.

ACKNOWLEDGEMENTS

I would like to thank my advisors Dr. Peter P. Valkó and Dr. James E. Russell for directing my Ph.D. study at Texas A&M University. Their scientific approach toward research taught me to be a serious scholar. I would like to express my gratitude to Dr. James E. Russell for generously providing financial support for my study. Without that, my study here would have been impossible. I would like to thank Dr. W. John Lee for being my committee member. I also benefited a lot from many courses taught by him. I thank him for teaching me to think in physics in addition to mathematics. I thank also Dr. Dimitris C. Lagoudas for serving on my committee. His plasticity course elevated my understanding of solid mechanics and is fully used in my dissertation.

As an international graduate student in the Department of Petroleum Engineering, I appreciate Dr. Thomas A. Blasingame and Ms. Eleanor Schuler for organizing lots of extracurricular activities for graduate students. They gave us a sense of family.

I appreciate Mr. Joseph A. Ayoub of Schlumberger for providing me an internship opportunity. His trust in me and his willingness to teach me knowledge will be missed.

I thank my officemates Javier Franquet, Orlando Zambrano and Serguei Jourine for sharing their knowledge with me and encouraging our mutual interests in rock mechanics.

I appreciate my wife and my parents for their constant and unconditional support, without which, it would have taken much longer or even been impossible to pursue and finish my doctoral study.

TABLE OF CONTENTS

	Page
ABSTRACT	iii
ACKNOWLEDGEMENTS	v
TABLE OF CONTENTS	vi
LIST OF FIGURES.....	ix
LIST OF TABLES	xii
CHAPTER	
I INTRODUCTION.....	1
1.1 Statement of the problem	1
1.2 Objectives of this research	1
1.3 Summary of results.....	2
II LITERATURE REVIEW	4
2.1 Sand arch stability	4
2.2 Perforation tunnel stability	7
2.3 Open hole stability	9
2.3.1 Analytical axisymmetrical plane strain model	9
2.3.2 Analytical 2D plane strain model	10
2.3.3 Numerical model	11
2.4 Sand production criterion	11
2.4.1 Tensile failure.....	12
2.4.2 Shear failure and rock strength criterion	12
2.4.3 Pore collapse	13
III ANALYTICAL MODELS FOR SANDING ONSET PREDICTION	16
3.1 Analytical model for wellbore/perforation tunnel failure induced sand production-Isotropic in-situ stress case	16
3.1.1 Poroelasticity solution and shear failure sanding criterion	17
3.1.2 Poroelastoplasticity solution and tensile failure sanding criterion	19
3.2 Analytical model for wellbore/perforation tunnel failure induced	

CHAPTER	Page
sand production-Anisotropic in-situ stress case.....	22
3.3 Analytical model for perforation tip failure induced sand production.....	26
3.3.1 Poroelasticity solution and shear failure sanding criterion	26
3.3.2 Poroelastoplasticity solution and tensile failure sanding criterion	27
IV NUMERICAL MODEL FOR SANDING ONSET PREDICTION	30
4.1 3D stress model	30
4.2 3D transient fluid flow model	31
4.3 Mohr-Coulomb plasticity	32
4.3.1 Mohr-Coulomb in terms of stress invariants.....	32
4.3.2 Flow rule.....	34
4.3.3 Elastoplastic stress-strain matrix.....	34
4.4 Finite element solution to the 3D stress model	36
4.5 Finite element solution to the 3D fluid flow model	37
4.6 Verification of the numerical models.....	37
4.6.1 Verification of the 3D fluid flow model.....	37
4.6.2 Verification of the 3D stress model.....	43
4.7 Comparison of numerical model and analytical model.....	47
4.8 Uncertainty assessment of sanding onset prediction model.....	50
V EFFECT OF ROCK STRENGTH CRITERION ON SANDING ONSET PREDICTION	54
5.1 Rock strength criterion	56
5.1.1 Mohr-Coulomb criterion	56
5.1.2 Hoek-Brown criterion	57
5.1.3 Drucker-Prager criterion	58
5.1.4 Modified Lade criterion	61
5.2 Near wellbore poroelastic stress model.....	61
5.3 Determination of rock strength criterion parameters	62
5.4 Application of rock strength criterion in sand production prediction	68
VI SANDING ONSET PREDICTION CASE STUDIES.....	75
6.1 Sand production in gas fields in the Northern and Central Adriatic Sea	75
6.2 Sand production in Well #3	84
VII SUMMARY AND CONCLUSIONS.....	90
NOMENCLATURE.....	92

	Page
REFERENCES	98
APPENDIX A	107
APPENDIX B	118
APPENDIX C	120
APPENDIX D	125
APPENDIX E.....	128
VITA	132

LIST OF FIGURES

FIGURE	Page
2.1 Sand arch near perforation	5
2.2 Grid system used by Morita <i>et al.</i>	8
2.3 Normalized failure envelope for sandstone.....	14
2.4 Complete Mohr-Coulomb failure envelope including pore collapse	15
2.5 Drucker-Prager elliptic cap model	15
3.1 Dimensionless critical drawdown plot assuming Poisson's ratio=0.3	19
3.2 Comparison of shear failure induced sanding criterion and tensile failure induced sanding criterion	22
3.3 Anisotropic in-situ stress around a borehole	23
3.4 Dimensionless critical drawdown plot for different stress anisotropy ratio-Assuming Poisson's ratio=0.3, $\sigma_h(t)=C_o$	25
3.5 Comparison of critical drawdown values for shear failure induced sanding from perforation tunnel and perforation tip	28
4.1 Finite element grid used in simulation of single well production from a closed axisymmetrical reservoir	39
4.2 Comparison of pressure and pressure derivative curves for single well production from an closed axisymmetrical reservoir	40
4.3 Finite element grid used in simulation of single well production from a closed rectangular reservoir.....	42
4.4 Comparison of pressure and pressure derivative curves for single well production from a closed rectangular reservoir.....	43
4.5 Comparison of 3D finite element solution with analytical solution for stress state near wellbore during production	44
4.6 Principal effective stresses along radial direction 63.75° to x coordinate.....	45

FIGURE	Page
4.7 Principal effective stresses around wellbore for anisotropic in-situ stress case with fluid flow.....	46
4.8 Boundary condition and grid used in finite element simulation of near wellbore stress.....	48
4.9 Comparison of stress state simulation results after 150 days of production using analytical and numerical models.....	48
4.10 Relative error of stresses using analytical model.....	49
4.11 Histogram for the predicted critical bottom hole flowing pressure @ $P_{avg}=2500$ psi.....	52
4.12 Cumulative frequency distribution for the predicted critical bottom hole flowing pressure @ $P_{avg}=2500$ psi.....	53
5.1 Comparison scheme in Chapter V.....	55
5.2 Mohr-Coulomb strength criterion.....	57
5.3 Failure envelopes projected on the π -plane for Mohr-Coulomb criterion, circumscribed Drucker-Prager criterion, inscribed Drucker-Prager criterion and Drucker-Prager middle circle.....	60
5.4 Pressure change with time during gas production.....	70
5.5 Wellbore surface principal effective stresses change with production time assuming linear elasticity.....	70
5.6 Predicted sanding onset results using different rock strength criteria for rock data in Case A & B, with rock strength parameters from Tables 5.2 and 5.4 respectively.....	72
5.7 Predicted sanding onset results using different rock strength criteria for test data in Case A, with rock strength parameters from Table 5.3	73
5.8 Predicted sanding onset results using different rock strength criteria for rock test data in Case B, with rock strength parameters from Table 5.5	74
6.1 The Northern Adriatic Basin.....	76

FIGURE	Page
6.2 Comparison of predicted and field measured BHFP at sanding onset assuming perforation tunnel or perforation tip shear failure induced sanding	80
6.3 Gas density and pressure correlation in a wide pressure range.....	81
6.4 Gas density and pressure correlation in a narrower pressure range	81
6.5 Predicted and field measured BHFP at sanding onset assuming perforation tip tensile stressed induced sanding.....	82
6.6 Comparison of predicted critical BHFP and field measured BHFP for 23 wells with sand production.....	83
6.7 Comparison of predicted critical BHFP and field measured BHFP for 8 wells without sand production.....	84
6.8 Logging data for well #3	85
6.9 Predicted and field measured BHFP at sanding onset assuming perforation tip tensile stressed induced sanding.....	87
6.10 Comparison of predicted and field measured BHFP at sanding onset assuming perforation tunnel or perforation tip shear failure induced sanding.....	88

LIST OF TABLES

TABLE	Page
4.1 Well, reservoir and production parameters - Case 1	38
4.2 Well, reservoir and production parameters - Case 2	41
4.3 Rock mechanics parameters used in comparison study	44
4.4 Minimum, mean and maximum values for Poisson's ratio, UCS and in-situ horizontal stress	51
5.1 Assumed rock strength test data points	63
5.2 Strength criterion parameters for Case A-Derived from regressed Mohr-Coulomb S_o and ϕ_f	64
5.3 Strength criterion parameters for Case A- Calculated directly from the two assumed test data points	65
5.4 Strength criterion parameters for Case B-Derived from regressed Mohr-Coulomb S_o and ϕ_f	66
5.5 Strength criterion parameters for Case B- Calculated directly from the two assumed test data points	67
5.6 Well, reservoir and production parameters used in studying the effect of rock strength criterion on sand production	69
6.1 Northern Adriatic gas wells where sand production was observed under the given condition	76
6.2 Northern Adriatic gas wells where sand production was not observed under the given condition	78

CHAPTER I

INTRODUCTION

1.1 Statement of the problem

Sand production is the production of sand particles during the producing of oil/gas. It poses some disadvantages such as erosion to surface and downhole tubulars, fire hazard to gas wells. Generally sand production is not desirable and sand control facilities are installed to prevent sand production. Since sand control is generally an expensive investment for an oil/gas operator, it is of great interests for the operator to estimate if sand control is needed before production, or when sand control is needed after some time of sand-free production. To provide technical support for sand control decision-making, it is necessary to predict the production condition at which sand production occurs. This forms the research topics in this dissertation.

1.2 Objectives of this research

The objectives of this research are:

- To develop numerical and analytical models which can be used to predict the onset of sand production for oil and gas wells.
- To study the effect of rock strength criterion on sanding onset prediction.
- To use those models to explain some field sanding problems such as production of sand after some time of sand-free production.

This dissertation follows the style and format of the *SPE Journal*.

1.3 Summary of results

Through this research, we accomplish the following:

- We derive an analytical poroelastoplastic stress model for thick-walled hollow cylinder model. Based on the thick-walled hollow cylinder model, we derive simple sanding onset prediction models assuming shear failure induced sanding and tensile stress induced sanding after shear failure. These models may be used to study sanding from open-hole well or perforation tunnel for cased well.
- We derive an analytical poroelastoplastic stress model for thick-walled hollow sphere model. Based on the thick-walled hollow sphere model, we derive simple sanding onset prediction models assuming shear failure induced sanding and tensile stress induced sanding after shear failure. These models may be used to study sanding from perforation tip for cased well.
- We derive an analytical poroelastic stress model for thick-walled hollow cylinder model under anisotropic in-situ stress condition. Based on this model, we derive sanding onset prediction model assuming shear failure induced sanding. This model may be used to study sanding from open-hole wells where the in-situ horizontal stresses are different.
- We implement a 3D general finite element code for stress state simulation and single-phase fluid flow simulation. Its technical performance is checked against available analytical and numerical solutions.
- We study the effect of rock strength criterion on sanding onset prediction. We propose that the best way to evaluate the rock strength criterion parameters is to perform direct regression of the laboratory test data. Using the regressed Mohr-Coulomb parameters to calculate the rock strength parameters in the other criteria is not recommended. Using this methodology, the uncertainties of the effect of rock strength criterion on sand production prediction are reduced.

- We study the Northern Adriatic Basin wells sanding cases. Through this study, we conclude that sand production in Northern Adriatic Basin wells might be because of induced tensile stress at perforation tip after shear failure. We validate this conclusion by wells without sand production problem under the given conditions. Case study of sanding problem in Well#3 indicates that sanding might be caused by shear failure at perforation tip. Using this assumption, we reached perfect agreement between predicted and field measured bottom hole flowing pressure at sanding onset.

CHAPTER II

LITERATURE REVIEW

Sanding onset prediction is generally based on sand arch instability¹⁻¹⁰, perforation tunnel instability¹¹⁻¹⁵, or vertical, horizontal or deviated borehole instability¹⁶⁻³⁰. Generally, a stress model is established to obtain the stress state near the sand arch, perforation tunnel or borehole, and then a sand production criterion is applied to predict the stress state or fluid flow condition at which sand production occurs. Post-sanding behavior has also been studied to quantify the amount of sand produced³¹⁻³⁵.

Numerous factors such as rock mechanical properties, in-situ stress state, wellbore/perforation geometry, pressure drawdown, pressure depletion, and water cut may influence sand production. Many efforts have been made to study the effect of those parameters. The final goal of these efforts is to know when sand production occurs and how much sand will be produced. The following paragraphs summarize those methods grouped by the underlying assumptions.

2.1 Sand arch stability

The role of arching in sand stability was first treated by Terzaghi¹ in his trap door experiment, which demonstrated that arching was a real and stable phenomenon.

Hall and Harrisberger² initiated the study of sand arch stability in the oil industry. Their paper describes that “an arch is a curved structure spanning an opening, serving to support a load by resolving the vertical stress into horizontal stresses”. Sand arch is visualized as in **Fig. 2.1**. Their experiments were designed to determine whether fluid flow or change in load affects the stability of sand arch. Effects of sand roundness, grain crush, fluid flow and wettability on sand arch formation and stability were studied. It was observed that angular sands are more likely to form sand arch than round sands. Inward fluid flow may help to stabilize sand arch formed by round sands. Slow outward

fluid flow does not disrupt sand arch while faster flow does. Water cut tends to destroy the sand arch.

Stein and coworkers³⁻⁴ described an application of sand arch stability theory, which assumes that the maximum sand-free rate an arch can tolerate is proportional to the shear modulus of the sand.

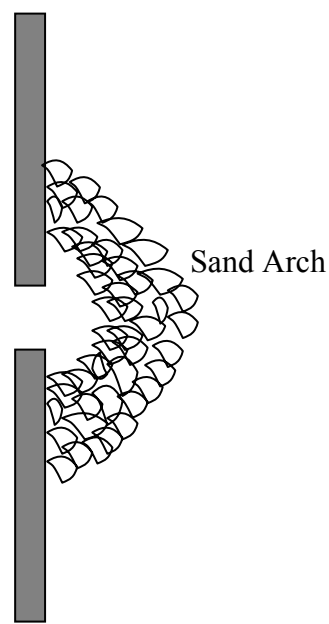


Figure 2.1 Sand arch near perforation

Later Tippie and Kohlhaas⁵ experimentally investigated further the effect of fluid flow rate on sand arch formation and stability. They concluded from their experiments that substantial sand-free producing rates can be maintained through stable sand arches in unconsolidated sands. Arch growth is a function of production rate and initial arch size.

An arch may be destroyed and a new arch be formed through gradual increase of flow rate.

Cleary *et al.*⁶ experimentally studied the effect of stress and fluid properties on sand arch stability in unconsolidated sands. They reported that the arch size decreases with increasing confining stress. They found also that a more stable arch occurs when the horizontal stress is the maximum principal stress and the vertical stress is the minimum principal stress.

Bratli and Risnes⁷ studied in laboratory the sand arch phenomenon due to stresses imposed by flowing fluid. An elastoplastic stress solution was obtained by simplifying the arch geometry as a hemisphere. They presented a stability criterion describing the total failure of sand, as well as the failure of an individual arch. Good agreement between theory and experimental data was shown. Later Polillo *et al.*⁸ studied the same problem with elastoplastic finite element method.

Yim *et al.*⁹'s experimental study showed that the ratio of sand grain size to outlet hole size and grain size distribution are important factors.

More recently, Bianco and Halleck¹⁰ extended Hall and Harrisberger's² work to study the effects of change in wetting phase saturation on arch behavior, morphology and stability. Their main conclusion is that within a defined range, a progressive increase in wetting phase saturation does not impact sand arch stability. As the wetting phase saturation exceeds a critical value, sand arch instability occurs.

In the above papers, it is assumed that sand arch is formed around a perforation and the perforation just penetrates the well casing and cement sheath. This theory may also be used assuming there is a sand arch at the perforation tip if the perforation tunnel is long enough. However, no model considered the interaction of multiple arches when the shot density is high.

2.2 Perforation tunnel stability

Antheunis *et al.*¹¹ simulated the perforation collapse by loading a number of thick-wall hollow cylinders to failure. The thick-walled hollow cylinder experiments were numerically analyzed with the aid of elastoplastic theory. It was found that yielding and ultimate failure is not equivalent. It was concluded from their experiments that the failure criterion could be expressed in terms of a limiting value of the equivalent plastic strain.

Morita *et al.*¹², by separating the effect of well pressure and local pressure gradient around the cavity, proposed an analytical approach to study the effects of many parameters on sand production. It was pointed out that the following parameters may affect sand production: (1) boundary loads such as well pressure and in-situ stresses, (2) fluid flow induced force which is dependent on such factors as flow rate, permeability, viscosities of fluids, relative permeability for multiphase flow and fluid saturation, (3) rock deformation character, (4) rock strength character, (5) perforation cavity geometry and shot density, (6) cyclic loading history. A cavity failure envelope, composed of a tensile failure envelope and shear failure envelope, is generated with their model. If the well pressure is too low, shear failure will occur, if the pressure gradient is too high, tensile failure will occur. They demonstrated that the reservoir pressure depletion increases the effective in-situ stress, especially the effective vertical stress component, which results in the shift of the cavity failure envelope. Therefore, depletion-triggered tensile stress induced sand instability is less likely but shear induced sanding problem may become dominant. The authors note that the results obtained should be used on a qualitative basis because of some degree of simplification.

Morita *et al.*¹³ provided an analysis of perforation tunnel stability using a set of 3D transient fluid flow and geomechanical finite element codes. The results are said to be quantitatively accurate and can be applied to field design. The grid system used in this study is shown in **Fig. 2.2**.

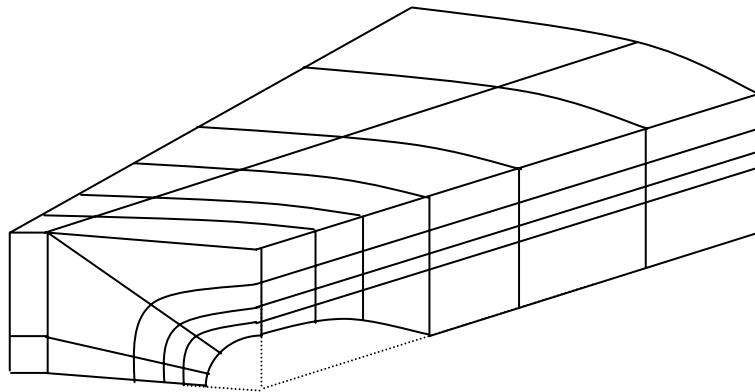


Figure 2.2 Grid system used by Morita *et al.* ¹³

Santarelli *et al.*¹⁴ used a 3D finite element code to study the stress concentration around perforations and to relate it to sand production risk. Influence of perforation geometric features such as perforation length, diameter, shot density, phasing and cementation quality were studied. Results show that: (1) Sand production risk is independent of perforation length; (2) Large shot density will increase the mechanical interaction between adjacent perforations and thus sand production risk; (3) Cavity enlargement will further worsen perforation interaction; (4) In poorly cemented wells, perforations can be oriented to decrease sand production risk and the optimal angle only depends on the in-situ stress state.

Tronvoll *et al.*¹⁵ performed comprehensive laboratory and numerical studies of perforation cavity and sand production from a perforation tunnel. Jacketed cores with a cavity simulating a perforation tunnel are loaded in a high-pressure vessel and fluid flow is applied. Cavity deformation and failure are monitored. A 3D nonlinear finite element model was employed to study cavity stability. It was shown, from both numerical modeling and experiments, that the onset of sand production is mainly controlled by the

formation strength and the in-situ stress state. The results of their study explain quantitatively some field observations. In their study, the failure point is chosen as the point of the cavity displacement curve corresponding to a critical plastic strain of the material in the vicinity of the cavity wall.

We remark that in the above models, only one perforation is considered, i.e, no interactions between multiple tunnels are considered.

2.3 Open hole stability

This type of study focuses on the near borehole, vertical, horizontal or deviated, stress state simulation and its application to sanding prediction. The stress-strain relation of the material, the strength criterion, the post failure behavior, and the effect of fluid flow, are very important for accurate simulation of the behavior of the material. Detailed finite element simulation brings more accurate results but an analytical solution may better emphasize the effect of a single parameter. Laboratory hollow cylinder experiments may be necessary to validate the analytical or numerical solution before it is used in field sanding prediction.

The near borehole stress models published in the literature are categorized as: (1) analytical axisymmetrical plane strain model, this type of model may be used to study sanding phenomenon in vertical and horizontal wells; (2) analytical 2D plane strain model considering the effect of in-situ stress anisotropy, this type of model may be used to consider the effect of anisotropic horizontal stresses on horizontal, vertical and deviated well sand production; (3) numerical model, this type of model may take into account the effect of in-situ stress anisotropy, material nonlinearity and different boundary conditions.

2.3.1 Analytical axisymmetrical plane strain model

Pasley and Cheatham¹⁶ studied the near well stress induced by fluid flow into the borehole using an axisymmetrical plane strain model. The formation material is

considered as linear elastic, fluid is incompressible and flow is in steady state. Permeability variation and its effect on rock failure were studied. Geertsma¹⁷ provided a general poroelastic plane strain solution without assuming a particular fluid flow regime. Risnes and Bratli¹⁸ found a poroelastoplastic solution for incompressible fluid flow under steady state condition. The simplification, which assumes no fluid flow when the maximum principal stress is the vertical stress, may need to be improved for practical usage. It is worth mentioning that an initial vertical strain is considered, which may lead to more accurate description of the in-situ stress condition. Wang *et al.*¹⁹ provided a complete axisymmetrical plane strain poroelastoplastic solution, which was used to study perforation tunnel stability and gas well sand production. Bradford and Cook²⁰ proposed a semi-analytical model to study wellbore stability and sand production. Single fluid flow is assumed transient flow in infinite acting reservoir. More recently, Van den Hoek *et al.*²¹ studied the near well stress state by considering the change of material cohesion in the plastic zone.

2.3.2 Analytical 2D plane strain model

Under anisotropic in-situ stress condition when the maximum and minimum horizontal stresses are different, the Kirsch solution can be used²². However, it is assumed that there is no fluid flow from the wellbore to the formation or from the formation to wellbore, therefore, it may be not appropriate to use this solution to sand production prediction for a flowing well. Despite that, a couple of applications of this model had been reported to predict maximum sand-free production rate for directional well²³ and horizontal well²⁴ by assuming uniform pore pressure in the reservoir and a different pressure in the wellbore. For a specific average reservoir pressure, a critical wellbore pressure is calculated and then it is used to predict the critical sand-free production rate. No analytical model considering near wellbore pressure gradient under anisotropic in-situ stress condition has been found.

2.3.3 Numerical model

Generally, numerical models provide more detailed and accurate description of the stress state. Abousleiman *et al.*²⁵⁻²⁶ provided a poroelastic model to study wellbore stability. Some other effects such as thermal, chemical and physical were also included in their model. Vardoulakis *et al.*²⁷ studied the hydro-mechanical aspects of the sand production problem. A mathematical model is established to describe the transport of sand particles in formation. As a result, the amount of sand produced as a function of time is calculated from their model. Material balance equations are established for the flowing sand particle, the formation matrix and the flowing fluid. The amount of eroded sand and deposited sand is related to flow rate, porosity, sand concentration, and a sand production coefficient, which is determined through experiment and calibrated through field simulation. The effect of porosity increase on permeability is taken into account through the Carman-Kozeny equation. Later, Stavropoulou *et al.*²⁸ coupled the erosion model with near well stress model. The effect of porosity change on elasticity and cohesion is also included in their model. Papamichos *et al.*²⁹⁻³¹ used similar method to study volumetric sand production. Recently, Coomble *et al.*³² coupled the erosion model with more complicated near wellbore stress delineation and fluid flow model to describe the cold production process of heavy oil. Wang *et al.*³³⁻³⁵ used a coupled flow-geomechanical model to simulate the sand production process and wellbore stability. Sand production is assumed to occur if either a critical stress state or a critical strain state is reached. The amount of sand produced is assumed to be proportional to the sanding zone size.

2.4 Sand production criterion

Several mechanisms are recognized as responsible for sand production, such as tensile failure, shear failure and pore collapse.

2.4.1 Tensile failure

Bratli and Risnes⁷ proposed a tensile failure criterion for perforation tunnel inner shell collapse. Risnes and Bratli¹⁸ used the same criterion to hollow cylinder. Tensile failure may occur when the effective radial stress is equal to the tensile strength of the formation rock.

Based on Risnes and Bratli¹⁸'s work, Vaziri³⁶⁻³⁷ employed a fully coupled fluid flow and deformation model to consider the effect of transient fluid flow, nonlinear soil and fluid behavior on sand production. It was found that a cavity, tensile zone, plastic zone and nonlinear elastic zone may form around wellbore.

Perkins and Weingarten³⁸ studied the conditions necessary for stability or failure of a spherical cavity in unconsolidated or weakly consolidated rock. Weigarten and Perkins³⁹ derived an equation describing tensile failure condition in terms of pressure drawdown, wellbore pressure, formation rock cohesion and frictional angle. In their paper, dimensionless curves are provided for determining the pressure drawdown at a specified wellbore pressure.

Ong *et al.*⁴⁰ extended Perkins and Weigarten³⁸ and Weigarten and Perkins's work³⁹ by considering the effect of non-Darcy flow. A foot-by-foot analysis of sand production caused by tensile failure is made possible through their work.

2.4.2 Shear failure and rock strength criterion

If sand production is caused by shear failure, rock strength criterion plays an important role in sand production. Several rock strength criteria have been employed to predict wellbore stability and sand production in the literature. Among which are Von Mises²³⁻²⁴, Drucker-Prager⁴¹, Mohr-Coulomb³⁸⁻³⁹, Hoek-Brown⁴², Modified Lade⁴³⁻⁴⁴ and Modified Weibols & Cook⁴⁵. Laboratory tests may be necessary to know which strength criterion best describes the behavior of the rock studied. Among those strength criteria, the Von Mises criterion is used more in metal than in porous media, the Mohr-

Coulomb and Hoek-Brown criteria consider only the effect of maximum and minimum principal stresses while the Drucker-Prager, Modified Lade and Modified Weibols & Cook criteria involve also intermediate principal stress. The systematic comparison of the use of all those criteria has not been made. For rock behaves in the brittle regime, the sand production criterion may be the same as the rock strength criterion. However, for rock behaves in the ductile regime, it may be necessary to simulate the post yield behavior (hardening or softening) and to propose some other sand production criterion.

2.4.3 Pore collapse

With the depletion of the reservoir pressure, the effective stress acting on the formation rock increases. At a certain stress level, pore collapse may occur and this may lead to sand production. The previous listed criteria are just good to describe failure in the brittle regime and cannot be used to describe failure by pore collapse. As a result, it is necessary to run both triaxial and hydrostatic tests to construct a complete failure envelope.

Some efforts have been made to construct a complete failure envelope and apply it in sand production prediction. Through triaxial and hydrostatic tests of a variety of sandstones, a single normalized failure envelope was established by Zhang *et al.*⁴⁶, see **Fig. 2.3**. The only parameter appears in the normalized envelope is critical pressure, which is correlated to the compression wave velocity. It is not clear if this normalized envelope can be applied universally. Awal *et al.*⁴⁷ demonstrated the application of this normalized curve in sanding onset prediction but the applicability is not verified.

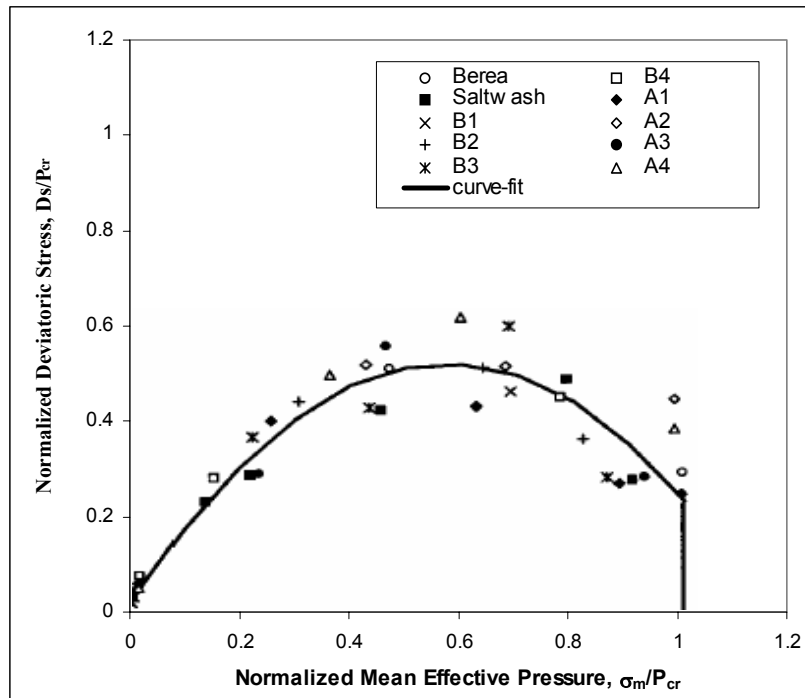


Figure 2.3 Normalized failure envelope for sandstone (after Zhang *et al.*⁴⁶)

The pore collapse portion is shown in the Mohr-Coulomb criterion, see **Fig. 2.4** and in the Drucker-Prager criterion, see **Fig. 2.5**.

In summary, in this chapter, sanding onset prediction methods used in literature are reviewed. The limitations in some of the methods are pointed out. In the following chapters in this work, improved and more general poroelastoplastic stress models for thick-walled hollow cylinder and hollow sphere models are derived. Simple sanding onset prediction models are derived based on those stress models and used in field sanding case studies. The effect of rock strength criterion on sanding onset prediction is studied.

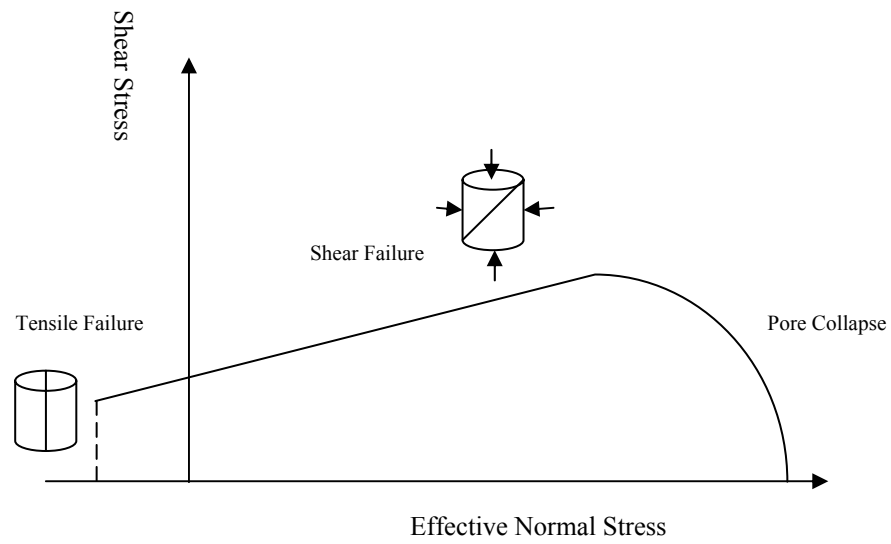


Figure 2.4 Complete Mohr-Coulomb failure envelope including pore collapse (after Abass *et al.*⁴⁸)

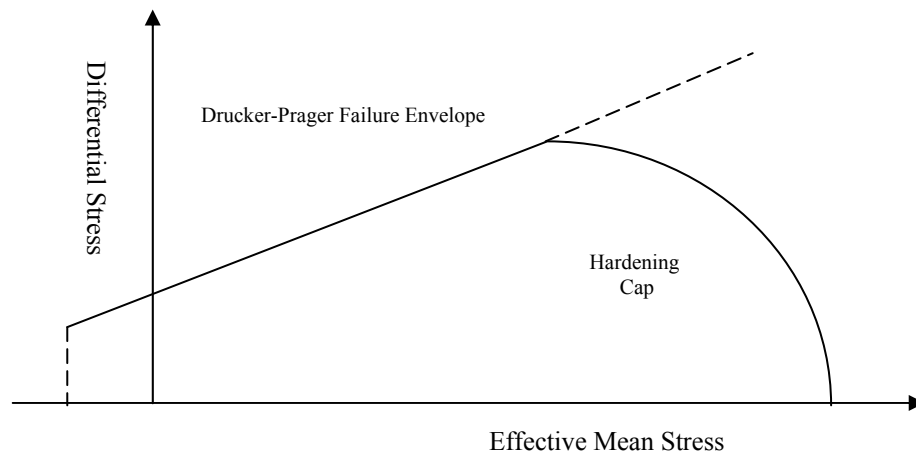


Figure 2.5 Drucker-Prager elliptic cap model (after Chen and Mizuno⁴⁹)

CHAPTER III

ANALYTICAL MODELS FOR SANDING ONSET PREDICTION

Sanding onset prediction involves stress calculation at cavity (including wellbore, perforation tunnel in our cases) surface. Even though a numerical model, such as Finite Element model, is more general, analytical or semi-analytical models may be more convenient and easier to use under special conditions. Besides, an analytical model is always useful to verify numerical models. This chapter provides some improved analytical models for sanding onset prediction.

3.1 Analytical model for wellbore/perforation tunnel failure induced sand production-Isotropic in-situ stress case

In petroleum engineering, the vertical/horizontal wellbore, perforation tunnel and their adjacent formation are often approximated as thick-walled hollow cylinder. Using this approximation, we are able to obtain an analytical or semi-analytical solution for the near wellbore/perforation tunnel stress state and use it in sand production prediction.

As indicated in the previous literature review, Risnes *et al.*¹⁸ studied the near wellbore stress state considering incompressible, steady state fluid flow into wellbore in bounded elastoplastic reservoir. Initial vertical strain is taken into account in their model. Bradford and Cook²⁰ studied the non-steady state oil flow into wellbore in infinite boundary elastoplastic reservoir. Sanfilippo *et al.*⁵⁰ proposed a more general poroelastoplastic model for infinite boundary reservoir by taking into account the initial stresses before a well is drilled and produced. However, for simplicity, the pressure in the well drainage area is assumed to be uniform.

In view of the limitations in the aforementioned models, in this chapter, we propose a more general model suitable for sand production prediction through combining the merits of the previous models. In this model, we assume

- (1) The wellbore/perforation tunnel-formation structure is axisymmetrical.
- (2) The formation rock mechanics properties are homogenous and isotropic. External stresses act axisymmetrically.
- (3) The deformation of formation rock satisfies the plane strain condition.
- (4) The formation rock obeys the Mohr-Coulomb failure criterion and behaves as linear elastic perfect plastic material.

With the above assumptions, we derive a poroelastoplastic solution, see **Appendix A** for detailed derivations.

3.1.1 Poroelasticity solution and shear failure sanding criterion

If the material is in elastic state, the stresses distribution is

$$\sigma'_r = (\lambda + G)A_e - 2G \frac{B_e}{r^2} + \frac{\alpha_b}{r^2} \frac{2G}{\lambda + 2G} \int_{R_w}^r p(r, t) r dr - \alpha_b p(r, t) + \sigma'_h(t_0) \quad (3.1)$$

$$\sigma'_\theta = (\lambda + G)A_e + 2G \frac{B_e}{r^2} - \frac{\alpha_b}{r^2} \frac{2G}{\lambda + 2G} \int_{R_w}^r p(r, t) r dr - \alpha_b \frac{\lambda}{\lambda + 2G} p(r, t) + \sigma'_h(t_0) \quad (3.2)$$

For sanding onset prediction, we are only interested in stresses at wellbore/perforation tunnel surface. The stresses at the surface are

$$\sigma'_r = (1 - \alpha_b) P_{wf}(t) \quad (3.3)$$

$$\sigma'_\theta = \frac{P_{wf}(t) R_w^2 - (2\sigma_h(t) - P_{wf}(t)) R_e^2}{R_w^2 - R_e^2} - \alpha_b \frac{1 - 2\nu}{1 - \nu} \bar{P}(t) - \alpha_b \frac{\nu}{1 - \nu} P_{wf}(t) \quad (3.4)$$

In our case, $R_e \gg R_w$, and the above equation simplifies to

$$\sigma'_\theta = 2\sigma_h(t) - \alpha_b \frac{1-2\nu}{1-\nu} \bar{P}(t) - (1 + \alpha_b \frac{\nu}{1-\nu}) P_{wf}(t) \quad (3.5)$$

If we assume that the effective tangential stress is the maximum principal stress and the effective radial stress is the minimum principal stress, and if we assume sanding occurs at shear failure condition, using Mohr-Coulomb criterion,

$$\frac{\sigma'_\theta - \sigma'_r}{2} = \frac{\sigma'_\theta + \sigma'_r}{2} \sin\phi_f + S_o \cos\phi_f \quad (3.6)$$

Substituting (3.3) and (3.5) into (3.6), we obtain the following sand production criterion

$$\left[(1 - \alpha_b) \frac{1 + \sin\phi_f}{1 - \sin\phi_f} + (1 + \alpha_b \frac{\nu}{1 - \nu}) \right] P_{wf}(t) = 2\sigma_h(t) - \alpha_b \frac{1 - 2\nu}{1 - \nu} \bar{P}(t) - \frac{2S_o \cos\phi_f}{1 - \sin\phi_f} \quad (3.7)$$

Since

$$C_o = \frac{2S_o \cos\phi_f}{1 - \sin\phi_f} \quad (3.8)$$

equation (3.7) can be written in a dimensionless form, which is

$$\left[(1 - \alpha_b) \frac{1 + \sin\phi_f}{1 - \sin\phi_f} + (1 + \alpha_b \frac{\nu}{1 - \nu}) \right] \frac{P_{wf}(t)}{C_o} = 2 \frac{\sigma_h(t)}{C_o} - \alpha_b \frac{1 - 2\nu}{1 - \nu} \frac{\bar{P}(t)}{C_o} - 1 \quad (3.9)$$

If α_b is taken to be one, the above equation simplifies to

$$\frac{P_{wf}(t)}{C_o} = (1 - \nu) \left[2 \frac{\sigma_h(t)}{C_o} - \frac{1 - 2\nu}{1 - \nu} \frac{\bar{P}(t)}{C_o} - 1 \right] \quad (3.10)$$

Sanding occurs when the LHS is less than the RHS.

Fig. 3.1 provides a graphics presentation of dimensionless critical drawdown assuming Poisson's ratio equals to 0.3.

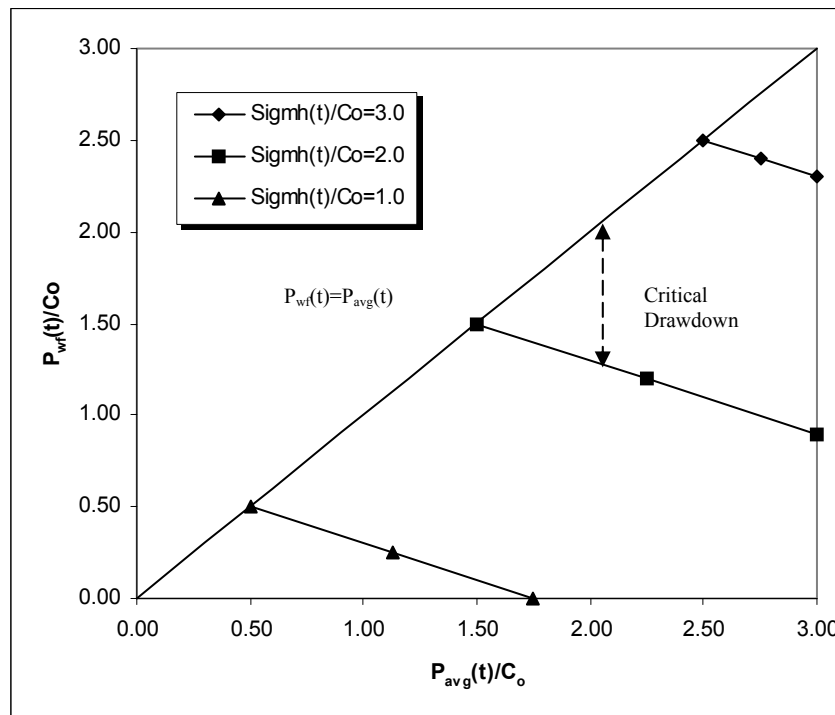


Figure 3.1 Dimensionless critical drawdown plot assuming Poisson's ratio=0.3

3.1.2 Poroelastoplasticity solution and tensile failure sanding criterion

The material becomes plastic if the failure criterion is violated. Using theory of plasticity, we obtained the following solution.

In the plastic zone,

$$\sigma'_r = -\alpha_b r^m \int_{R_w}^r \frac{\partial p(r,t)}{\partial r} r^{-m} dr + C_{hc} r^m - S_o \cot \phi_f \quad (3.11)$$

$$\sigma'_\theta = -\alpha_b q r^m \int_{R_w}^r \frac{\partial p(r,t)}{\partial r} r^{-m} dr + C_{hc} q r^m - S_o \cot \phi_f \quad (3.12)$$

where

$$m = \frac{2 \sin \phi_f}{1 - \sin \phi_f} \quad (3.13)$$

$$q = \frac{1 + \sin \phi_f}{1 - \sin \phi_f} \quad (3.14)$$

$$C_{hc} = \frac{S_o \cot \phi_f + (1 - \alpha_b) P_{wf}(t)}{R_w^m} \quad (3.15)$$

In the elastic zone, the solutions are the same as those in equations (3.1) and (3.2) except that the integration coefficients are different. See **Appendix A** for details.

Even though the material near cavity may fail under shear stresses, it does not necessarily mean sand production occurs. It is possible that sand particles still stay in place and sustain loads until the flow rate is large enough to dislodge the failed sand particles. Weingarten and Perkins³⁹ proposed this sand production criterion. If we assume that the tensile strength of the material is negligible, then the sand production criterion is

$$\left. \frac{d \sigma'_r}{dr} \right|_{r=R_w} = 0 \quad (3.16)$$

Substituting (3.11) into (3.16), yields

$$\alpha_b \left. \frac{\partial p(r,t)}{\partial r} \right|_{r=R_w} = \frac{2 \sin \phi_f}{1 - \sin \phi_f} \frac{S_o \cot \phi_f + (1 - \alpha_b) P_{wf}(t)}{R_w} \quad (3.17)$$

If α_b is taken to be one, the above equation simplifies to the following

$$\left. \frac{\partial p(r, t)}{\partial r} \right|_{r=R_w} = \frac{C_o}{R_w} \quad (3.18)$$

Sand production occurs when the LHS is larger than the RHS.

If we assume fluid flow in reservoir reaches steady state or pseudo-steady state, the LHS is related to average reservoir pressure and bottom hole flowing pressure. A critical drawdown for sanding onset can be derived. Ong *et al.*⁴⁰ derived such solution for steady state fluid flow condition considering non-Darcy flow.

For slightly compressible oil flow in pseudo-steady state, Equation (3.18) becomes

$$\frac{P_{wf}(t)}{C_o} = \frac{\bar{P}(t)}{C_o} - \left[\ln\left(\frac{R_e}{R_w}\right) + \frac{3}{4} \right] \quad (3.19)$$

The comparison between the two criteria is shown in **Fig. 3.2**. We see that the tensile stress induced sanding criterion predicts higher drawdown than the shear failure induced sanding criterion.

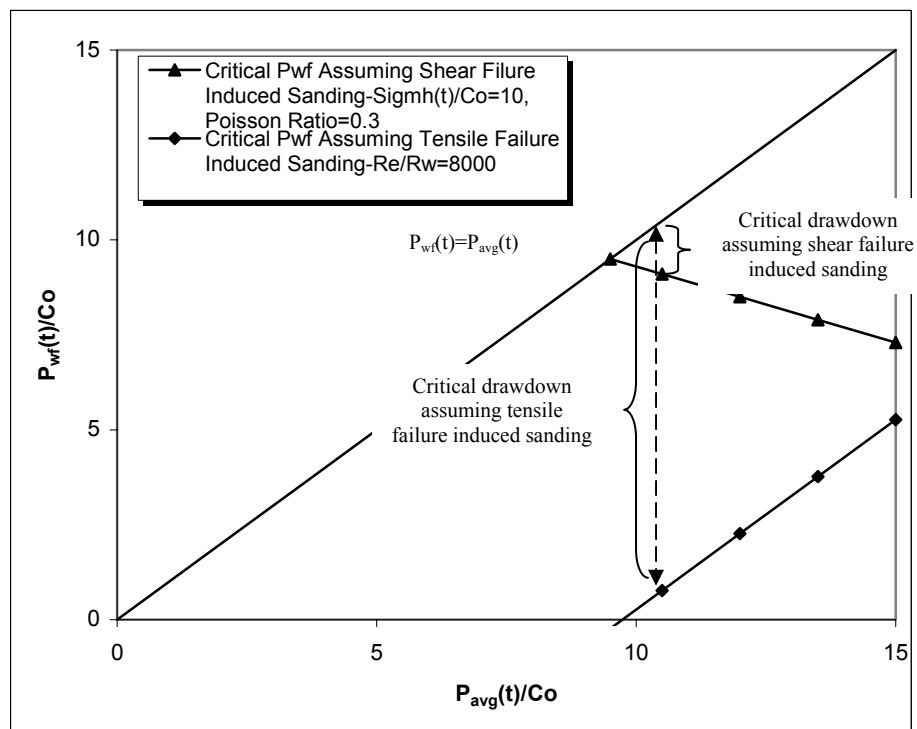


Figure 3.2 Comparison of shear failure induced sanding criterion and tensile failure induced sanding criterion

3.2 Analytical model for wellbore/perforation tunnel failure induced sand production-Anisotropic in-situ stress case

In the above derivations, we assume that the external stresses acting around the wellbore or perforation tunnel are axisymmetrical. In some cases this may not be true. For example, for vertical well, the horizontal in-situ stresses may be different in different direction. For horizontal well, even if the horizontal stress is isotropic, it is often that the vertical stress is not equal to the horizontal stress. So, it is necessarily to develop a solution for this case. In the following derivations, we assume that the in-situ stress in x

direction is the maximum horizontal stress σ_H and in y direction is the minimum horizontal stress σ_h , see **Fig. 3.3**.

The poroelastic solution is obtained through superposition of the stress caused by in-situ stress (Kirsch solution) and the stress induced by fluid flow. The stress solution is

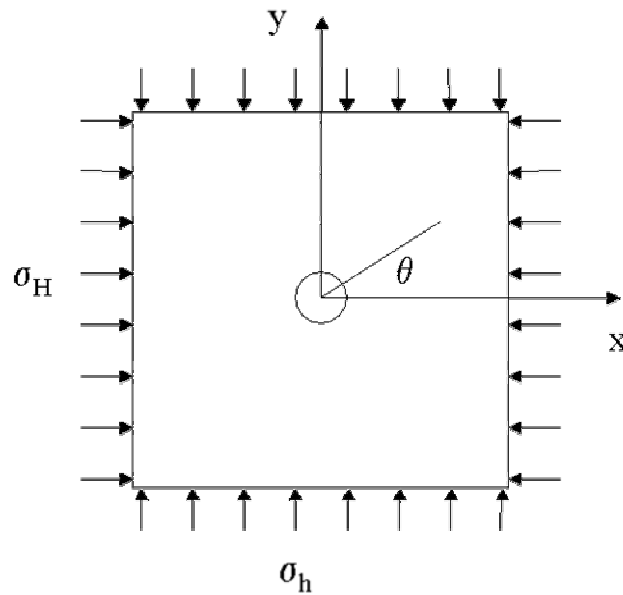


Figure 3.3 Anisotropic in-situ stress around a borehole

$$\begin{aligned} \sigma_r' = & (\lambda + G)A_e - 2G \frac{B_e}{r^2} + \frac{\alpha_b}{r^2} \frac{2G}{\lambda + 2G} \int_{R_w}^r p(r, t) r dr - \alpha_b p(r, t) \\ & + \frac{\sigma_H(t) + \sigma_h(t)}{2} \left(1 - \frac{R_w^2}{r^2}\right) + \frac{\sigma_H(t) - \sigma_h(t)}{2} \left(1 - 4 \frac{R_w^2}{r^2} + 3 \frac{R_w^4}{r^4}\right) \cos(2\theta) \end{aligned} \quad (3.20)$$

$$\begin{aligned} \sigma'_\theta = & (\lambda + G)A_e + 2G \frac{B_e}{r^2} - \frac{\alpha_b}{r^2} \frac{2G}{\lambda + 2G} \int_{R_w}^r p(r, t) r dr - \alpha_b \frac{\lambda}{\lambda + 2G} p(r, t) \\ & + \frac{\sigma_H(t) + \sigma_h(t)}{2} \left(1 + \frac{R_w^2}{r^2}\right) - \frac{\sigma_H(t) - \sigma_h(t)}{2} \left(1 + 3 \frac{R_w^4}{r^4}\right) \cos(2\theta) \end{aligned} \quad (3.21)$$

$$\tau_{r\theta} = -\frac{\sigma_H(t) - \sigma_h(t)}{2} \left(1 + 2 \frac{R_w^2}{r^2} - 3 \frac{R_w^4}{r^4}\right) \sin(2\theta) \quad (3.22)$$

The integration constants A_e and B_e are given in **Appendix B**.

At the wellbore surface, the stresses are

$$\sigma'_r = (1 - \alpha_b) P_{wf}(t) \quad (3.23)$$

$$\begin{aligned} \sigma'_\theta = & \sigma_H(t)(1 - 2\cos(2\theta)) + \sigma_h(t)(1 + 2\cos(2\theta)) - \alpha_b \frac{1 - 2\nu}{1 - \nu} \bar{P}(t) \\ & - \left(\alpha_b \frac{\nu}{1 - \nu} + 1\right) P_{wf}(t) \end{aligned} \quad (3.24)$$

The maximum tangential stress is

$$\sigma'_\theta = 3\sigma_H(t) - \sigma_h(t) - \alpha_b \frac{1 - 2\nu}{1 - \nu} \bar{P}(t) - \left(\alpha_b \frac{\nu}{1 - \nu} + 1\right) P_{wf}(t) \quad (3.25)$$

Using Mohr-Coulomb criterion, the shear failure condition is

$$\begin{aligned} \left[(1 - \alpha_b) \frac{1 + \sin\phi_f}{1 - \sin\phi_f} + \left(\alpha_b \frac{\nu}{1 - \nu} + 1\right) \right] P_{wf}(t) = & 3\sigma_H(t) - \sigma_h(t) \\ - \alpha_b \frac{1 - 2\nu}{1 - \nu} \bar{P}(t) - \frac{2S_o \cos\phi_f}{1 - \sin\phi_f} \end{aligned} \quad (3.26)$$

In dimensionless form, it becomes

$$\left[(1 - \alpha_b) \frac{1 + \sin\phi_f}{1 - \sin\phi_f} + \left(\alpha_b \frac{\nu}{1 - \nu} + 1\right) \right] \frac{P_{wf}(t)}{C_o} = 3 \frac{\sigma_H(t)}{C_o} - \frac{\sigma_h(t)}{C_o} - \alpha_b \frac{1 - 2\nu}{1 - \nu} \frac{\bar{P}(t)}{C_o} - 1 \quad (3.27)$$

If α_b is one, then

$$\frac{P_{wf}(t)}{C_o} = (1-\nu) \left[3 \frac{\sigma_H(t)}{C_o} - \frac{\sigma_h(t)}{C_o} - \frac{1-2\nu}{1-\nu} \frac{\bar{P}(t)}{C_o} - 1 \right] \quad (3.28)$$

Sanding occurs when the RHS is less than the LHS.

Similarly, we obtain the critical drawdown graph for different horizontal stress anisotropy ratios, see **Fig. 3.4**.

To the author's knowledge, the tensile stress induced sand production criterion cannot be derived analytically. Therefore, numerical methods may be needed.

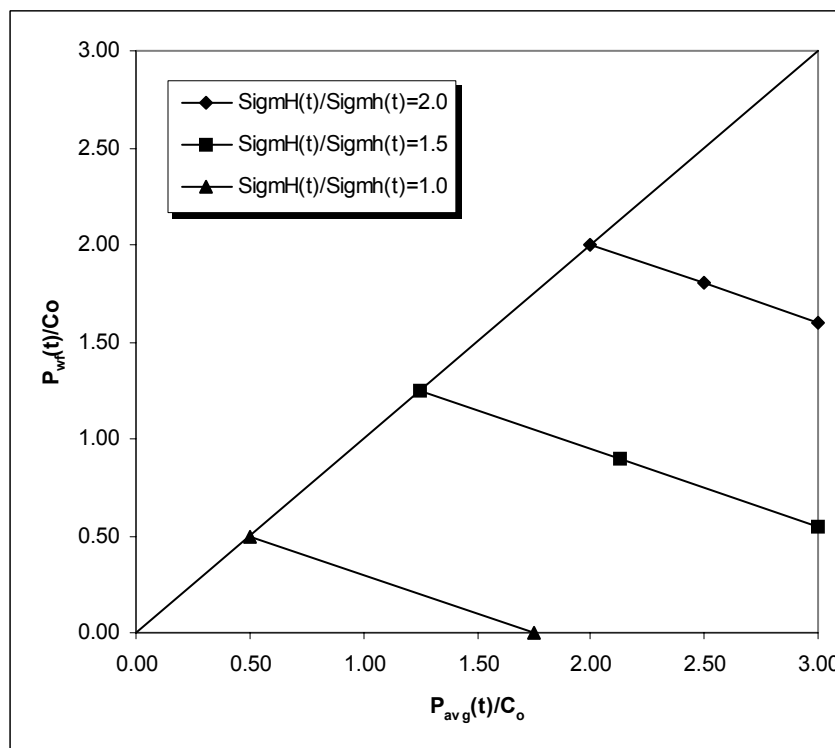


Figure 3.4 Dimensionless critical drawdown plot for different stress anisotropy ratio-
Assuming Poisson's ratio=0.3, $\sigma_h(t) = C_o$

3.3 Analytical model for perforation tip failure induced sand production

Besides perforation tunnel stability, perforation tip stability may also cause sand production. After perforation and a period of oil/gas production, the perforation tip may evolve and become a hemisphere-like structure. It is possible to study the stability of the hemisphere and use it in sand production. In the literature, Bratli and Risnes⁷ studied the stability of sand arch. A poroelastoplasticity model is provided assuming steady state flow condition. Perkins and Weingarten³⁸ derived the shear stability and tensile stability criteria. Weingarten and Perkins³⁹ and Ong *et al.*⁴⁰ used this model in field studies.

Using similar assumptions as those listed in section 3.1, we derive an improved and more general stress solution and sanding onset criterion.

3.3.1 Poroelasticity solution and shear failure sanding criterion

If the material is in elastic state, the stress solution is

$$\sigma'_r = (3\lambda + 2G)\frac{A_e}{3} - 4G\frac{B_e}{r^3} - \alpha_b p(r, t) + \alpha_b \frac{4G}{r^3(\lambda + 2G)} \int_{R_w}^r p(r, t)r^2 dr + \sigma'_h(t_0) \quad (3.29)$$

$$\sigma'_\theta = (3\lambda + 2G)\frac{A_e}{3} + 2G\frac{B_e}{r^3} - \alpha_b \frac{\lambda}{(\lambda + 2G)} p(r, t) - \alpha_b \frac{2G}{r^3(\lambda + 2G)} \int_{R_w}^r p(r, t)r^2 dr + \sigma'_h(t_0) \quad (3.30)$$

The stresses at the inner surface of the sphere are

$$\sigma'_r = (1 - \alpha_b)P_{wf}(t) \quad (3.31)$$

$$\sigma'_\theta = \frac{3\sigma_h(t)}{2} - \alpha_b \frac{1 - 2\nu}{1 - \nu} \bar{P}(t) - \left(\alpha_b \frac{\nu}{1 - \nu} + \frac{1}{2}\right) P_{wf}(t) \quad (3.32)$$

If we assume sand production is caused by shear failure, using Mohr-Coulomb criterion, yields

$$\left[(1 - \alpha_b) \frac{1 + \sin \phi_f}{1 - \sin \phi_f} + \left(\frac{1}{2} + \alpha_b \frac{v}{1 - v} \right) \right] P_{wf}(t) = \frac{3\sigma_h(t)}{2} - \alpha_b \frac{1 - 2v}{1 - v} \bar{P}(t) - \frac{2S_o \cos \phi_f}{1 - \sin \phi_f} \quad (3.33)$$

In dimensionless form, the above equation becomes

$$\left[(1 - \alpha_b) \frac{1 + \sin \phi_f}{1 - \sin \phi_f} + \left(\frac{1}{2} + \alpha_b \frac{v}{1 - v} \right) \right] \frac{P_{wf}(t)}{C_o} = \frac{3}{2} \frac{\sigma_h(t)}{C_o} - \alpha_b \frac{1 - 2v}{1 - v} \frac{\bar{P}(t)}{C_o} - 1 \quad (3.34)$$

If α_b is taken to be one, the above equation simplifies to the following

$$\left(\frac{1}{2} + \frac{v}{1 - v} \right) \frac{P_{wf}(t)}{C_o} = \frac{3}{2} \frac{\sigma_h(t)}{C_o} - \frac{1 - 2v}{1 - v} \frac{\bar{P}(t)}{C_o} - 1 \quad (3.35)$$

Sanding occurs when the LHS is less than the RHS. **Fig. 3.5** provides a comparison of the critical drawdown values for shear failure induced sanding from perforation tunnel and perforation tip.

3.3.2 Poroelastoplasticity solution and tensile failure sanding criterion

The material becomes plastic if the failure criterion is violated. Using theory of plasticity, we obtained the following solution.

$$\sigma'_r = -\alpha_b r^{2m} \int_{R_w}^r \frac{\partial p(r, t)}{\partial r} r^{-2m} dr + C_{hs} r^{2m} - S_o \cot \phi_f \quad (3.36)$$

$$\sigma'_\theta = -\alpha_b q r^{2m} \int_{R_w}^r \frac{\partial p(r, t)}{\partial r} r^{-2m} dr + C_{hs} q r^{2m} - S_o \cot \phi_f \quad (3.37)$$

where the m , q are the same as in (3.13) and (3.14), but the C_{hs} value is given by the following expression.

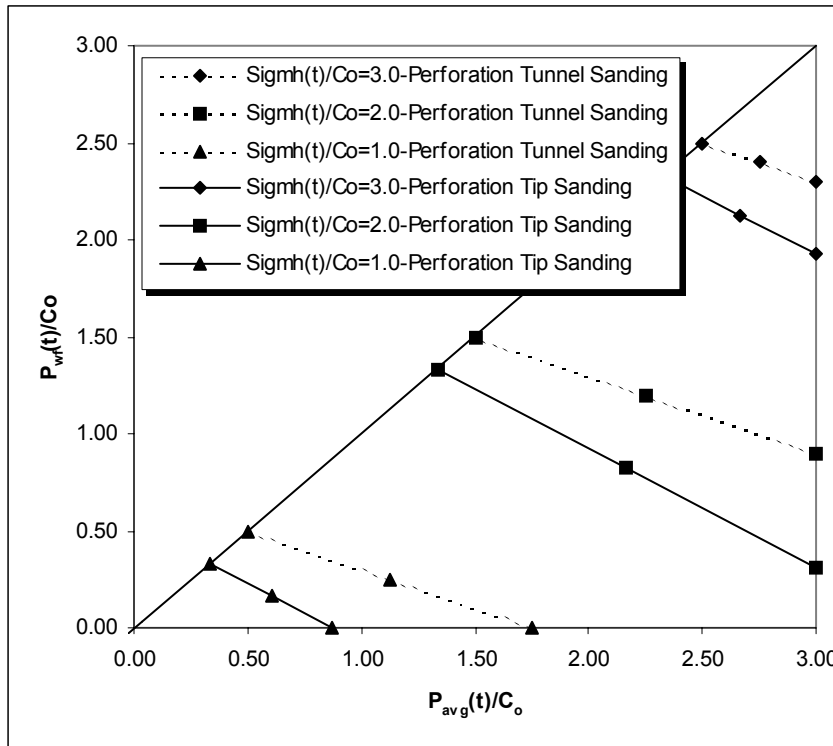


Figure 3.5 Comparison of critical drawdown values for shear failure induced sanding from perforation tunnel and perforation tip

$$C_{hs} = \frac{S_o \cot \phi_f + (1 - \alpha_b) P_{wf}(t)}{R_w^{2m}} \quad (3.38)$$

If sand production does not occur until tensile stress is induced after shear failure, using (3.16), we obtain the following sand production criterion

$$\alpha_b \frac{\partial p(r, t)}{\partial r} \Big|_{r=R_w} = 2 \frac{2 \sin \phi_f}{1 - \sin \phi_f} \frac{S_o \cot \phi_f + (1 - \alpha_b) P_{wf}(t)}{R_w} \quad (3.39)$$

If α_b is one, then

$$\left. \frac{\partial p(r, t)}{\partial r} \right|_{r=R_w} = \frac{2C_o}{R_w} \quad (3.40)$$

Sand production occurs when the LHS is larger than the RHS.

If we assume the fluid flow in reservoir reaches steady state or pseudo-steady state, the LHS is related to average reservoir pressure and bottom hole flowing pressure. A critical drawdown for sanding onset can be derived. Weingarten and Perkins³⁹ derived such solution using steady state flow assumption. Later Ong *et al.*⁴⁰ extended their solution by considering non-Darcy flow.

In summary, in this chapter,

- (1) We derive a poroelastoplastic stress model for thick-walled hollow cylinder model for arbitrary fluid pressure distribution. Based on the thick-walled hollow cylinder model, we derive simple sanding onset prediction models assuming shear failure induced sanding and tensile stress induced sanding after shear failure. These models may be used to study sanding from open hole well or perforation tunnel for cased well.
- (2) We derive a poroelastoplastic stress model for thick-walled hollow sphere model for arbitrary fluid pressure distribution. Based on the thick-walled hollow sphere model, we derive simple sanding onset prediction models assuming shear failure induced sanding and tensile stress induced sanding after shear failure. These models may be used to study sanding from perforation tip for cased well.
- (3) We derive a poroelastic stress model for thick-walled hollow cylinder model under anisotropic in-situ stresses condition. We derive a sanding onset criterion assuming shear failure induced sanding. This model may be used to study sanding from open hole well where the in-situ stresses are different.

CHAPTER IV

NUMERICAL MODEL FOR SANDING ONSET PREDICTION

The use of plane strain models developed in the previous chapter is limited because of the underlying plane strain assumption. To describe the stress state more realistically, a 3D stress model may be required. This chapter describes the 3D poroelastoplastic model for an elastic-perfect plastic material.

4.1 3D stress model

Using the theory of poroelasticity⁵¹, we obtain the momentum equilibrium equation for a porous media with fluid flow as

$$\frac{\partial \sigma'_x}{\partial x} + \frac{\partial \tau_{xy}}{\partial y} + \frac{\partial \tau_{zx}}{\partial z} + f_x + \alpha_b \frac{\partial p}{\partial x} = 0 \quad (4.1)$$

$$\frac{\partial \sigma'_y}{\partial y} + \frac{\partial \tau_{yz}}{\partial z} + \frac{\partial \tau_{xy}}{\partial x} + f_y + \alpha_b \frac{\partial p}{\partial y} = 0 \quad (4.2)$$

$$\frac{\partial \sigma'_z}{\partial z} + \frac{\partial \tau_{zx}}{\partial x} + \frac{\partial \tau_{yz}}{\partial y} + f_z + \alpha_b \frac{\partial p}{\partial z} = 0 \quad (4.3)$$

Assuming the material behaves linear elastically before yield,

$$\begin{Bmatrix} \sigma'_x - \sigma'_H(z, t_0) \\ \sigma'_y - \sigma'_h(z, t_0) \\ \sigma'_z - \sigma'_v(z, t_0) \\ \tau_{xy} \\ \tau_{yz} \\ \tau_{xz} \end{Bmatrix} = \mathbf{D} \begin{Bmatrix} \varepsilon_x \\ \varepsilon_y \\ \varepsilon_z \\ \gamma_{xy} \\ \gamma_{yz} \\ \gamma_{xz} \end{Bmatrix} \quad (4.4)$$

where

$$\mathbf{D} = \frac{E}{(1+\nu)(1-2\nu)} \begin{bmatrix} 1-\nu & \nu & \nu & 0 & 0 & 0 \\ \nu & 1-\nu & \nu & 0 & 0 & 0 \\ \nu & \nu & \nu & 0 & 0 & 0 \\ 0 & 0 & 0 & \frac{1-2\nu}{2} & 0 & 0 \\ 0 & 0 & 0 & 0 & \frac{1-2\nu}{2} & 0 \\ 0 & 0 & 0 & 0 & 0 & \frac{1-2\nu}{2} \end{bmatrix} \quad (4.5)$$

The relation between displacement and strain is defined as

$$\begin{Bmatrix} \varepsilon_x \\ \varepsilon_y \\ \varepsilon_z \\ \gamma_{xy} \\ \gamma_{yz} \\ \gamma_{xz} \end{Bmatrix} = \begin{bmatrix} \frac{\partial}{\partial x} & 0 & 0 \\ 0 & \frac{\partial}{\partial y} & 0 \\ 0 & 0 & \frac{\partial}{\partial z} \\ \frac{\partial}{\partial y} & \frac{\partial}{\partial x} & 0 \\ 0 & \frac{\partial}{\partial z} & \frac{\partial}{\partial y} \\ \frac{\partial}{\partial z} & 0 & \frac{\partial}{\partial x} \end{bmatrix} \begin{Bmatrix} u \\ v \\ w \end{Bmatrix} \quad (4.6)$$

Boundary conditions may vary with the specific problem being solved. Most commonly, the displacement at a specific location may be specified, or the force applied at a specific location be specified.

4.2 3D transient fluid flow model

Assuming single-phase flow according to Darcy's law, we establish a material balance equation⁵².

$$\begin{aligned} & \frac{\partial}{\partial x} \left(\frac{k_x}{\mu_f B_f} \left(\frac{\partial p}{\partial x} + \gamma_f \frac{\partial H}{\partial x} \right) \right) + \frac{\partial}{\partial y} \left(\frac{k_y}{\mu_f B_f} \left(\frac{\partial p}{\partial y} + \gamma_f \frac{\partial H}{\partial y} \right) \right) \\ & + \frac{\partial}{\partial z} \left(\frac{k_z}{\mu_f B_f} \left(\frac{\partial p}{\partial z} + \gamma_f \frac{\partial H}{\partial z} \right) \right) = \frac{\phi (C_r + C_f)}{B_f} \frac{\partial p}{\partial t} \end{aligned} \quad (4.7)$$

The initial condition is

$$p(x, y, z, t)|_{t=0} = p_i(x, y, z) \quad (4.8)$$

where p_i is the initial pressure depending on location.

The boundary conditions may vary with the problem being solved. Generally, a pressure at a specific location may be specified, or the flow rate across a specific surface be specified.

4.3 Mohr-Coulomb plasticity

4.3.1 Mohr-Coulomb criterion in terms of stress invariants

In the previous chapter, it was assumed that the tangential stress around a cavity is the maximum principal stress and the radial stress is the minimum principal stress. In this chapter, we provide a more general form of the Mohr-Coulomb criterion so that it can be used more conveniently in plastic deformation simulation.

If σ_1 is the maximum principal stress and σ_3 is the minimum principal stress, the Mohr-Coulomb failure criterion is written as

$$\frac{\sigma_1 - \sigma_3}{2} = \frac{\sigma_1 + \sigma_3}{2} \sin \phi_f + S_o \cos \phi_f \quad (4.9)$$

We can also express equation (4.9) in terms of stress invariants using the following equations⁵³

$$\sigma_1 = \frac{I_1}{3} + \frac{2}{\sqrt{3}} \sqrt{J_2} \sin\left(\theta_L + \frac{2}{3} \pi\right) \quad (4.10)$$

$$\sigma_2 = \frac{I_1}{3} + \frac{2}{\sqrt{3}} \sqrt{J_2} \sin\theta_L \quad (4.11)$$

$$\sigma_3 = \frac{I_1}{3} + \frac{2}{\sqrt{3}} \sqrt{J_2} \sin\left(\theta_L - \frac{2}{3}\pi\right) \quad (4.12)$$

In equations (4.10)-(4.12), the stress invariants are defined in the following equations⁵³

$$I_1 = \sigma'_x + \sigma'_y + \sigma'_z \quad (4.13)$$

$$J_2 = \frac{1}{6} [(\sigma'_x - \sigma'_y)^2 + (\sigma'_y - \sigma'_z)^2 + (\sigma'_x - \sigma'_z)^2] + \tau_{xy}^2 + \tau_{yz}^2 + \tau_{xz}^2 \quad (4.14)$$

$$\theta_L = \frac{1}{3} \arcsin\left(-\frac{3\sqrt{3}}{2} \frac{J_3}{J_2^{3/2}}\right) \quad \left(-\frac{\pi}{6} \leq \theta_L \leq \frac{\pi}{6}\right) \quad (4.15)$$

$$J_3 = \begin{vmatrix} \sigma'_x - \frac{I_1}{3} & \tau_{xy} & \tau_{xz} \\ \tau_{xy} & \sigma'_y - \frac{I_1}{3} & \tau_{yz} \\ \tau_{xz} & \tau_{yz} & \sigma'_z - \frac{I_1}{3} \end{vmatrix} \quad (4.16)$$

Substitutes (4.10)-(4.12) into (4.9), it becomes

$$\frac{I_1}{3} \sin\phi_f - \sqrt{J_2} \left(\cos\theta_L + \frac{1}{\sqrt{3}} \sin\theta_L \sin\phi_f\right) + S_o \cos\phi_f = 0 \quad (4.17)$$

The failure function F is defined as

$$F = \frac{I_1}{3} \sin\phi_f - \sqrt{J_2} \left(\cos\theta_L + \frac{1}{\sqrt{3}} \sin\theta_L \sin\phi_f\right) + S_o \cos\phi_f \quad (4.18)$$

Failure occurs when $F \leq 0$.

For non-associated plasticity, the plastic potential function Q can be written as

$$Q = \frac{I_1}{3} \sin\psi - \sqrt{J_2} \left(\cos\theta_L + \frac{1}{\sqrt{3}} \sin\theta_L \sin\psi \right) + S_o \cos\psi \quad (4.19)$$

where ψ is called dilation angle.

4.3.2 Flow rule

In order to derive the relationship between plastic strain component and stress increment, a further assumption on material behavior must be made. In particular it is assumed that the plastic strain increment is proportional to the stress gradient of plastic potential function Q , that is

$$d\boldsymbol{\varepsilon}^p = d_\lambda \frac{\partial Q}{\partial \boldsymbol{\sigma}'} \quad (4.20)$$

where the plastic multiplier, d_λ , is to be determined.

4.3.3 Elastoplastic stress-strain matrix

For elastic-perfect plastic material, there is no hardening and the yield function is only a function of the stress. It does not move during loading and unloading, which means

$$F = F(\boldsymbol{\sigma}') \quad (4.21)$$

By differentiating the yield function, yield

$$\frac{dF}{d\boldsymbol{\sigma}'} = 0 \quad (4.22)$$

If it is assumed that the stress is induced only by elastic strain, then

$$d\boldsymbol{\sigma}' = \mathbf{D}(d\boldsymbol{\varepsilon} - d\boldsymbol{\varepsilon}^p) \quad (4.23)$$

Substituting equation (4.20) into the above equation,

$$d\boldsymbol{\sigma}' = \mathbf{D}(d\boldsymbol{\varepsilon} - d\boldsymbol{\varepsilon}^p) = \mathbf{D}(d\boldsymbol{\varepsilon} - d_\lambda \frac{\partial Q}{\partial \boldsymbol{\sigma}'}) \quad (4.24)$$

Substituting equation (4.24) into equation (4.22),

$$\frac{dF^T}{d\boldsymbol{\sigma}'} d\boldsymbol{\sigma}' = \frac{dF^T}{d\boldsymbol{\sigma}'} \mathbf{D}(d\boldsymbol{\varepsilon} - d_\lambda \frac{\partial Q}{\partial \boldsymbol{\sigma}'}) = 0 \quad (4.25)$$

Rearranging the above equation, yields

$$d_\lambda = \frac{\frac{dF^T}{d\boldsymbol{\sigma}'} \mathbf{D} d\boldsymbol{\varepsilon}}{\frac{dF^T}{d\boldsymbol{\sigma}'} \mathbf{D} \frac{\partial Q}{\partial \boldsymbol{\sigma}'}} \quad (4.26)$$

Therefore

$$d\boldsymbol{\sigma}' = \mathbf{D}(d\boldsymbol{\varepsilon} - d_\lambda \frac{\partial Q}{\partial \boldsymbol{\sigma}'}) = \mathbf{D}(d\boldsymbol{\varepsilon} - \frac{\frac{dF^T}{d\boldsymbol{\sigma}'} \mathbf{D} d\boldsymbol{\varepsilon}}{\frac{dF^T}{d\boldsymbol{\sigma}'} \mathbf{D} \frac{\partial Q}{\partial \boldsymbol{\sigma}'}} \frac{\partial Q}{\partial \boldsymbol{\sigma}'}) = (\mathbf{D} - \frac{\mathbf{D} \frac{\partial Q}{\partial \boldsymbol{\sigma}'} \frac{dF^T}{d\boldsymbol{\sigma}'} \mathbf{D}}{\frac{dF^T}{d\boldsymbol{\sigma}'} \mathbf{D} \frac{\partial Q}{\partial \boldsymbol{\sigma}'}}) d\boldsymbol{\varepsilon} \quad (4.27)$$

The above equation is simplified as

$$d\boldsymbol{\sigma}' = \mathbf{D}_{ep} d\boldsymbol{\varepsilon} \quad (4.28)$$

where

$$\mathbf{D}_{ep} = \mathbf{D} - \frac{\mathbf{D} \frac{\partial Q}{\partial \boldsymbol{\sigma}'} \frac{dF^T}{d\boldsymbol{\sigma}'} \mathbf{D}}{\frac{dF^T}{d\boldsymbol{\sigma}'} \mathbf{D} \frac{\partial Q}{\partial \boldsymbol{\sigma}'}} = \mathbf{D} - \mathbf{D}_p \quad (4.29)$$

\mathbf{D}_{ep} is the elastoplastic stress-strain matrix. Expression for \mathbf{D}_p can be found Appendix 2 in reference⁵³. We note that it is a function of the stress state. Therefore it is necessary to solve the elastoplastic problem iteratively.

4.4 Finite element solution to the 3D stress model

According to the principle of virtual work, the Finite Element formulation of the problem is

$$\iiint_{\Omega_e} \mathbf{B}^T \mathbf{D}_{ep} \mathbf{B} dV \mathbf{u}^e = \mathbf{F}_f^e \quad (4.30)$$

Detailed formulae of the above matrices are provided in **Appendix C**.

Using (4.29), Equation (4.30) becomes

$$\iiint_{\Omega_e} \mathbf{B}^T (\mathbf{D} - \mathbf{D}_p) \mathbf{B} dV \mathbf{u}^e = \mathbf{F}_f^e \quad (4.31)$$

Since $[\mathbf{D}_p]$ is a function of stress state, solving the above equation involves iteration techniques. However, because recalculating and inverting the stiffness matrix in Finite Element Method is time-consuming, the nonlinear part can be moved to the right side during iteration, which results in

$$\iiint_{\Omega_e} \mathbf{B}^T \mathbf{D} \mathbf{B} dV \mathbf{u}^e = \mathbf{F}_f^e + \iiint_{\Omega_e} \mathbf{B}^T \mathbf{D}_p \boldsymbol{\varepsilon} dV \quad (4.32)$$

The second term on the right hand side of (4.32) acts like a body force, it is updated during each iteration while the left side remains unchanged. This algorithm is called “initial stress” algorithm⁵⁴.

Another way of generating the body loads was proposed by Zienkiewicz and Corneau⁵⁵. This algorithm is called “visco-plasticity” algorithm, where the body load is generated through iteration in the following way, at the i^{th} iteration, the body load \mathbf{p}_b is

$$\mathbf{p}_b^i = \mathbf{p}_b^{i-1} + \iiint_{\Omega_e} \mathbf{B}^T (\mathbf{D} \boldsymbol{\varepsilon}^{vp})^i dV \quad (4.33)$$

where

$$\boldsymbol{\varepsilon}^{vp} = \Delta t F \frac{\partial Q}{\partial \boldsymbol{\sigma}'} \quad (4.34)$$

$$\Delta t = \frac{4(1 + \nu)(1 - 2\nu)}{E(1 - 2\nu + \sin^2 \phi_f)} \quad (4.35)$$

4.5 Finite element solution to the 3D fluid flow model

The fluid flow model can be solved with both finite difference method and Finite Element Method. For complicated geometries, the finite difference method may be difficult to apply and the finite element method is preferred. In this work, the 3D fluid flow model is solved by the finite element method.

The finite element formulation for 3D Fluid Flow Model is⁵³

$$\mathbf{K}_p^e \mathbf{p}^e + \mathbf{P}_M^e \frac{\partial \mathbf{p}^e}{\partial t} = \mathbf{q}^e \quad (4.36)$$

Detailed formulae for the above matrices are described in **Appendix D**.

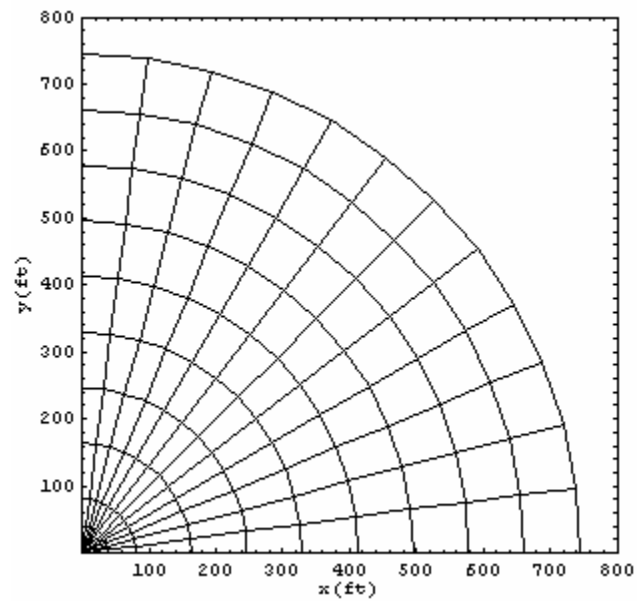
4.6 Verification of the numerical models

4.6.1 Verification of the 3D fluid flow model

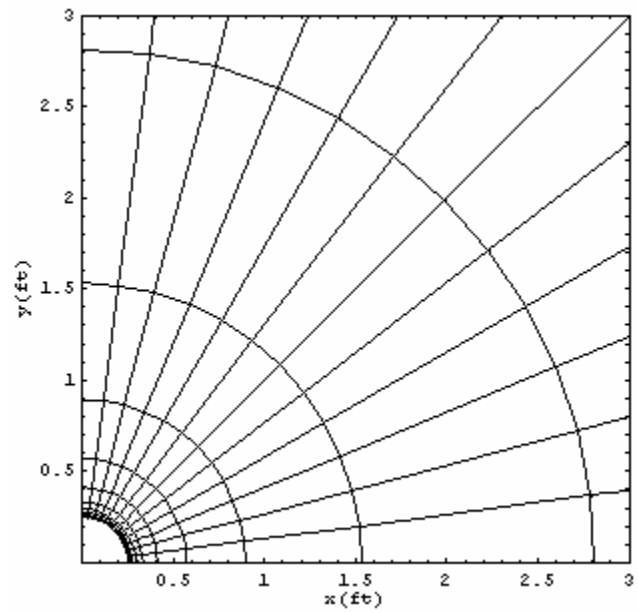
We run several cases in this section to verify the 3D fluid flow model, we show the results of two cases. The first case is single well production at constant rate from a closed axisymmetrical reservoir, with well and reservoir data presented in **Table 4.1**. In the finite element model, the grid used is shown in **Fig. 4.1**. We consider only $\frac{1}{4}$ of the reservoir. Comparison of the bottom hole flowing pressure with the one obtained from commercial reservoir flow simulator is shown in **Fig. 4.2**. We see good agreement between finite element model simulation and finite difference simulation.

Table 4.1 Well, reservoir and production parameters-Case 1

Wellbore Radius (ft)	0.25
Drainage Area (acre)	40
Reservoir Thickness (ft)	20
Gas Specific Gravity (fraction)	0.7
Reservoir Temperature (°F)	108
Initial Reservoir Pressure (psi)	2,800
Permeability (mD)	10
Porosity (fraction)	0.12
Formation Compressibility (1/psi)	1e-6
Initial Production Rate (Mscf/Day)	1,000



(a) Grid for $\frac{1}{4}$ of a reservoir



(b) Grid in near wellbore region

Figure 4.1 Finite element grid used in simulation of single well production from a closed axisymmetrical reservoir

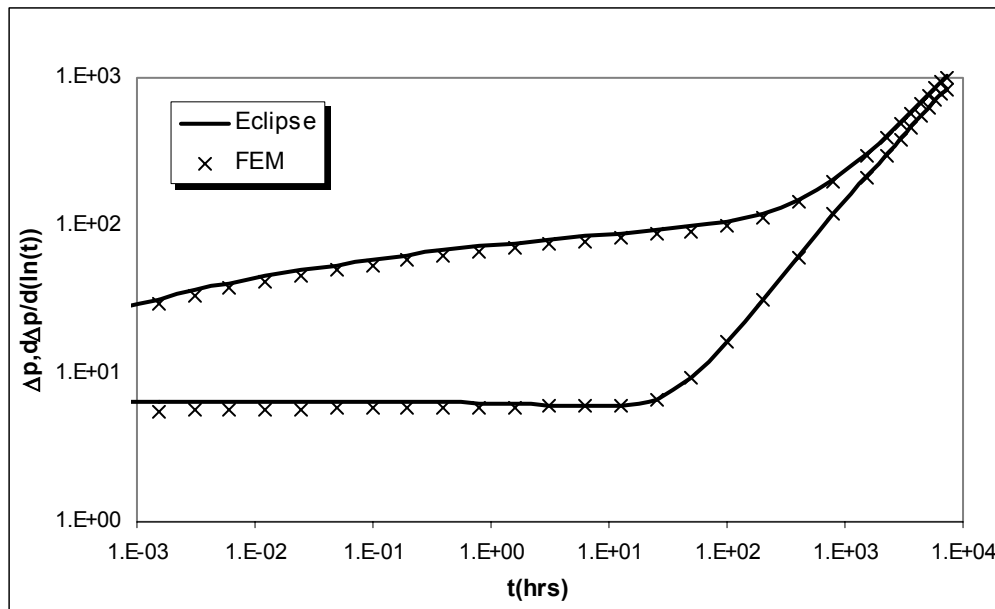
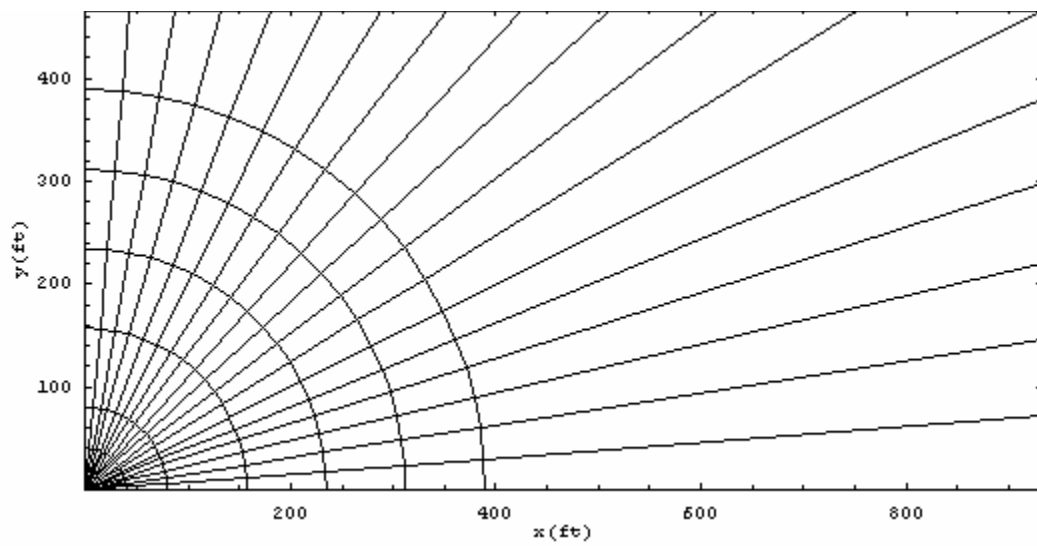


Figure 4.2 Comparison of pressure and pressure derivative curves for single well production from a closed axisymmetrical reservoir

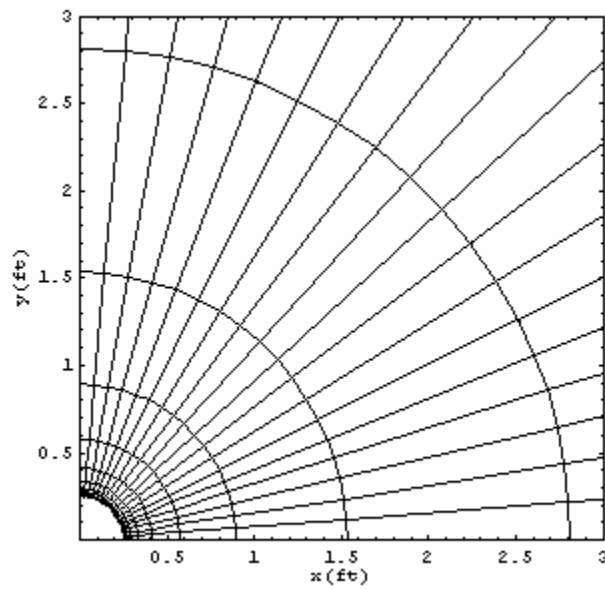
The second case is single well production at const rate from a closed rectangular reservoir, with the well and reservoir data presented in **Table 4.2**. Grid used in finite element simulation is shown in **Fig. 4.3**. Comparison of the bottom hole flowing pressure with the one obtained from commercial reservoir flow simulator is shown in **Fig. 4.4**. As seen from this figure, good agreement is reached between the finite element model simulation and the finite difference simulation. This again verifies the fluid flow simulator developed in this work. Other cases like flowing at constant bottom hole flowing pressure are run and excellent agreement is reached between results from commercial simulator and the model implemented in this work.

Table 4.2 Well, reservoir and production parameters-Case 2

Wellbore Radius (ft)	0.25
Drainage Area (acre)	40
Aspection Ratio	½
Reservoir Thickness (ft)	20
Gas Specific Gravity (fraction)	0.7
Reservoir Temperature (°F)	108
Initial Reservoir Pressure (psi)	2,800
X Direction Permeability (mD)	5
Y Direction Permeability (mD)	10
Z Direction Permeability (mD)	0.1
Porosity (fraction)	0.12
Formation Compressibility (1/psi)	1e-6
Initial Production Rate (Mscf/Day)	1,000



(a) Grid for $\frac{1}{4}$ of a reservoir



(b) Grid in near wellbore region

Figure 4.3 Finite element grid used in simulation of single well production from a closed rectangular reservoir

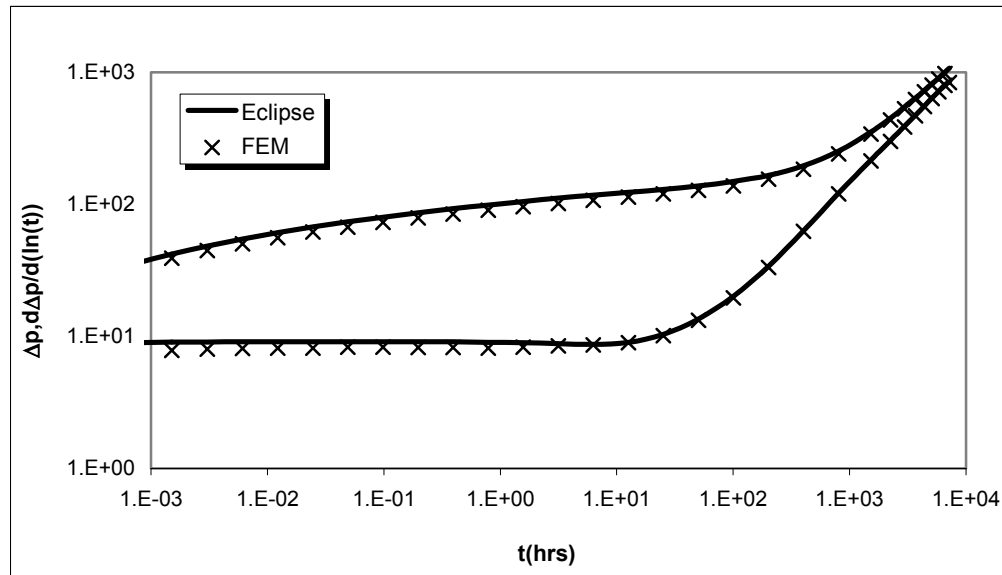


Figure 4.4 Comparison of pressure and pressure derivative curves for single well production from a closed rectangular reservoir

4.6.2 Verification of the 3D stress model

The technical performance of this 3D finite element program is checked against the analytical solutions obtained in the previous chapter. We run several cases in this comparison study. Two cases are presented in this work. The first case is to compare the results with the ones obtained using the poroelastoplastic solution for the thick-walled hollow cylinder model and this finite element code. In this comparison, the following rock mechanics data are used in addition to the well and reservoir parameters listed in the **Table 4.1**, see **Table 4.3**. **Fig. 4.5** presents the comparison of numerical and analytical solutions. From **Fig. 4.5**, we see excellent agreement between numerical and analytical solutions.

Table 4.3 Rock mechanics parameters used in comparison study

Young Modulus (psi)	1.4E+6
Poisson Ratio (fraction)	0.3
Cohesive Strength (psi)	500
Friction Angle (Degree)	30
Overburden Stress (psi)	3400
Horizontal Stress (psi)	3060

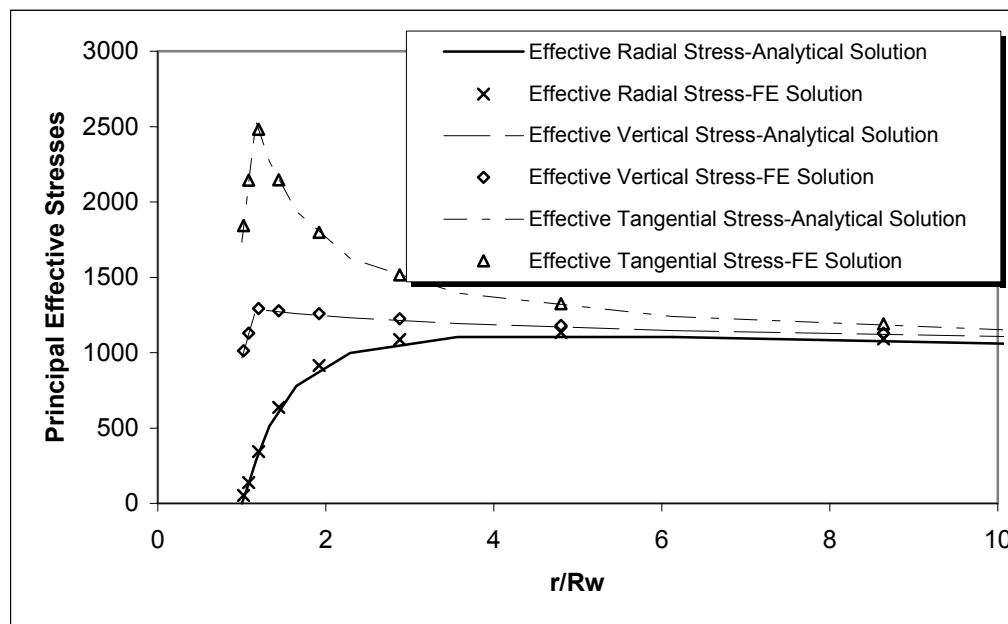


Figure 4.5 Comparison of 3D finite element solution with analytical solution for stress state near wellbore during production

We run the second case to compare the finite element solution with the extended Kirsch solution for anisotropic in-situ stress case. The data used is the same as the isotropic in-situ stress case except that the horizontal stress in x direction is increased to 4590 psi (which means $\sigma_H/\sigma_h = 1.5$). With these data, we compare the principal effective stresses along a specific radial direction, see Fig. 4.6. The agreement between the finite element model and the analytical model is satisfactory. We also get the principal effective stress distribution density plot around the wellbore, see Fig. 4.7.

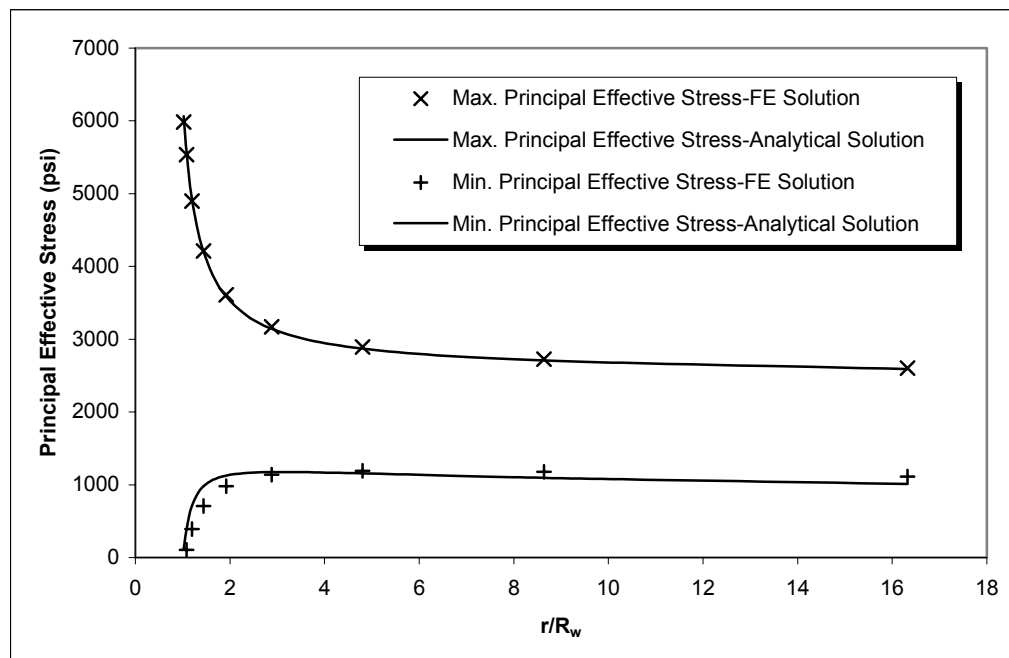
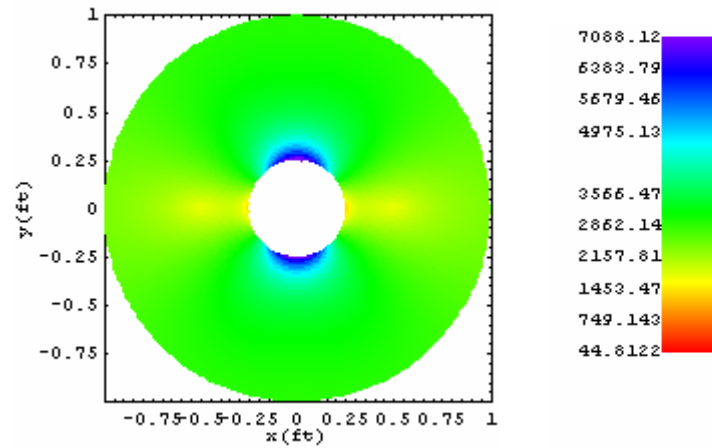
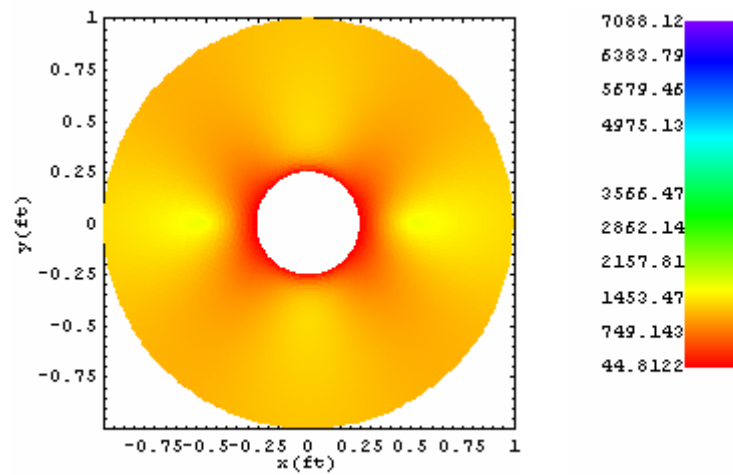


Figure 4.6 Principal effective stresses along radial direction 63.75° to x coordinate



(a) Maximum principal effective stress around wellbore with fluid flow



(b) Minimum principal effective stress around wellbore with fluid flow

Figure 4.7 Principal effective stresses around wellbore for anisotropic in-situ stress case with fluid flow.

4.7 Comparison of numerical model and analytical model

It is worth mentioning that in section 4.6, the comparison between numerical and analytical models is performed to verify the numerical model. In the comparison, same boundary condition and physical geometry are used in the two models. The boundary condition used in the comparison is representative to a real case if the cap rock and underling formation have high Young modulus. In this situation, both models give accurate stress description. Using both models will yield identical stress simulation results and sanding prediction results. However, the flexibility of the Finite Element model lies in that it can deal with different boundary conditions and geometries other than those used in the analytical model. For example, if the cap rock has similar rock mechanics properties as the productive zone but the underling formation has significantly higher Young modulus than the productive zone, the numerical model can describe the stress state more realistically than the analytical model. In this section, using the numerical and analytical stress models, we compare the differences of stress simulation results and sanding onset prediction results.

Using data presented in **Table 4.1** and **Table 4.3**, we performed near wellbore stress simulation with the analytical model and Finite Element model. **Fig. 4.8** presents the boundary conditions and grid used in Finite Element simulation. **Fig. 4.9** presents a comparison of the stress state at the center of the formation after 150 days of production using the analytical and numerical models. We see that the main difference between numerical and analytical simulation results is the vertical stress. This is due to the plane strain assumption used in the analytical model, which assumes that there is no deformation in vertical direction during production and leads to a less vertical stress than the real one. **Fig. 4.10** presents the relative error of the stresses obtained from the analytical model. We see that using the analytical model for this case causes some error on stress state simulation. However, it is noticed that, at the wellbore, radial stress error is only 3%, tangential stress error is only 0.4% and vertical stress error is 20%.

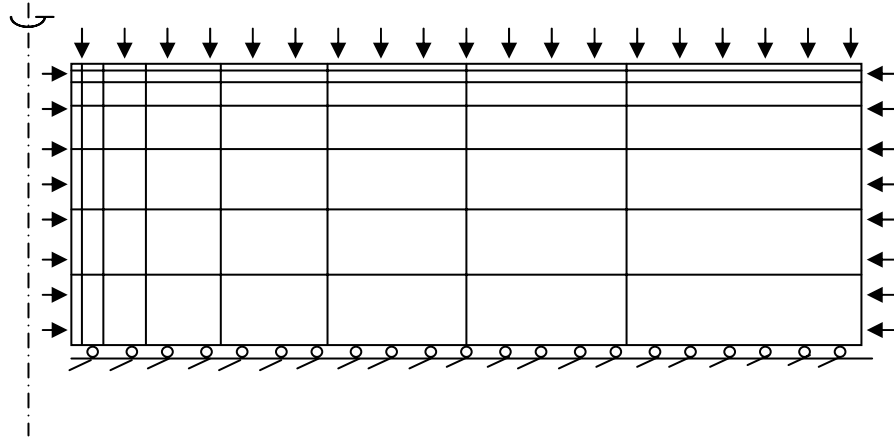


Figure 4.8 Boundary condition and grid used in finite element simulation of near wellbore stress

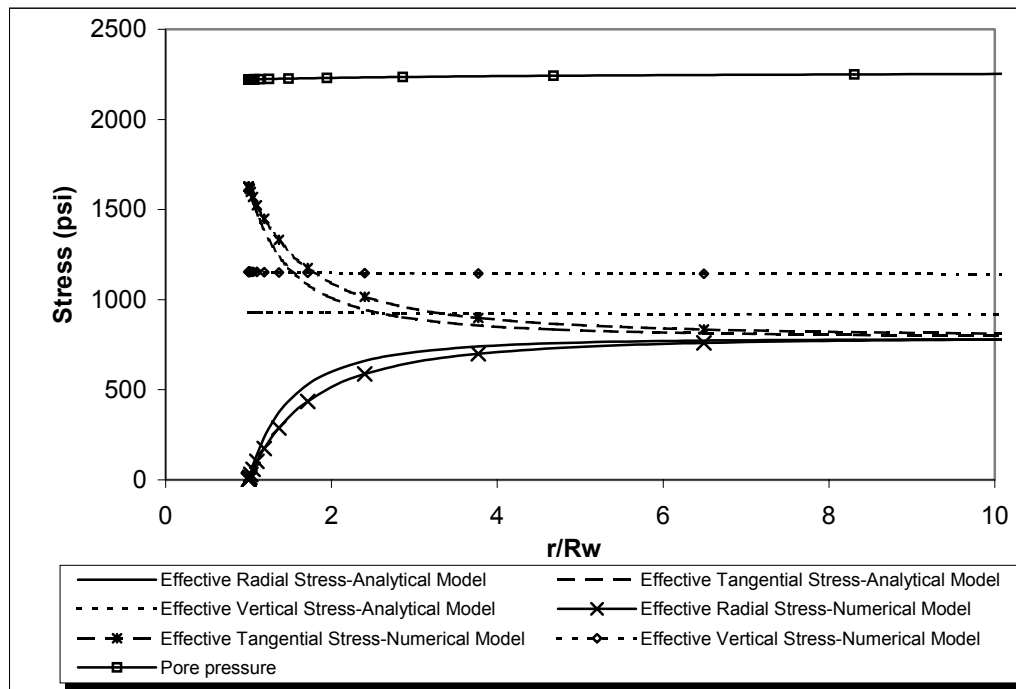


Figure 4.9 Comparison of stress state simulation results after 150 days of production using analytical and numerical models

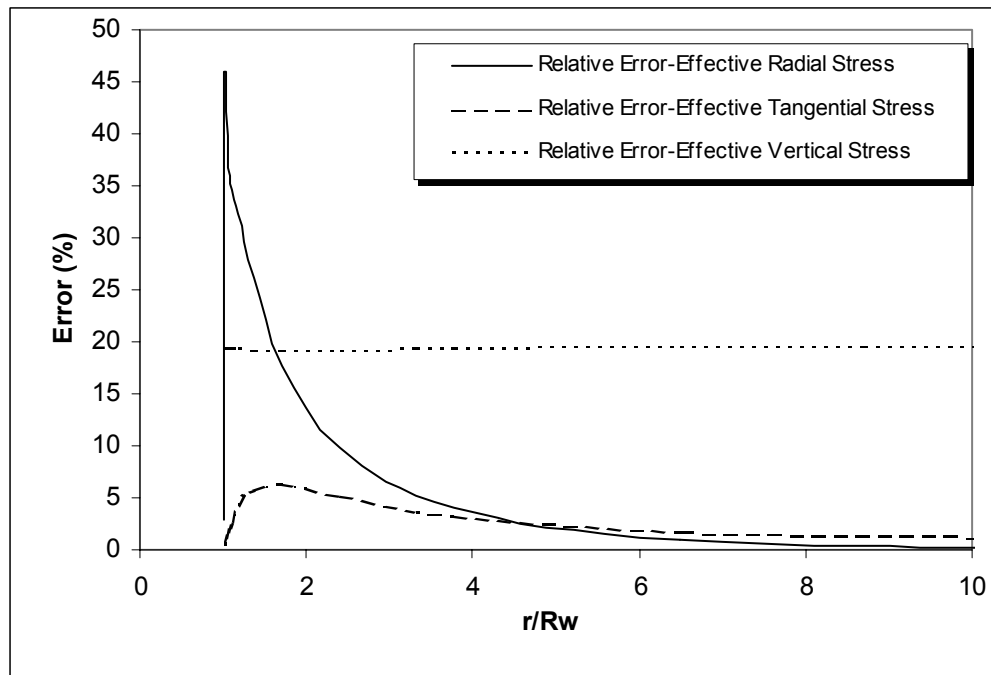


Figure 4.10 Relative error of stresses using analytical model

If we assume sanding is caused by wellbore shear failure, using the sanding model derived from the analytical stress model, equation (3.10), we find that sanding occurs after 171 days of production at $P_{wf} = 2157.86$ psi and $P_{avg} = 2254.70$ psi. Using the numerical model, we find that sanding occurs after 165 days of production at $P_{wf} = 2175.95$ psi and $P_{avg} = 2272.50$ psi. We see that, for the case studied, sanding onset prediction results are not very different by using numerical and analytical stress models. Even though we see large vertical stress difference in the comparison, since the vertical stress is the intermediate principal stress which is not taken into account in Mohr-Coulomb failure criterion, only the tangential stress and radial stress will affect the sanding onset prediction results. Due to the fact that the differences of the tangential stress and radial stress at wellbore from the numerical model and analytical model are minimum, the sanding onset prediction results differ minimally.

4.8 Uncertainty assessment of sanding onset prediction model

Mechanistic modeling of physical systems is often complicated by the presence of uncertainties. This also applies to sanding onset prediction modeling. Even though significant effort may be needed to incorporate uncertainties into the modeling process, this could potentially result in providing useful information that can help sand control decision-making. A systematic uncertainty analysis provides insight into the level of confidence in model estimates, and can help assessing how various possible model estimates should be weighed. Further, it can lead to the identification of the key sources of uncertainty, as well as the sources of uncertainty that are not important with respect to a given response.

The following stages are involved in the uncertainty analysis of a model: (a) estimation of uncertainties in model inputs and parameter (i.e. characterization of input uncertainties), (b) estimation of the uncertainty in model outputs resulting from the uncertainty in model inputs and model parameters (i.e. uncertainty propagation), (c) characterization of uncertainties associated with different model structures and model formulations (i.e. characterization of model uncertainty), and (d) characterization of the uncertainties in model predictions resulting from uncertainties in the evaluation data.

Various methods are available for uncertainties analysis. Among which, Monte Carlo methods are the most widely used ones. These methods involve random sampling from the distribution of inputs and successive model runs until a statistically significant distribution of outputs is obtained. They can be used to solve problems with physical probabilistic structures, such as uncertainty propagation in models or solution of stochastic equations, or can be used to solve non-probabilistic problems. Commercial software @RISK developed by Palisade Corporation (www.palisade.com) is one of the available tools to perform uncertainties analysis.

In this section, we study how input data uncertainties propagate in the sanding onset prediction model and affect model prediction uncertainty. We ignore model uncertainties

and use the analytical sanding onset prediction model, equation (3.10). In the analytical sanding onset prediction model, to predict a critical bottom hole flowing pressure for a specific average reservoir pressure, we need information on Poisson's ratio, UCS, and in-situ horizontal stress. In field practice, these data are rarely available from laboratory test. Sometimes well logging data are available to evaluate Poisson's ratio and UCS, and hydraulic fracturing data are available to evaluate the in-situ stress. It is also quite common that simply no any data available and neighbor well data or engineering estimated data from experience are used. In both cases, data uncertainties exist.

To perform uncertainty analysis, the first step is to estimate the distribution of the model input parameters. As stated earlier in this section, under most conditions, we just have an estimated value for a given parameter through field measurement or experience. It is very hard to know what probability distribution function a parameter satisfies. However it is possible to know the upper and lower bounds of a specific parameter. For illustration purpose, we assume that triangle distribution is satisfied for all three parameters with the minimum, mean and maximum values specified in **Table 4.4**.

Table 4.4 Minimum, mean and maximum values for Poisson's ratio, UCS and in-situ horizontal stress

Parameter	Min. Value	Mean Value	Max. Value
Poisson Ratio (fraction)	0.25	0.3	0.40
Co (psi)	1500	1732	2500
Horizontal Stress (psi)	2800	3060	3400

Using the Monte Carlo simulation model provided in @RISK, we yield the following histogram for the critical bottom hole flowing pressure for an average reservoir pressure of 2500 psi, see **Fig. 4.11**. **Fig. 4.12** presents the cumulative frequency for the predicted bottom hole flowing pressure. From both **Fig. 4.11** and **Fig. 4.12**, we see that the predicted bottom hole flowing pressure is very scattered due to the uncertainties of the input data.

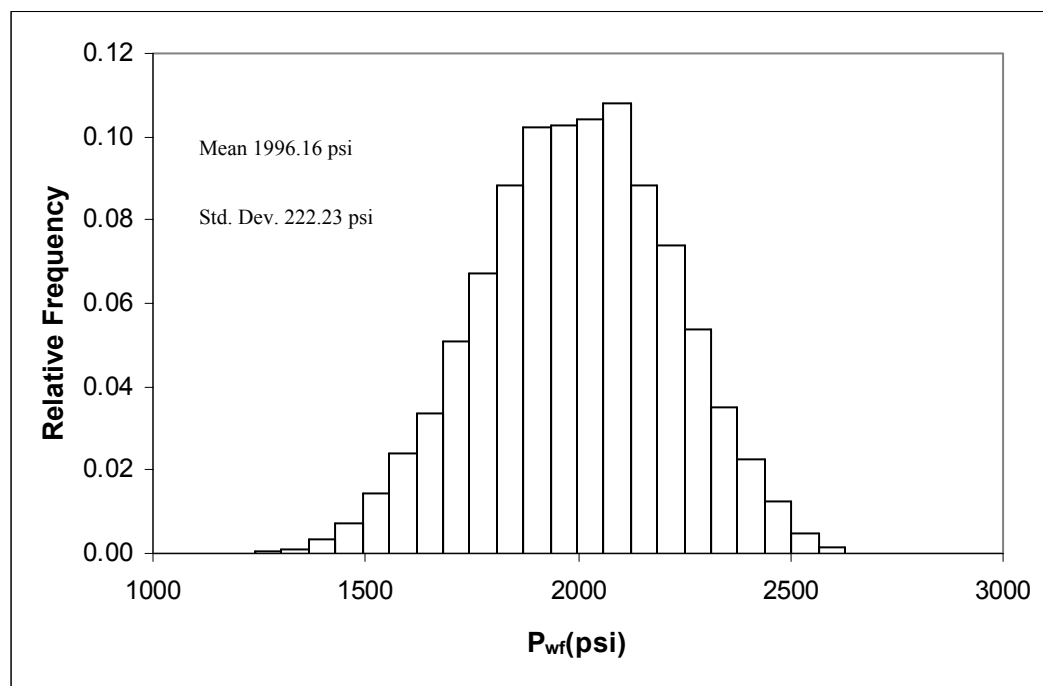


Figure 4.11 Histogram for the predicted critical bottom hole flowing pressure @
 $P_{avg}=2500$ psi

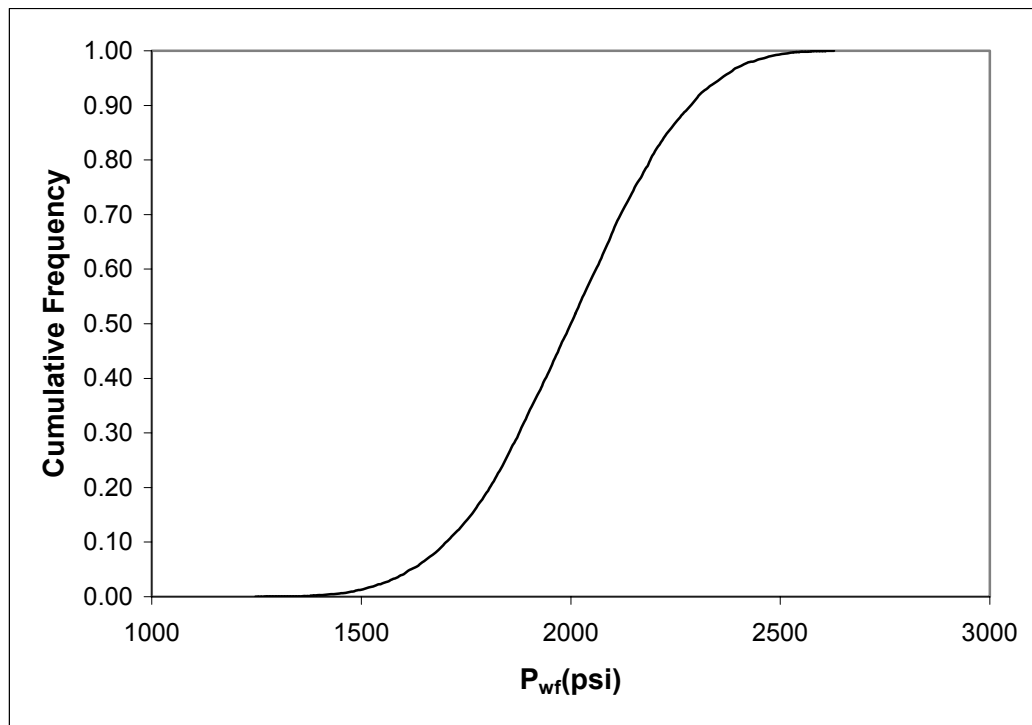


Figure 4.12 Cumulative frequency distribution for the predicted critical bottom hole flowing pressure @ $P_{avg}=2500$ psi

In summary, in this chapter,

- (1) We implemented a 3D general finite element code for stress state simulation and single-phase fluid flow simulation.
- (2) We verified its technical performance against available analytical and numerical solutions.

CHAPTER V

EFFECT OF ROCK STRENGTH CRITERION ON SANDING ONSET PREDICTION

Sanding onset prediction involves near cavity stress calculation and use of rock strength criterion to determine sanding onset conditions. Therefore, rock strength criterion plays a key role in sanding prediction. In each rock strength criterion, there are some rock material parameters involved. In order to predict more accurately the sanding onset conditions, one needs to determine those material parameters based on laboratory test data of the rock.

Ewy⁴³ and McLean & Addis⁵⁶ studied the effect of rock strength criterion on wellbore stability. In their work, a two-step procedure is applied to obtain the rock material parameters in the rock strength criterion. First, the Mohr-Coulomb parameters like cohesion S_o and internal friction angle ϕ_f are regressed from the conventional triaxial test data. Then, the rock material parameters in other criteria are calculated using the regressed Mohr-Coulomb parameters S_o and ϕ_f . Using this procedure, the authors conclude that one rock strength criterion predicts a less conservative critical mud weight than the others and the difference is substantial. In this chapter, we propose a different methodology to evaluate the rock material parameters appearing in each rock strength criterion and investigate their effect on sanding onset prediction.

Four different rock strength criteria, Mohr-Coulomb⁴⁹, Hoek-Brown⁵⁷, Drucker-Prager⁵⁸, and Modified Lade⁴³ are used in conjunction with an axisymmetrical poroelastic stress model to predict the onset of sand production. Using conventional triaxial test data, we propose to regress for the rock material parameters appearing in the rock strength criterion directly from the test data instead of using the regressed Mohr-Coulomb parameters S_o and ϕ_f to calculate the rock material parameters indirectly. Then we demonstrate how the sanding onset prediction results differ from each other. In addition, because two of the aforementioned rock strength criteria are intermediate principal stress

dependent criteria, using conventional triaxial test data only may not be adequate. If we use a set of true triaxial (polyaxial) test data which give the same Mohr-Coulomb parameters S_o and ϕ_f as those given by the previous conventional triaxial test data and perform direct regression, we get quite different sanding onset prediction results. **Fig. 5.1** illustrates the comparison scheme in this chapter.

In this chapter, as a rule, all the stresses are indicated as effective stresses and compressive stress is assumed positive. Pore fluid pressure is always positive. First four rock strength criteria and a near wellbore poroelastic stress model are introduced. Then we demonstrate how different ways of processing the same set of data yield different sanding onset prediction results according to the scheme illustrated in **Fig. 5.1**. Finally conclusions are drawn and recommendations are made.

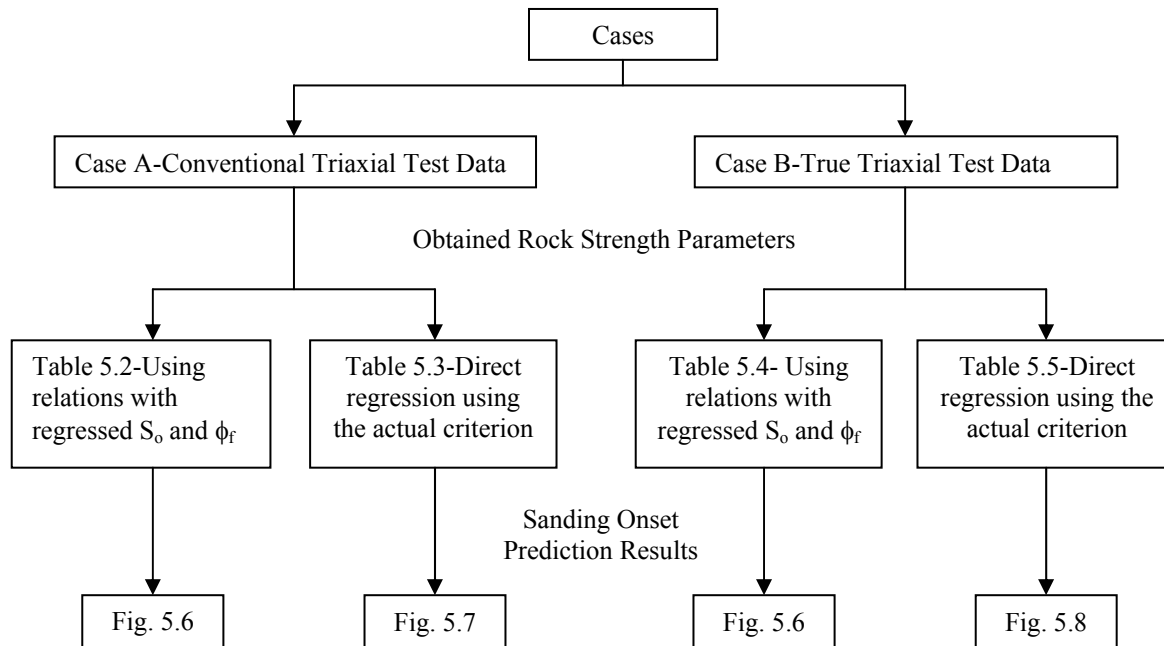


Figure 5.1 Comparison scheme in Chapter V

5.1 Rock Strength criterion

In this section, four most commonly used rock strength criteria in wellbore stability analysis and sand production prediction are presented.

5.1.1 Mohr-Coulomb criterion⁴⁹

Mohr-Coulomb failure criterion is the most commonly used strength criterion for geomaterials. According to the Mohr-Coulomb criterion, the shear strength increases with increasing normal stress on the failure plane. It can be represented by the following equation, see also Fig. 5.2,

$$\tau = S_o + \sigma \tan \phi_f \quad (5.1)$$

where τ is the shear stress, σ is the normal stress, S_o is the cohesive strength and ϕ_f is the internal frictional angle.

The Mohr-Coulomb criterion can be written in terms of principal stresses, which results in

$$\frac{\sigma_1 - \sigma_3}{2} = \frac{\sigma_1 + \sigma_3}{2} \sin \phi_f + S_o \cos \phi_f \quad (5.2)$$

in which σ_1 is the maximum principal stress and σ_3 is the minimum principal stress.

The failure function F is

$$F = \frac{\sigma_1 + \sigma_3}{2} \sin \phi_f + S_o \cos \phi_f - \frac{\sigma_1 - \sigma_3}{2} \quad (5.3)$$

Failure occurs when $F \leq 0$;

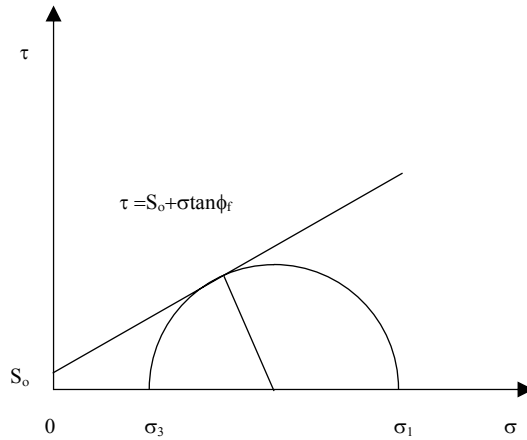


Figure 5.2 Mohr-Coulomb strength criterion

5.1.2 Hoek-Brown criterion⁵⁷

Hoek & Brown⁵⁷ studied the published experimental results of a wide variety of rocks and proposed the following strength criterion,

$$\frac{\sigma_1}{C_o} = \frac{\sigma_3}{C_o} + \sqrt{s_H + m_H \frac{\sigma_3}{C_o}} \quad (5.4)$$

where m_H and s_H are constants which depend on the properties of the rock and on the extent to which it has been broken before being subject to the stresses. Parameter

$s_H \begin{cases} = 1 & \text{for intact rock} \\ < 1 & \text{for previously broken rock} \end{cases}$. We assume $s_H=1$ in this study. C_o is the

Uniaxial Compressive Strength (UCS) of the intact rock in the specimen. C_o is related to the Mohr-Coulomb parameters through the following expression

$$C_o = \frac{2S_o \cos \phi_r}{1 - \sin \phi_r} \quad (5.5)$$

The failure function is

$$F = \frac{\sigma_3}{C_o} - \frac{\sigma_1}{C_o} + \sqrt{s_H + m_H \frac{\sigma_3}{C_o}} \quad (5.6)$$

Failure occurs if $F \leq 0$.

Mohr-Coulomb and Hoek-Brown criteria are only dependent on the maximum and minimum principal stresses. The effect of intermediate principal stress is not considered. The Mohr-Coulomb criterion is linear with σ_3 while the Hoek-Brown criterion is nonlinear. Application of Hoek-Brown criterion in sand production prediction is considered in reference⁴².

5.1.3 Drucker-Prager criterion⁵⁸

An approximation to the Mohr-Coulomb criterion was presented by Drucker and Prager⁵⁸ as an extended Mohr-Coulomb rule that employs the Von Mises criterion often used for ductile metals. It has the form

$$\alpha_D I_1 + k_D = \sqrt{J_2} \quad (5.7)$$

where

$$I_1 = \sigma_1 + \sigma_2 + \sigma_3 \quad (5.8)$$

which is the first invariant of a stress tensor.

$$J_2 = \frac{1}{6} [(\sigma_1 - \sigma_2)^2 + (\sigma_2 - \sigma_3)^2 + (\sigma_1 - \sigma_3)^2] \quad (5.9)$$

which is the second invariant of a stress deviator tensor.

The failure function is

$$F = \alpha_D I_1 + k_D - \sqrt{J_2} \quad (5.10)$$

Failure occurs if $F \leq 0$;

The material constants in Drucker-Prager criterion can be determined by matching two particular points with those of the Mohr-Coulomb criterion, and thus the two constants, α_D and k_D , can be expressed in terms of the Mohr-Coulomb parameters S_o and ϕ_f .

In 3D stress matching, if the points are selected in such a way that the failure surface circumscribes the Mohr-Coulomb hexagonal pyramid, see **Fig. 5.3**, the material constants are⁴⁹

$$\alpha_D = \frac{2 \sin \phi_f}{\sqrt{3}(3 - \sin \phi_f)} \quad (5.11)$$

$$k_D = \frac{6S_o \cos \phi_f}{\sqrt{3}(3 - \sin \phi_f)} \quad (5.12)$$

The matching points may also be selected in such a way that the failure surface touches the other 3 apexes, see **Fig 5.3**. In this case, the material constants are⁴⁹

$$\alpha_D = \frac{2 \sin \phi_f}{\sqrt{3}(3 + \sin \phi_f)} \quad (5.13)$$

$$k_D = \frac{6S_o \cos \phi_f}{\sqrt{3}(3 + \sin \phi_f)} \quad (5.14)$$

If the Drucker-Prager and Mohr-Coulomb criteria are expected to give identical limit loads for plane strain case, the material constants can be determined as⁴⁹

$$\alpha_D = \frac{\tan \phi_f}{\sqrt{9 + 12 \tan^2 \phi_f}} \quad (5.15)$$

$$k_D = \frac{3S_o}{\sqrt{9 + 12 \tan^2 \phi_f}} \quad (5.16)$$

Under this condition, the Drucker-Prager failure surface inscribes the Mohr-Coulomb failure surface, see **Fig. 5.3**.

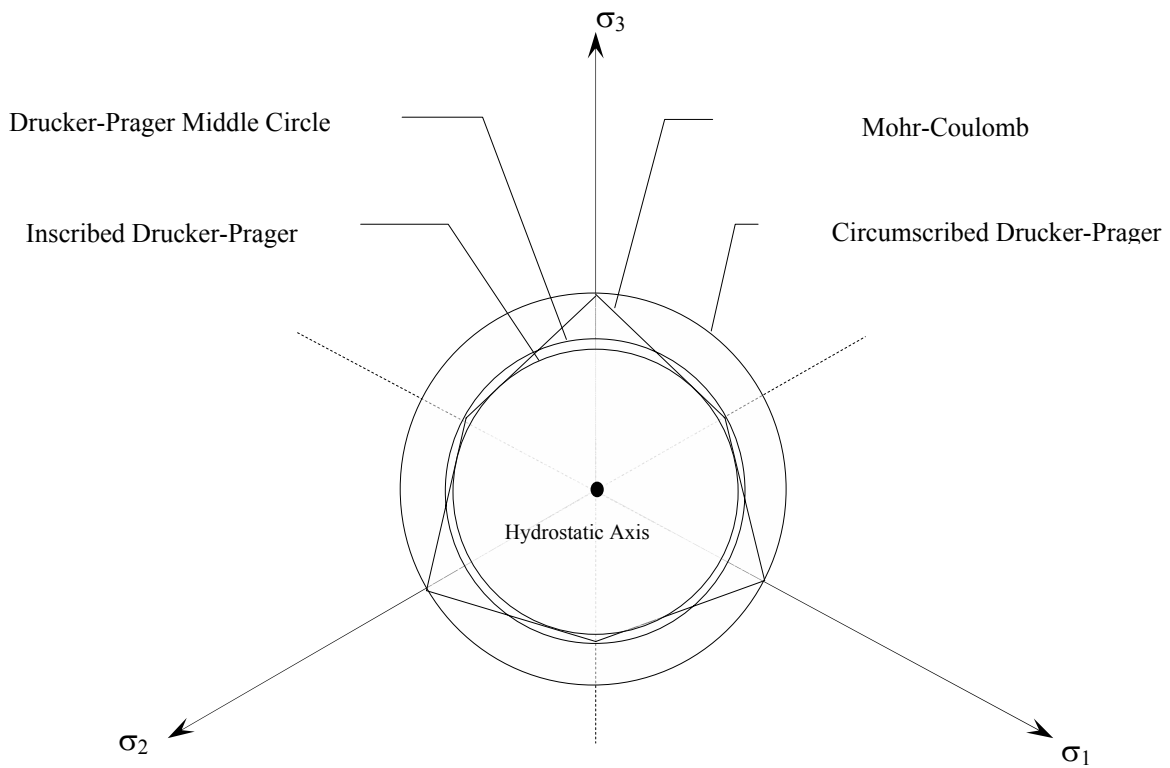


Figure 5.3 Failure envelopes projected on the π -plane for Mohr-Coulomb criterion, circumscribed Drucker-Prager criterion, inscribed Drucker-Prager criterion and Drucker-Prager middle circle

5.1.4 Modified Lade criterion⁴³

The modified Lade criterion was proposed by Ewy⁴³ based on Lade criterion⁵⁹. Application of this criterion in sand production is also shown by Ewy *et al.*⁴⁴. The criterion can be written as

$$\frac{I_1^{n3}}{I_3^n} = 27 + \eta_L \quad (5.17)$$

where

$$I_1^n = (\sigma_1 + S_L) + (\sigma_2 + S_L) + (\sigma_3 + S_L) \quad (5.18)$$

$$I_3^n = (\sigma_1 + S_L)(\sigma_2 + S_L)(\sigma_3 + S_L) \quad (5.19)$$

and

$$S_L = \frac{S_o}{\tan \phi_f} \quad (5.20)$$

$$\eta_L = \frac{4 \tan^2 \phi_f (9 - 7 \sin \phi_f)}{1 - \sin \phi_f} \quad (5.21)$$

The failure function is

$$F = 27 + \eta_L - \frac{I_1^{n3}}{I_3^n} \quad (5.22)$$

Failure occurs if $F \leq 0$;

5.2 Near wellbore poroelastic stress model

Combining the fluid flow model and the poroelastic stress model with appropriate boundary conditions, we determine the stress state using the Finite Element Method

(FEM) for a given well production condition as a function of time. In this chapter, we used an axisymmetric version of the fluid flow and stress models illustrated in Chapter IV.

5.3 Determination of rock strength criterion parameters

From the above listed rock strength criteria, we note that there are two parameters involved in each criterion (in Hoek-Brown, s_H has been assumed to be unity). We need to run laboratory tests to determine those parameters for a specific rock. Among the listed rock strength criteria, Mohr-Coulomb and Hoek-Brown criteria are intermediate principal stress independent (σ_2 -independent) while Drucker-Prager and Modified Lade criteria are intermediate principal stress dependent (σ_2 -dependent). If we know that the formation rock satisfies any of the σ_2 -independent strength criteria, then we need to run only conventional triaxial tests ($\sigma_1 > \sigma_2 = \sigma_3$). Otherwise, true triaxial tests ($\sigma_1 > \sigma_2 > \sigma_3$) are needed. However, in reality, we do not know which criterion the formation rock satisfies until proven by laboratory tests. True triaxial test data can always be used to determine which criterion best describes the formation rock strength. However, for many reasons, conventional triaxial test data are commonly used but true triaxial test data are rarely available for petroleum engineering usage. Besides, the procedure used to process the conventional triaxial test data is frequently regressing for the Mohr-Coulomb criterion parameters like cohesion S_o and internal friction angle ϕ_f through the σ_1 , σ_3 plot, and then deriving the parameters in other strength criteria through their relation with the Mohr-Coulomb parameters, see equations (5.11-5.16, 5.20-5.21). Even if there are relations between Mohr-Coulomb parameters and the parameters in the other criteria, the relations are not based directly on laboratory test data. We recommend direct regression of the test data for each different rock strength criterion.

To support our recommendation, in this section, we demonstrate the following: 1) Using conventional triaxial test data, the rock strength criteria parameters obtained from the regressed Mohr-Coulomb parameters and from direct regression of the test data are

different. Consequently, the approach used in processing laboratory test data does matter. 2) Using true triaxial test data which give the same regressed Mohr-Coulomb parameters as before, we demonstrate that the rock strength criteria parameters obtained from direct regression of the test data are different from those obtained using conventional triaxial test data.

In order to avoid the complicated regression process (interested reader should refer to [60-61]), we use just two assumed strength data points in two cases, see **Table 5.1**, to illustrate our ideas. As a result, it is important to mention that, in this chapter, all the rock strength criterion parameters are calculated from assumed data points instead of regressed from actual test data points. In Case A, we use one uniaxial compressive test data point and one conventional triaxial test data point. In Case B, we use one uniaxial compressive test data point and one true triaxial test data point. These data are assumed such that they provide same regressed Mohr-Coulomb parameters S_0 and ϕ_f in order to compare the results obtained in Case A and B.

Table 5.1 Assumed rock strength test data points

Case A-Conventional Triaxial Test				Case B-True Triaxial Test			
Experiment	σ_1 (psi)	σ_2 (psi)	σ_3 (psi)	Experiment	σ_1 (psi)	σ_2 (psi)	σ_3 (psi)
Uniaxial Compression	2,425	0	0	Uniaxial Compression	2,425	0	0
Conven. Triaxial Compression	4,525	700	700	True Triaxial Compression	3,025	500	200

For Case A, if we first calculate the Mohr-Coulomb parameters S_o and ϕ_f , and then use S_o and ϕ_f to calculate rock strength criterion parameters in other criteria using equations (5.11-5.16, 5.20-5.21), we obtain **Table 5.2**. If we calculate the parameters in each strength criterion directly from the assumed test data without using equations (5.11-5.16, 5.20-5.21), we obtain **Table 5.3**. Similarly, we obtain **Table 5.4** and **Table 5.5** for Case B.

Table 5.2 Strength criterion parameters for Case A-Derived from regressed Mohr-Coulomb S_o and ϕ_f

Strength Criterion	α_D	k_D (psi)	S_L (psi)	η_L	S_o (psi)	ϕ_f (Degree)	C_o (psi)	m_H
Mohr-Coulomb					700	30		-
Hoek-Brown*							2,425	5.15
D-P-Cirm. Circle	0.23094	840						
D-P -Ins. Circle	0.16013	582.44						
D-P -Middle Circle	0.16496	600						
Modified Lade			1,212.44	14.67				

* m_H and C_o are directly calculated without using Mohr-Coulomb S_o and ϕ_f

Table 5.3 Strength criterion parameters for Case A- Calculated directly from the two assumed test data points (Compare with **Table 5.2**)

Strength Criterion	α_D	k_D (psi)	S_L (psi)	η_L	S_o (psi)	ϕ_f (Degree)	C_o (psi)	m_H
Mohr-Coulomb					700	30		
Hoek-Brown*							2,425	5.15
D-P-Cirm. Circle	0.23094	840						
D-P -Ins. Circle	0.23094	840						
D-P -Middle Circle	0.23094	840						
Modified Lade			1,212.44	14.67				

* m_H and C_o are directly calculated without using Mohr-Coulomb S_o and ϕ_f

Table 5.4 Strength criterion parameters for Case B-Derived from regressed Mohr-Coulomb S_o and ϕ_r

Strength Criterion	α_D	k_D (psi)	S_L (psi)	η_L	S_o (psi)	ϕ_r (Degree)	C_o (psi)	m_H
Mohr-Coulomb					700	30		-
Hoek-Brown*							2,425	4.33
D-P-Cirm. Circle	0.23094	840						
D-P -Ins. Circle	0.16013	582.44						
D-P -Middle Circle	0.16496	600						
Modified Lade			1,212.44	14.67				

* m_H and C_o are directly calculated without using Mohr-Coulomb S_o and ϕ_r

Table 5.5 Strength criterion parameters for Case B- Calculated directly from the two assumed test data points (Compare with **Table 5.4**)

Strength Criterion	α_D	k_D (psi)	S_L (psi)	η_L	S_o (psi)	ϕ_f (Degree)	C_o (psi)	m_H
Mohr-Coulomb					700	30		
Hoek-Brown*							2,425	4.33
D-P-Cirm. Circle	0.11662	1,117.21						
D-P -Ins. Circle	0.11662	1,117.21						
D-P -Middle Circle	0.11662	1,117.21						
Modified Lade			2,048.06	3.45				

* m_H and C_o are directly calculated without using Mohr-Coulomb S_o and ϕ_f

From the results in **Tables 5.2-5.5**, we see that the procedure used in processing laboratory test data is important for evaluating rock strength parameters. We strongly recommend using direct regression based on laboratory test data to evaluate rock strength parameters.

In the following section, we show how the sanding onset prediction results are affected by the methodology of obtaining the parameters in rock strength criterion.

5.4 Application of rock strength criterion in sand production prediction

As indicated in Chapter III, sand production may be caused by a high production rate, which leads to near-wellbore formation rock tensile failure³⁹. It may also be induced by the increase of near-wellbore effective stress during the depletion of a reservoir, which causes near-wellbore formation rock shear failure¹²⁻¹³. In this chapter, we assume that sand production is caused by near wellbore formation rock shear failure.

We consider a hypothetical vertical gas well with the parameters given in **Table 5.6**. The well produces first at constant rate and then at constant pressure after the bottomhole flowing pressure reaches the allowed minimum value. The variation of average reservoir pressure and bottomhole flowing pressure etc. with production time is shown in **Fig. 5.4**. If the formation rock behaves linear elastically, the variation of wellbore surface principal effective stresses with production time is calculated as shown in **Fig. 5.5**. However, it is more likely that the formation rock behaves as an elastoplastic material. If a specific strength criterion is used, we predict when the near wellbore area fails and leads to sand production. In this section, we show how the sanding onset prediction results vary with the methodology of obtaining the parameters in the rock strength criterion.

For Case A, when only conventional laboratory measurements are available, we have calculated the rock strength criteria parameters using two different methodologies. Using parameters in **Table 5.2**, which is derived by first calculating the Mohr-Coulomb parameters S_o and ϕ_f , and then using S_o and ϕ_f to calculate rock strength criterion parameters in other criteria using equations (5.11-5.16, 5.20-5.21), we predict the specific production time when sand production occurs, in addition to other data such as drawdown (the difference between average reservoir pressure and bottom hole flowing pressure) and total drawdown (the difference between initial reservoir pressure and bottom hole flowing pressure) at the onset of sand production. Those sanding parameters obtained by using different strength criteria are illustrated in **Fig. 5.6**. Obviously, the variation of predicted onset of sanding with the applied strength criterion is too large.

Table 5.6 Well, reservoir and production parameters used in studying the effect of rock strength criterion on sand production

Wellbore Radius (ft)	0.5
Drainage Radius (ft)	2,000
Reservoir Thickness (ft)	20
Total Production Time (yrs)	12
Gas Specific Gravity (fraction)	0.7
Reservoir Temperature (°F)	108
Initial Reservoir Pressure (psi)	2800
Permeability (mD)	10
Porosity (fraction)	0.12
Initial Production Rate (Mscf/Day)	1250
Minimum BHP (psi)	500
Young Modulus (psi)	1.4e6
Poisson's Ratio (fraction)	0.3
Biot's Constant (fraction)	1.0
Horizontal Stress (psi)	3060
Vertical Stress (psi)	3400

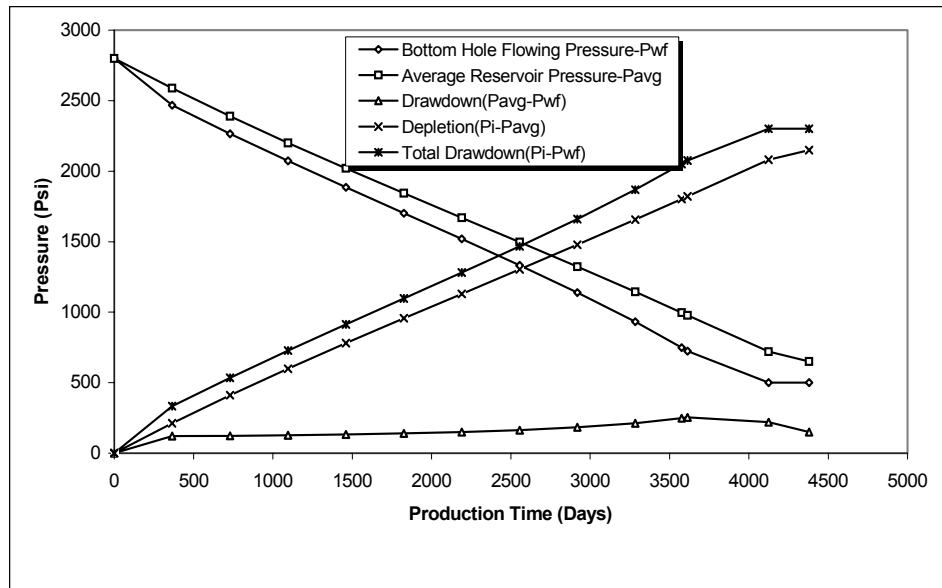


Figure 5.4 Pressure change with time during gas production

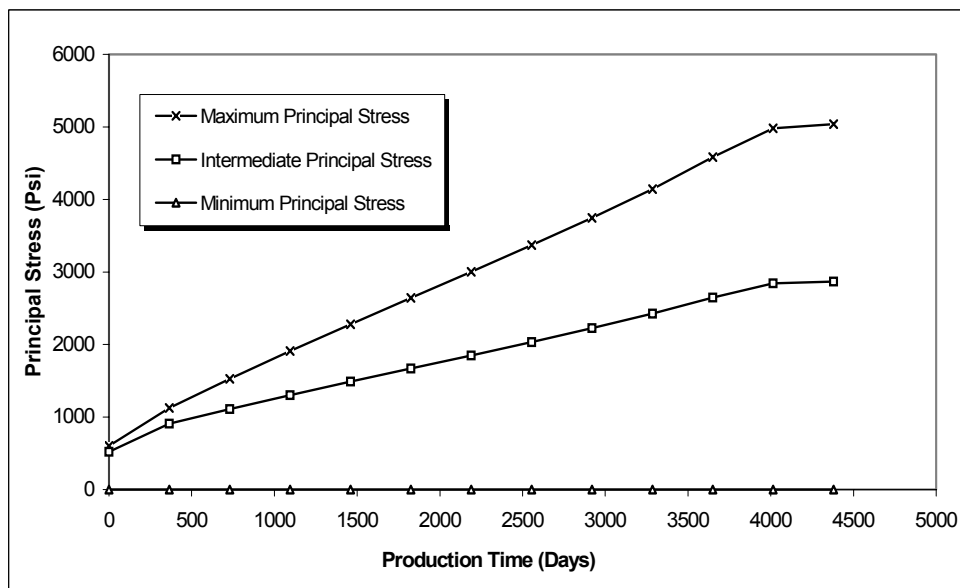


Figure 5.5 Wellbore surface principal effective stresses change with production time assuming linear elasticity

However, if we use parameters in **Table 5.3**, which are calculated directly from the test data without using equations (5.11-5.16, 5.20-5.21), we obtain a different set of sanding onset data, see **Fig. 5.7**. Comparison of **Fig. 5.6** and **Fig. 5.7** indicates that the sanding onset prediction differences for various versions of the Drucker-Prager criterion are eliminated if the rock strength criterion parameters are obtained by direct regression of the laboratory test data. This is because in the Drucker-Prager criterion there are only two parameters, α_D and k_D , available for regressing. Therefore, using the same test data, regression can only lead to the same set of α_D and k_D even for different versions of the Drucker-Prager criteria.

In the same way, we can obtain two different sanding onset prediction results for Case B. If we use the rock strength criterion parameters in **Table 5.4**, we arrive at the sanding prediction results exactly the same as those in **Fig. 5.6**. If we use the rock strength criterion parameters in **Table 5.5**, we get different sanding prediction results, see **Fig. 5.8**. The sanding prediction results differ from each strength criterion much less than that in **Fig. 5.7** due to the fact that we use one true triaxial test data point in Case B and use our recommended methodology to process the test data points. Some difference still exists because the shape of each strength criterion surface in the 3D principal stress space is different.

In **Figs. 5.6-5.8**, we notice that the Mohr-Coulomb and Hoek-Brown criteria provide the same sanding onset prediction results. This is because the Biot's constant is taken to be unity in our study and the minimum principal stress σ_3 is zero.

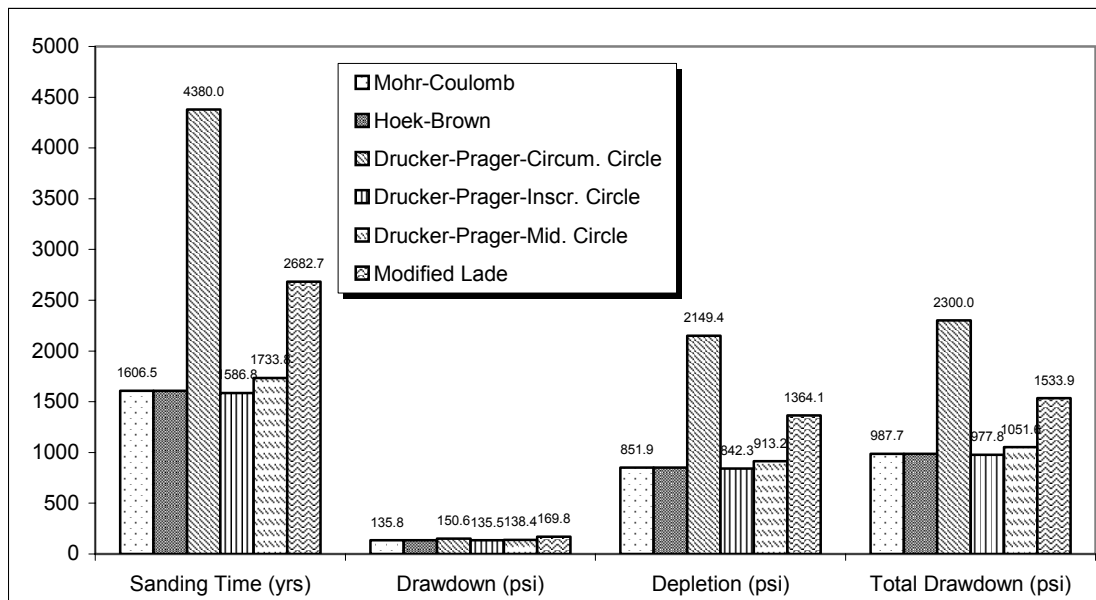


Figure 5.6 Predicted sanding onset results using different rock strength criteria for rock data in Case A & B, with rock strength parameters from **Tables 5.2** and **5.4** respectively.

Since **Tables 5.2** and **5.4** are essentially the same, the sanding onset prediction results are exactly the same for both cases. Sanding onset prediction indicates that no sanding occurs if the Circumscribed Drucker-Prager criterion is used for both cases, data for this criterion in this graph is at production time=12 yrs.

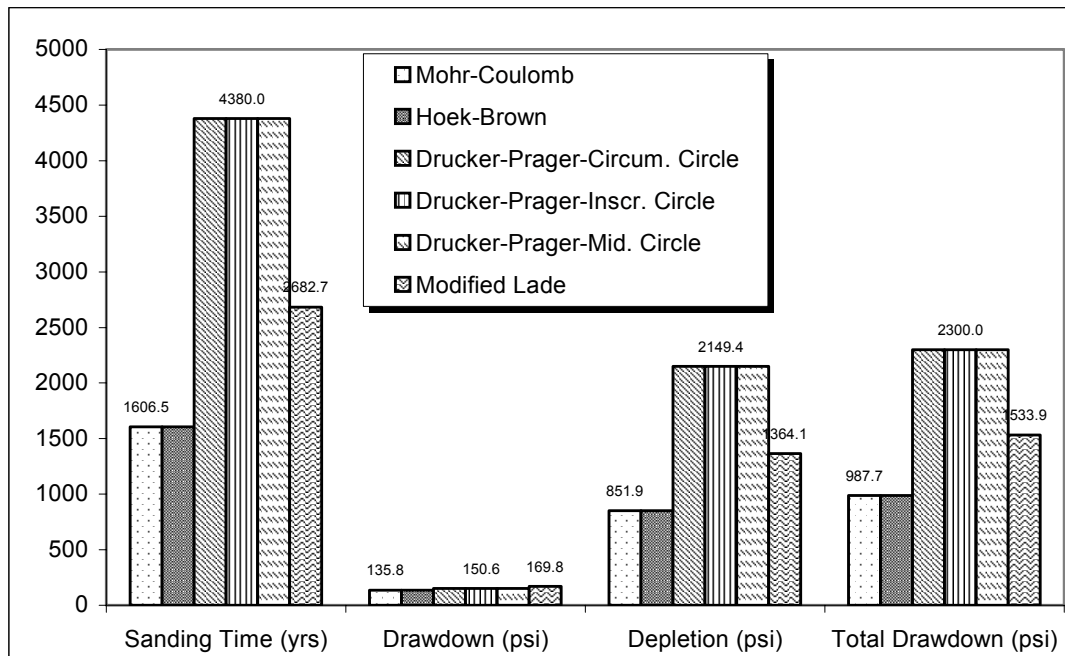


Figure 5.7 Predicted sanding onset results using different rock strength criteria for test data in Case A, with rock strength parameters from **Table 5.3**. Predicted sanding onset results for three versions of Drucker-Prager criteria are the same because the parameters α_D and k_D are the same for different versions of Drucker-Prager criterion. Since sanding onset prediction indicates that no sanding occurs if the three Drucker-Prager criteria are used, data for the criteria in this graph are at production time=12 yrs.

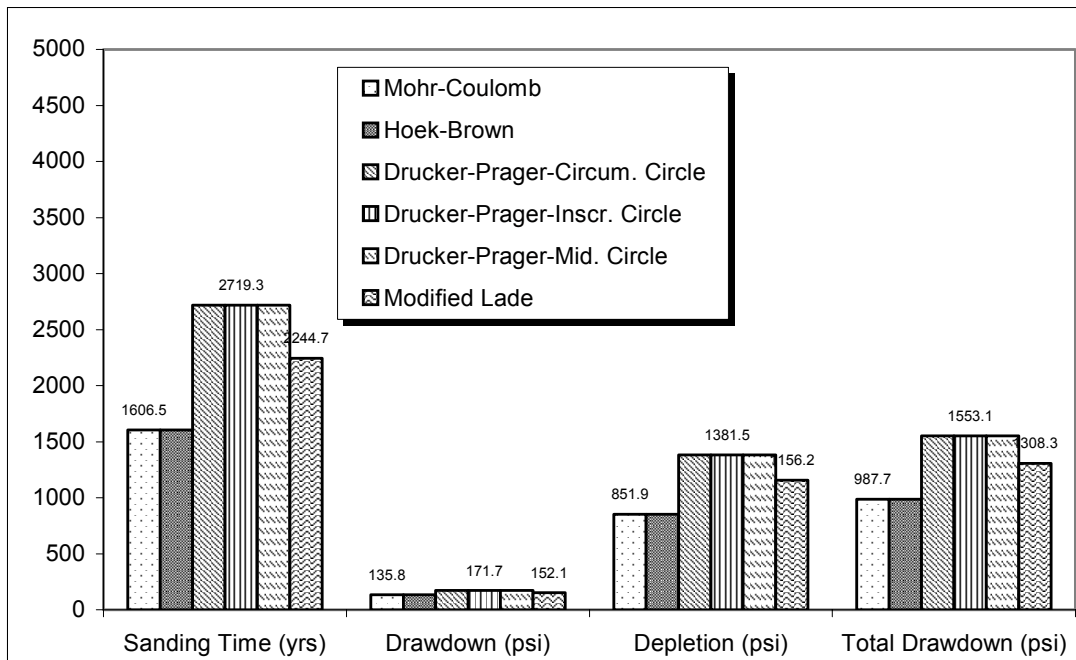


Figure 5.8 Predicted sanding onset results using different rock strength criteria for rock test data in Case B, with rock strength parameters from **Table 5.5**.

From the above work, we conclude and recommend the following

- (1) Of the approaches considered, the best way to evaluate the rock strength criterion parameters is to perform direct regression of the laboratory test data. Using the regressed Mohr-Coulomb parameters to calculate the rock strength parameters in the other criteria is not recommended.
- (2) Using the methodology proposed in this chapter, the uncertainties of the effect of rock strength criterion on sand production prediction are reduced.

CHAPTER VI

SANDING ONSET PREDICTION CASE STUDIES

6.1 Sand production in gas fields in the Northern and Central Adriatic Sea

The Northern and Central portions of the Adriatic Sea stretching from the gulf of Venice to Ancona make up a single geological unit called the Northern Adriatic Basin, see **Fig. 6.1**. Geological studies indicate that this basin is a typical case of normally compacted stratigraphic sequences. The strength of the reservoir rocks results exclusively from the compaction of the sand grains and was found to be strongly correlated to depth as a direct consequence of burial. Detailed geological description of this basin can be found in reference⁶²⁻⁶³.

To develop a sanding onset prediction model which can be used at a regional level. Sand production data for 31 wells belonging to 9 fields are studied, see **Table 6.1** and **Table 6.2**. **Table 6.1** lists 23 wells with sanding problem under the given condition. **Table 6.2** lists 8 wells without sanding problem under the given condition. In the literature, Moricca *et al.*⁶³ obtained a sanding onset prediction criterion based on regression of the sand producing wells data. Sanfilippo *et al.*⁵⁰ modified the Risnes *et al.*¹⁸ model to find a sanding onset prediction model. In this modified Risnes model, it is assumed that the fluid pressure gradient can be ignored. In their work, it is found that sanding occurs when the plastic zone radius reaches 2.15 times the wellbore radius. Tronvoll *et al.*⁶⁴ provided an empirical sand production criterion through examining the field data and laboratory cavity failure test data. Kanj and Abousleiman⁶⁵ used artificial neural network model to predict the onset of sand production. From the aforementioned methods, we notice that the proposed sanding production criterion does not explain the sanding mechanism and is not validated by wells without producing sand.



Figure 6.1 The Northern Adriatic Basin⁶³

Table 6.1 Northern Adriatic gas wells where sand production was observed under the given condition⁶³

Well No.	Well Name	TVD	S _o	BHSP	BHFP
		ft	psi	psi	psi
1	AG 14C	10,465.88	312.91	2,289.96	1,894.55
2	AG 19C	10,439.63	311.49	2,233.06	1,996.96
3	AM 8L	11,043.31	351.32	2,490.51	2,221.69
4	AM 8L	11,965.22	421.01	3,009.66	2,187.55
5	AN 7L	14,921.26	756.68	3,811.86	2,974.10

Table 6.1 Continued

6	AN 9L	13,412.07	561.82	2,716.66	2,090.83
7	AZ 9C	6,889.76	153.61	2,403.74	2,277.16
8	AZ 13C	6,332.02	137.97	2,655.50	2,496.20
9	AZ 13L	7,017.72	157.88	2,725.19	2,638.43
10	AZ 15L	7,808.40	184.90	2,281.42	1,607.24
11	BA 5L	3,681.10	81.07	1,635.68	1,521.90
12	BA 6L	4,396.33	93.87	2,005.49	1,800.67
13	BA 13C	3,510.50	78.23	1,486.34	1,476.38
14	BA 7C	6,299.21	136.54	4,693.70	3,527.39
15	BA 7L	8,300.53	203.39	5,689.34	4,298.29
16	BA 8C	5,380.58	113.79	3,353.86	2,688.21
17	BA 8L	6,988.19	156.46	4,267.00	3,816.12
18	CE 15L	11,991.47	423.86	4,220.06	4,090.63
19	CE 16L	12,034.12	426.70	4,003.87	3,873.02
20	P80 34S	4,301.18	92.45	1,280.10	1,244.12
21	P80 36L	11,040.03	351.32	5,732.01	4,336.70
22	P80 39L	4,931.10	103.83	2,198.93	2,166.21
23	PG 23C	10,400.26	308.65	3,318.31	3,159.00

Table 6.2 Northern Adriatic gas wells where sand production was not observed under the given condition⁶³

Well No.	Well Name	TVD	So	BHSP	BHFP
		ft	psi	psi	psi
1	CE 7C	10,488.85	314.34	3,316.88	2,625.63
2	CE 7L	10,597.11	321.45	3,129.13	2,986.90
3	CE 11L	12,086.61	430.97	4,641.08	3,791.94
4	DO 9C	9,858.92	277.36	967.19	952.96
5	DO 21L	12,434.38	462.26	4,858.69	3,089.31
6	PMW 3L	9,022.31	234.69	3,624.11	3,581.44
7	PWA 16L	9,786.75	273.09	1,537.54	1,450.78
8	PG 26C	10,416.67	310.07	3,316.88	3,073.66

In this chapter, several analytical models presented in Chapter III are used to study the sanding problem in the Northern Adriatic Basin gas wells. If it is assumed that sanding is caused by shear failure around perforation tunnel or tip, we may use equation (3.10) and equation (3.35) to predict the critical bottom hole flowing pressure P_{wf} . The results are shown in **Fig. 6.2**. We see that the difference between predicted and field measured P_{wf} is too large. In the shear failure induced sanding criteria, it is implied that sand production is equal to shear failure. A more plausible sand production criterion is that sanding occurs once the stress near the cavity overcomes the tensile strength of the failed rock. If the rock cannot sustain tensile stress after shear failure, sanding occurs once

tensile stress is induced. If applied to perforation tunnel or perforation tip, the sand production criteria are equation (3.18) and equation (3.40) in Chapter III respectively, which are

For perforation tunnel,

$$\left. \frac{\partial P(r, t)}{\partial r} \right|_{r=R_w} = \frac{C_o}{R_w} \quad (6.1)$$

and for perforation tip

$$\left. \frac{\partial P(r, t)}{\partial r} \right|_{r=R_w} = 2 \frac{C_o}{R_w} \quad (6.2)$$

To develop a correlation between pressure gradient and pressure drawdown, a flow regime needs to be assumed. If we assume the flow is in steady state at onset of sanding and assume that the density of the produced gas is related to the pressure through the following power-law relation,

$$\rho_f = \gamma P^{m_d} \quad (6.3)$$

If we assume that sanding occurs at perforation tip when tensile stress is induced after shear failure, the sanding onset prediction model becomes the one derived by Weingarten and Perkins³⁹ and Ong *et al.*⁴⁰, which is

$$2C_o = \frac{(P_e^{m_d+1} - P_{wf}^{m_d+1})}{P_{wf}^{m_d}} \frac{1}{m_d + 1} \quad (6.4)$$

If it is assumed that sanding occurs at perforation tunnel when tensile stress is induced after shear failure, the criterion becomes

$$C_o \ln \frac{R_e}{R_w} = \frac{1}{m_d + 1} \left[\frac{P_e^{m_d+1} - P_{wf}^{m_d+1}}{P_{wf}^{m_d}} \right] \quad (6.5)$$

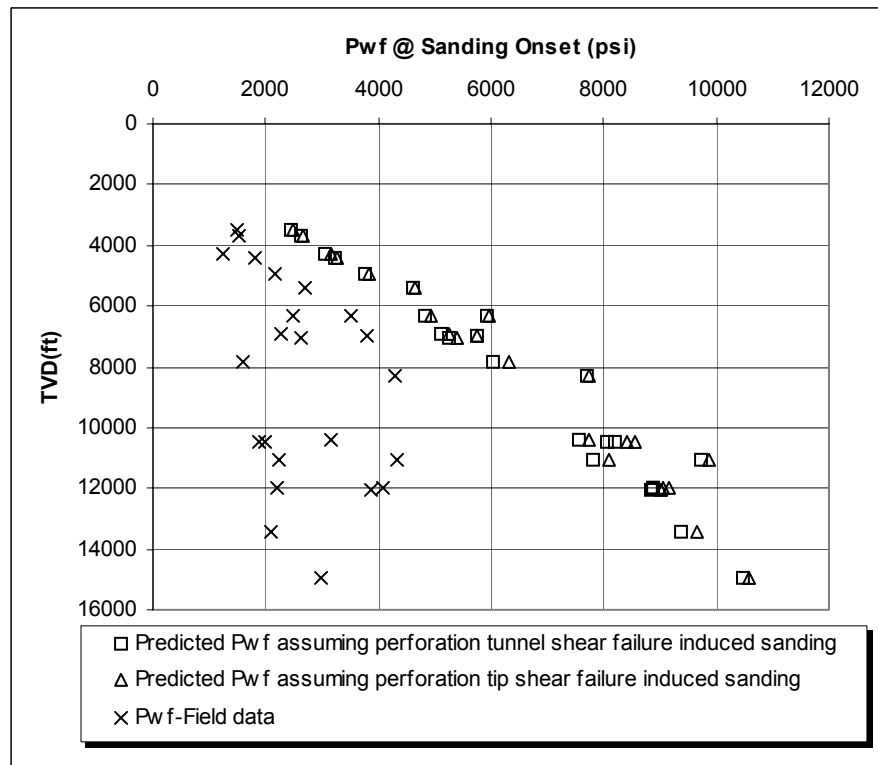


Figure 6.2 Comparison of predicted and field measured BHFP at sanding onset assuming perforation tunnel or perforation tip shear failure induced sanding

To use the above models, it is necessary first to determine the exponent m_d in equation (6.3). Using PVT analysis program, it is found that equation (6.3) gives good description of the density and pressure relation, see **Figs. 6.3** and **6.4**.

Since most of the well pressure is less than 4000 psi, from **Fig. 6.3** and **Fig. 6.4**, it is reasonable to take the density exponent m_d to be 1. Using equation (6.4), we obtain a predicted critical bottom hole flowing pressure, see **Fig. 6.5**.

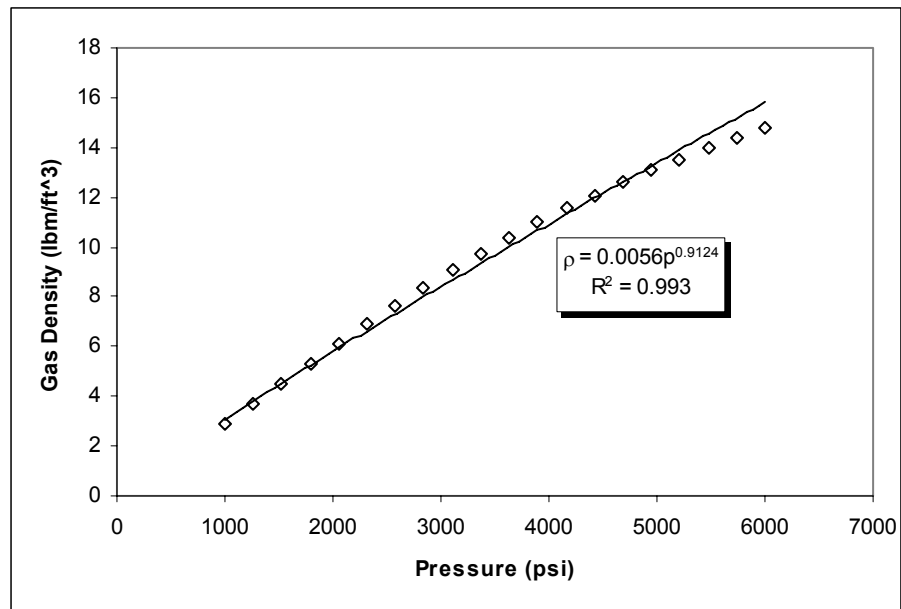


Figure 6.3 Gas density and pressure correlation in a wide pressure range

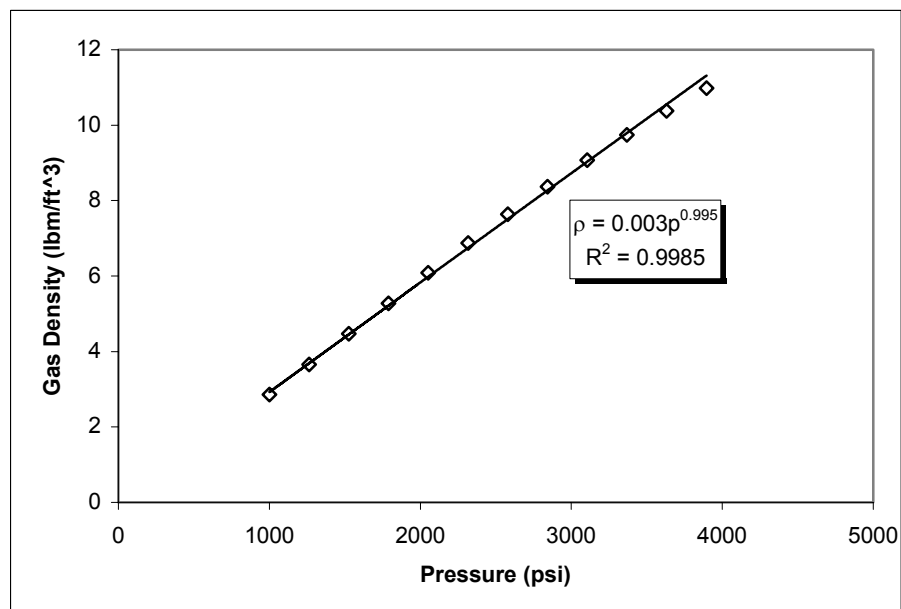


Figure 6.4 Gas density and pressure correlation in a narrower pressure range

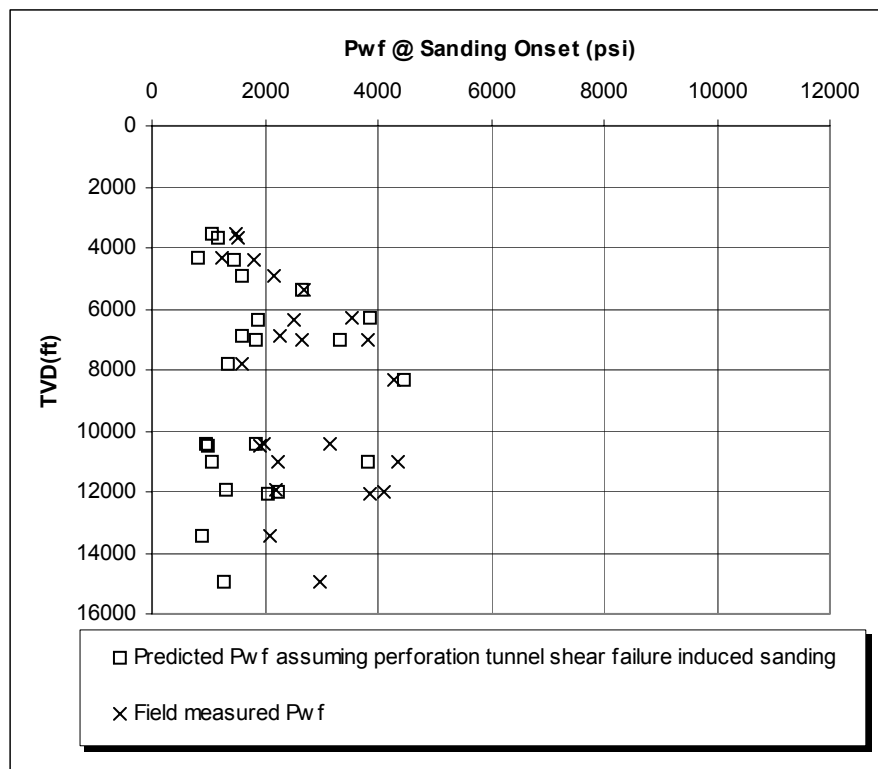


Figure 6.5 Predicted and field measured BHFP at sanding onset assuming perforation tip tensile stressed induced sanding

Comparison of the predicted and real critical P_{wf} is shown in **Fig. 6.6**. We see that this sanding onset prediction model provides a slightly optimistic estimation of the critical P_{wf} compared with the field data. But the prediction is reasonably good.

With this sanding onset prediction model, we check that if the other 8 wells produce sand or not. **Fig. 6.7** compared the predicted P_{wf} and real P_{wf} at which the wells do not produce sand. From **Fig. 6.7**, we see that the wells do not produce sand according to this model, which validates our sanding onset prediction model.

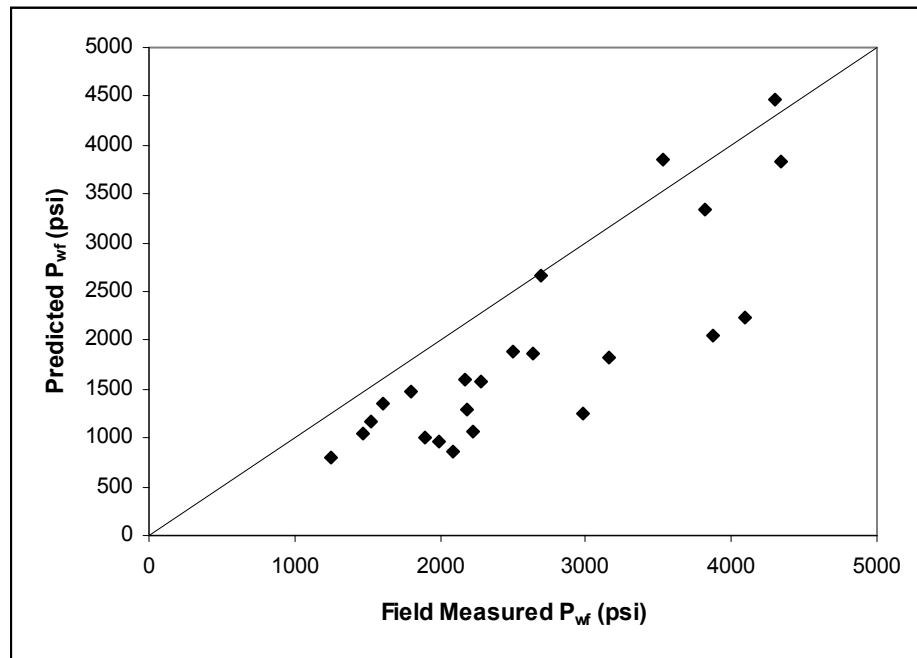


Figure 6.6 Comparison of predicted critical BHFP and field measured BHFP for 23 wells with sand production

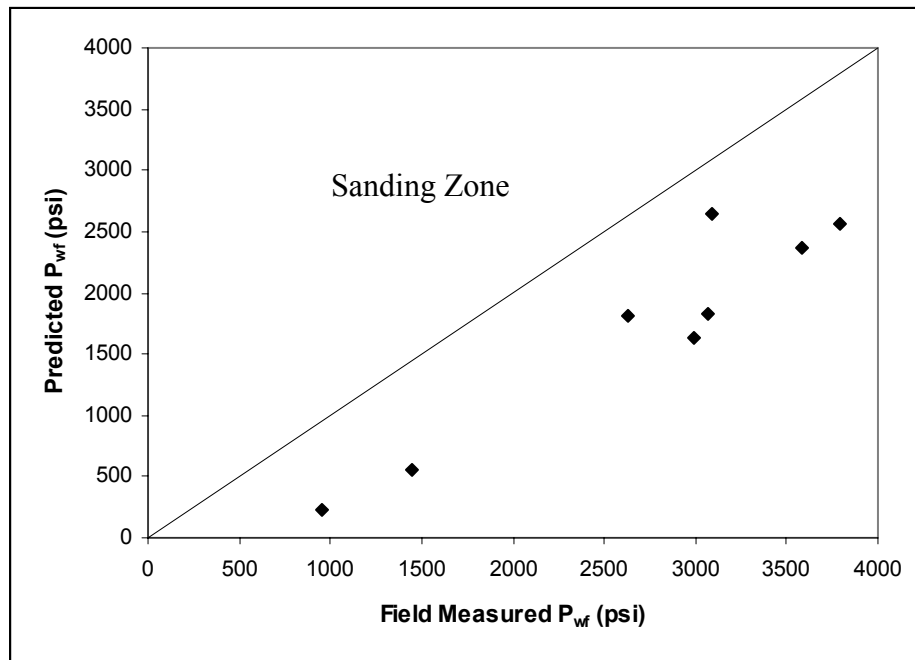
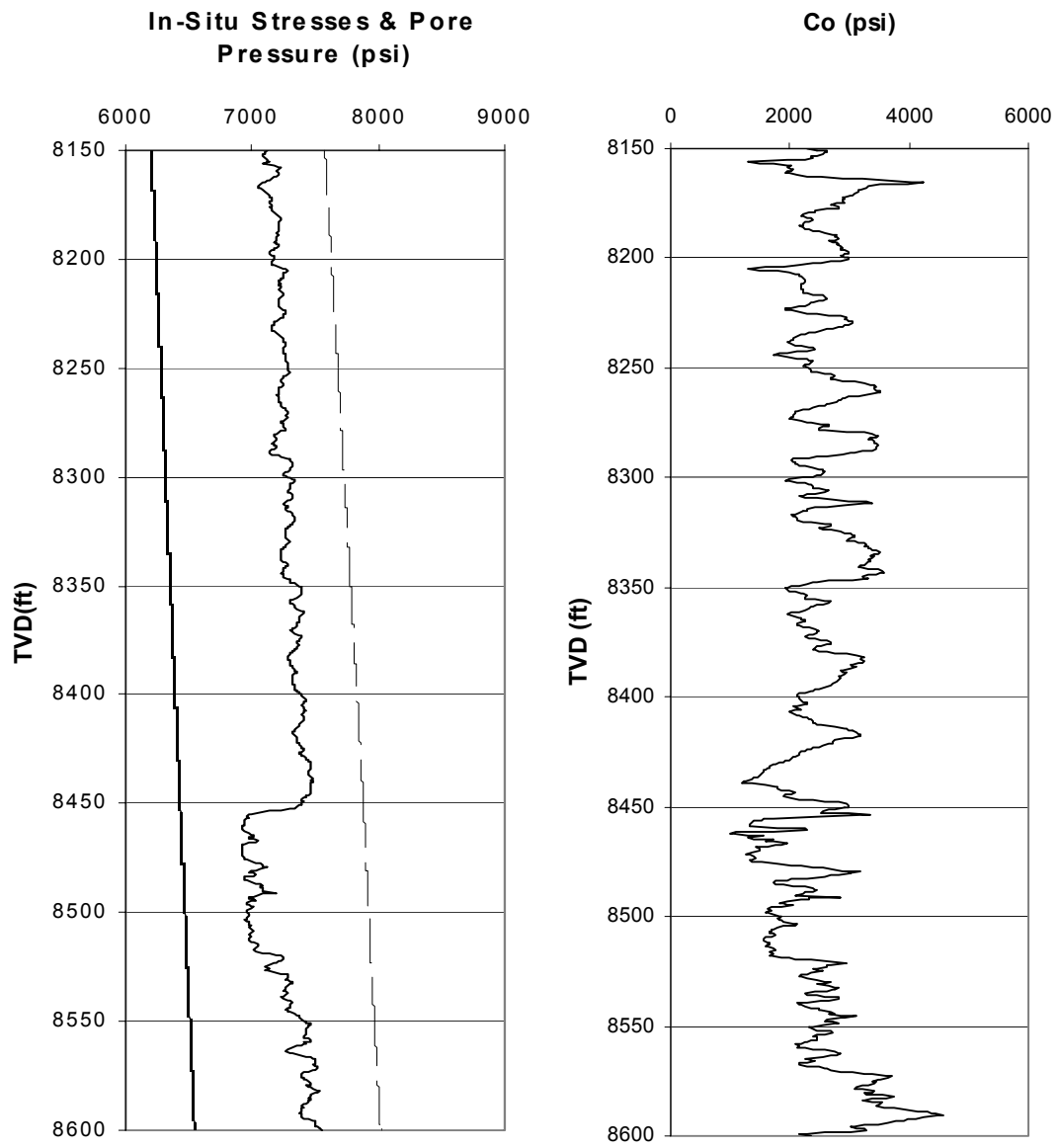


Figure 6.7 Comparison of predicted critical BHFP and field measured BHFP for 8 wells without sand production

6.2 Sand production in Well #3

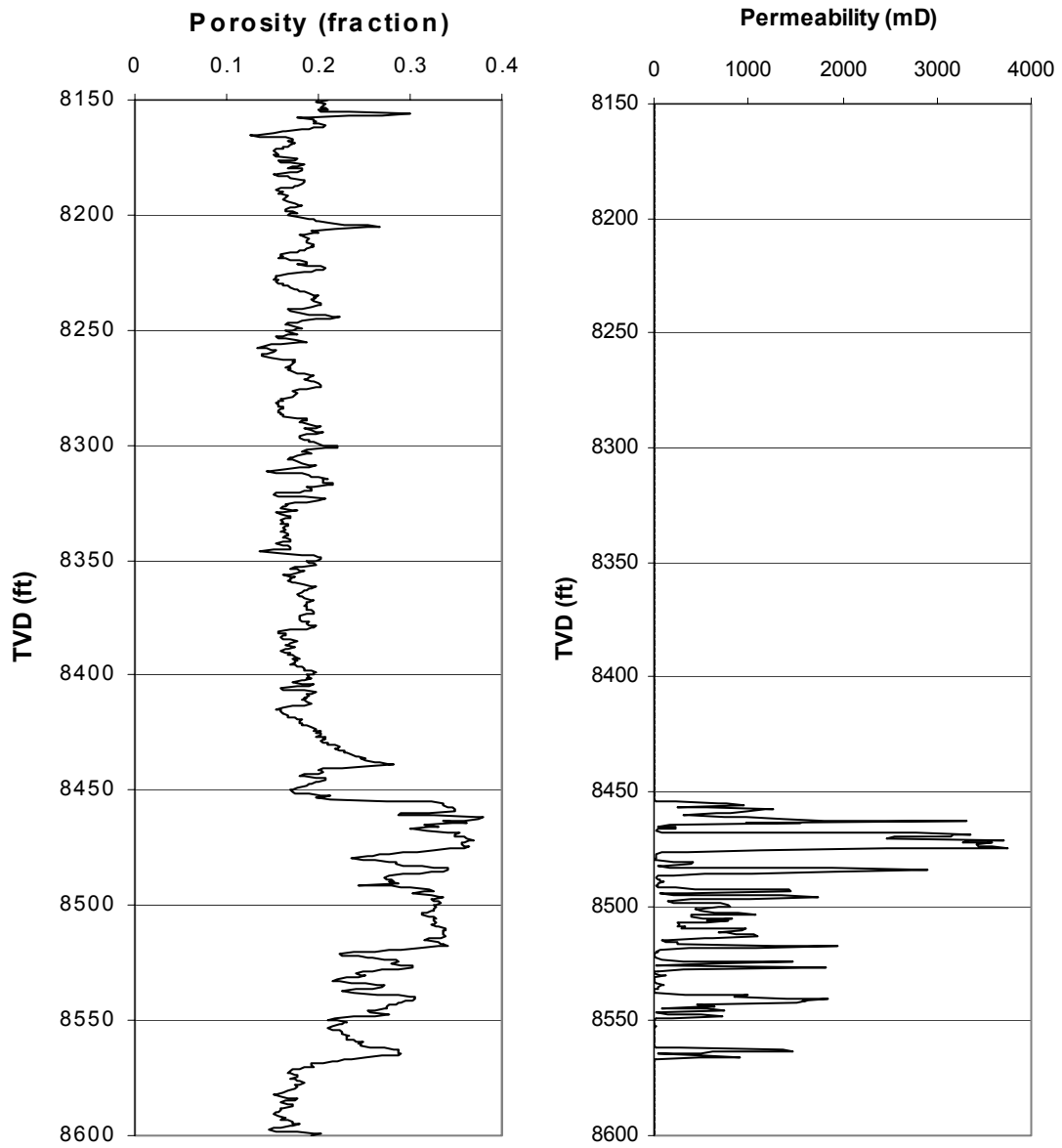
This well is cased and perforated from 8453 ft to 8458 ft. Field data indicates that sand production occurs at bottom hole flowing pressure $P_{wf}=5486$ psi and average reservoir pressure $\bar{P}=5508$ psi. Logging data for this well is available, see **Fig. 6.8**.



(a) In-situ stresses and pore pressure

(b) Uniaxial Compressive Strength

Figure 6.8 Logging data for well #3



(c) Porosity

(d) Permeability

Figure 6.8 Continued

In this well, if we assume that sanding is caused by tensile stress near perforation tip after shear failure, we obtain the critical bottom hole flowing pressure as shown in **Fig. 6.9**. We see a big difference between measured and predicted value. If we assume sanding is caused by shear failure at perforation tunnel or perforation tip, we obtain the sanding onset prediction results presented in **Fig. 6.10**. From **Fig. 6.10** we see that at depth 8456.5 ft, the well tend to produce sand. The predicted critical P_{wf} is 5446 psi while the real field measured critical P_{wf} is 5486 psi. This indicates that perforation tip shear failure might be the reason for sanding problem in this well.

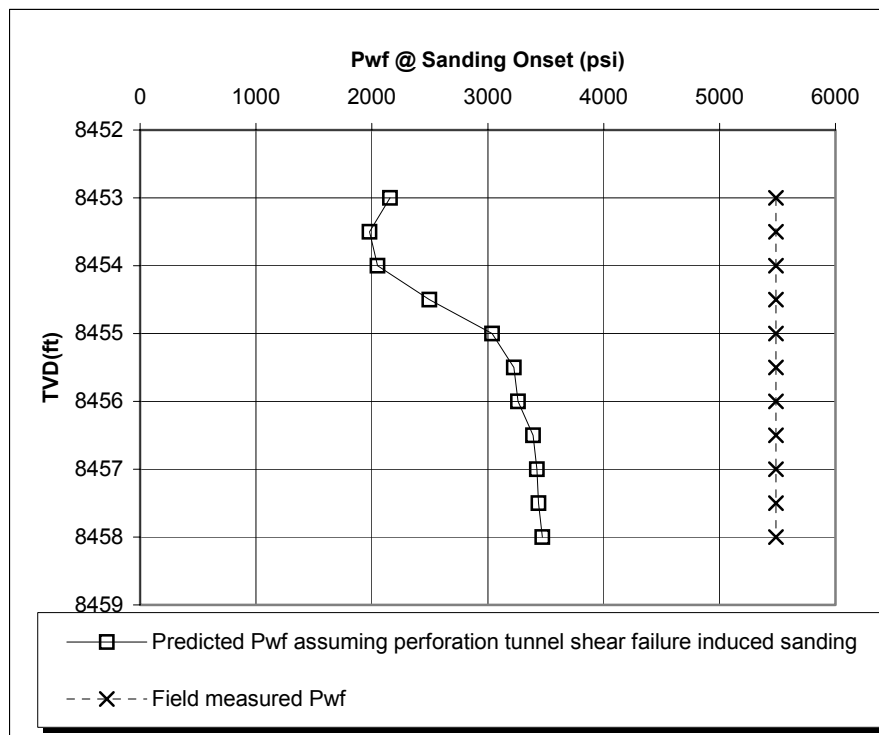


Figure 6.9 Predicted and field measured BHFP at sanding onset assuming perforation tip tensile stressed induced sanding

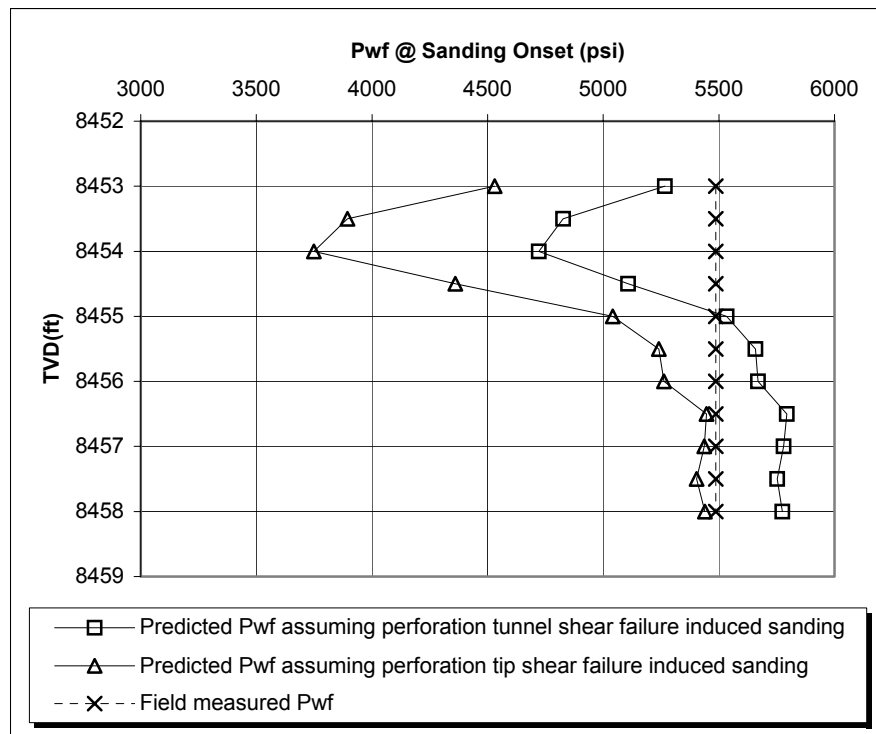


Figure 6.10 Comparison of predicted and field measured BHFP at sanding onset assuming perforation tunnel or perforation tip shear failure induced sanding

In summary, in this chapter,

- (1) We studied the Northern Adriatic Basin wells sanding cases. Through this study, we conclude that,
 - a. Sand production in Northern Adriatic Basin wells might be because of induced tensile stress at perforation tip after shear failure.

- b. The trend of sanding onset prediction results using this assumption is correct. The dispersion between predicted and field measured results is within reasonable limits.
- (2) Case study of sanding problem in Well #3 indicates that sanding might be caused by shear failure at perforation tip. Using this assumption, perfect agreement is reached between predicted and field measured P_{wf} at sanding onset.

CHAPTER VII

SUMMARY AND CONCLUSIONS

1. We derive an analytical poroelastoplastic stress model for thick-walled hollow cylinder model. Based on the thick-walled hollow cylinder model, we derive simple sanding onset prediction models assuming shear failure induced sanding and tensile stress induced sanding after shear failure. These models may be used to study sanding from open-hole well or perforation tunnel for cased well.
2. We derive an analytical poroelastoplastic stress model for thick-walled hollow sphere model. Based on the thick-walled hollow sphere model, we derive simple sanding onset prediction models assuming shear failure induced sanding and tensile stress induced sanding after shear failure. These models may be used to study sanding from perforation tip for cased well.
3. We derive an analytical poroelastic stress model for thick-walled hollow cylinder model under anisotropic in-situ stress condition. Based on this model, we derive sanding onset prediction model assuming shear failure induced sanding. This model may be used to study sanding from open-hole wells where the in-situ horizontal stresses are different.
4. We implement a 3D general finite element code for stress state simulation and single-phase fluid flow simulation. Its technical performance is checked against available analytical and numerical solutions.
5. We study the effect of rock strength criterion on sanding onset prediction. We propose that the best way to evaluate the rock strength criterion parameters is to perform direct regression of the laboratory test data. Using the regressed Mohr-Coulomb parameters to calculate the rock strength parameters in the other criteria is not recommended. Using this methodology, the uncertainties of the effect of rock strength criterion on sand production prediction are reduced.

6. We study the Northern Adriatic Basin wells sanding cases. Through this study, we conclude that sand production in Northern Adriatic Basin wells might be because of induced tensile stress at perforation tip after shear failure. We validate this conclusion by wells without sand production problem under the given conditions. Case study of sanding problem in Well#3 indicates that sanding might be caused by shear failure at perforation tip. Using this assumption, we reached perfect agreement between predicted and field measured bottom hole flowing pressure (P_{wf}) at sanding onset.

NOMENCLATURE

Variables

- A = area, L^2 , ft^2
 A_e = integration constants, dimensionless
 A_{ep} = integration constants, dimensionless
 B = strain-displacement matrix, L^{-1} , ft^{-1}
 B_e = integration constants, dimensionless
 B_{ep} = integration constants, dimensionless
 B_f = fluid formation volume factor, dimensionless
 C_1 = constant, $(m/Lt^2)^{-1}$, psi^{-1}
 C_2 = constant, $(m/Lt^2)^{-1}$, psi^{-1}
 C_3 = constant, L^{-m} , ft^{-m}
 C_4 = constant, L^{n+1} , ft^{n+1}
 C_f = fluid compressibility, $(m/Lt^2)^{-1}$, psi^{-1}
 C_{hc} = constant, $m/L^{1-m}t^2$, psi/ft^m
 C_{hs} = constant, $m/L^{1-2m}t^2$, psi/ft^{2m}
 C_N = constant in equation (E.4), dimensionless
 C_o = Uniaxial Compressive Strength (UCS), m/Lt^2 , psi
 C_r = rock compressibility, $(m/Lt^2)^{-1}$, psi^{-1}
 C_t = total compressibility, $(m/Lt^2)^{-1}$, psi^{-1}
 d_λ = plastic multiplier, dimensionless
 D = elastic stress-strain matrix, m/Lt^2 , psi
 D_{ep} = elastoplastic stress-strain matrix, m/Lt^2 , psi
 D_p = plastic stress-strain matrix, m/Lt^2 , psi
 E = Young modulus, m/Lt^2 , psi
 f = body force per unit volume, $m/(Lt)^2$, psi/ft

- f_x = body force per unit volume along x direction, $m/(Lt)^2$, psi/ft
 f_y = body force per unit volume along y direction, $m/(Lt)^2$, psi/ft
 f_z = body force per unit volume along z direction. $m/(Lt)^2$, psi/ft
 F = failure function, m/Lt^2 , psi
 F_b^e = element load induced by gravity, mL/t^2 , lbf
 F_f^e = element load, mL/t^2 , lbf
 F_s^e = element load induced by surface force, mL/t^2 , lbf
 $F_{\sigma 0}^e$ = element load induced by initial stress, mL/t^2 , lbf
 G = shear modulus, m/Lt^2 , psi
 H = depth to the reference plane, L, ft
 I_1 = first invariant of a stress tensor, m/Lt^2 , psi
 I_1'' = modified first invariant of a stress tensor, m/Lt^2 , psi
 I_3'' = modified third invariant of a stress tensor, $(m/Lt^2)^3$, psi³
 J = Jacobian matrix, L, ft
 J_2 = second invariant of a deviatoric stress tensor, $(m/Lt^2)^2$, psi²
 J_3 = third invariant of a deviatoric stress tensor, $(m/Lt^2)^3$, psi³
 k_x = formation x-direction permeability, L^2 , mD
 k_y = formation y-direction permeability, L^2 , mD
 k_z = formation z-direction permeability, L^2 , mD
 k_D = material constant in Drucker-Prager criterion, m/Lt^2 , psi
 K^e = element stiffness matrix, m/t^2 , psi.ft
 K_k = matrix in equation (D.5), $L^3/t/m$, $ft^2/(psi \cdot Day)$
 K_p^e = conductivity matrix in equation (4.36), $L^4/t/m$, $ft^3/(psi \cdot Day)$
 m = constant, dimensionless
 m_d = gas density exponent in equation (6.3)
 m_H = material constant in Hoek-Brown criterion, dimensionless
 n = constant, dimensionless
 n_n = node number in an element

n_{ip}	= number of Gaussian quadrature points
n_{ipa}	= number of Gaussian quadrature points in a 2D plane
N	= shape function, dimensionless
p	= pore fluid pressure, m/Lt^2 , psi
p_b	= body load, $m.L/t^2$, lbf
p_i	= initial reservoir pressure, m/Lt^2 , psi
\bar{p}	= average reservoir pressure, m/Lt^2 , psi
P_e	= reservoir boundary pressure, m/Lt^2 , psi
P_{wf}	= bottom hole flowing pressure, m/Lt^2 , psi
P_M^e	= matrix in equation (4.36), L^4t^2/m , ft^3/psi
q	= constant, dimensionless
q^e	= element flux inflow/outflow, L^3/t , ft^3/Day
q_f^e	= boundary flux inflow/outflow, L^3/t , ft^3/Day
q_g^e	= gravity induced flux inflow/outflow, L^3/t , ft^3/Day
Q	= plastic potential function, m/Lt^2 , psi
r	= radial coordinate, L, ft
R_e	= reservoir boundary radius, L, ft
R_p	= plastic zone radius, L, ft
R_w	= cavity (wellbore, perforation tunnel or perforation tip) radius, L, ft
s_H	= material constant in Hoek-Brown criterion, dimensionless
S	= area, L^2 , ft^2
S_L	= material constant in modified Lade criterion, m/Lt^2 , psi
S_o	= cohesive strength, m/Lt^2 , psi
t	= time, t, day
T	= surface traction, m/Lt^2 , psi
T_T	= Matrix in equation (D.4), L^{-1} , ft^{-1}
t_0	= initial time, t, day
u	= displacement in x direction, L, ft
u^e	= element nodal displacement, L, ft

v	= displacement in y direction, L, ft
v_f	= flow velocity across a boundary, L/t, ft/Day
V	= element volume, L^3 , ft^3
w	= displacement in z direction, L, ft
w_i	= weight for integration at the i^{th} Gaussian quadrature point, dimensionless
x	= coordinate, L, ft
y	= coordinate, L, ft
z	= coordinate, L, ft

Greek Symbols

α_b	= Biot's constant, dimensionless
α_D	= material constant in Drucker-Prager criterion, dimensionless
γ	= specific gravity of gas, dimensionless
γ_b	= gravity of rock, $m/(Lt)^2$, lbf/ft^3
γ_f	= gravity of pore fluid, $m/(Lt)^2$, lbf/ft^3
γ_{xy}	= shear strain in x-y plain, dimensionless
γ_{xz}	= shear strain in x-z plain, dimensionless
γ_{yz}	= shear strain in y-z plain, dimensionless
Δt	= pseudo-time step in visco-plasticity algorithm, $(m/Lt^2)^{-1}$, psi^{-1}
ε	= strain, dimensionless
ε^e	= elastic strain, dimensionless
ε^p	= plastic strain, dimensionless
ε^{vp}	= visco-plastic strain, dimensionless
ε_r	= radial strain, dimensionless
ε_r^e	= radial elastic strain, dimensionless
ε_r^p	= radial plastic strain, dimensionless
ε_x	= normal strain in x direction, dimensionless
ε_y	= normal strain in y direction, dimensionless

- ε_z = normal strain in z direction, dimensionless
 ε_z^e = vertical elastic strain, dimensionless
 ε_z^p = vertical plastic strain, dimensionless
 ε_θ = tangential strain, dimensionless
 ε_θ^e = tangential elastic strain, dimensionless
 ε_θ^p = tangential plastic strain, dimensionless
 ζ = local coordinate, dimensionless
 η = local coordinate, dimensionless
 η_L = material constant in modified Lade criterion, dimensionless
 θ = angle, dimensionless, radian
 θ_L = Lode's angle, dimensionless, radian
 λ = Lamé's constant, m/Lt², psi
 μ_f = fluid viscosity, m /Lt, cp
 ν = Poisson's ratio, dimensionless, fraction
 ξ = local coordinate, dimensionless
 ρ_f = density of gas, m/L³, lbm/ft³
 σ = total normal stress, m/Lt², psi
 σ' = effective stress, m/Lt², psi
 σ'_0 = initial effective stress, m/Lt², psi
 σ_1 = maximum principal stress, m/Lt², psi
 σ_2 = intermediate principal stress, m/Lt², psi
 σ_3 = minimum principal stress, m/Lt², psi
 σ_h = total minimum horizontal stress, m/Lt², psi
 σ'_h = effective minimum horizontal stress, m/Lt², psi
 σ_H = total maximum horizontal stress, m/Lt², psi
 σ'_H = effective maximum horizontal stress, m/Lt², psi
 σ_p = total radial stress at the interface of plastic and elastic zone, m/Lt², psi

- σ'_p = effective radial stress at the interface of plastic and elastic zone, m/Lt^2 , psi
 σ_r = total radial stress, m/Lt^2 , psi
 σ'_r = effective radial stress, m/Lt^2 , psi
 σ'_v = effective vertical stress, m/Lt^2 , psi
 σ_x = total normal stress in x direction, m/Lt^2 , psi
 σ'_x = effective normal stress in x direction, m/Lt^2 , psi
 σ_y = total normal stress in y direction, m/Lt^2 , psi
 σ_z = total normal stress in z direction, m/Lt^2 , psi
 σ'_z = effective normal stress in z direction, m/Lt^2 , psi
 σ'_θ = effective tangential stress, m/Lt^2 , psi
 τ = shear stress, m/Lt^2 , psi
 τ_{xy} = shear stress in x-y plane, m/Lt^2 , psi
 τ_{xz} = shear stress in x-z plane, m/Lt^2 , psi
 τ_{yz} = shear stress in y-z plane, m/Lt^2 , psi
 ϕ = formation rock porosity, dimensionless, fraction
 ϕ_f = internal friction angle, dimensionless, degrees
 ψ = dilation angle, dimensionless, degree

REFERENCES

1. Terzaghi, K. and Peck, R. B.: *Soil Mechanics in Engineering Practice*, John Wiley and Sons Inc., New York (1948).
2. Hall, C. D., Jr. and Harrisberger, W. H.: "Stability of Sand Arches: A Key to Sand Control," *JPT* (July 1970) 820-829.
3. Stein, N. and Hilchie, D. W.: "Estimating the Maximum Production Rate Possible From Friable Sandstones Without Using Sand Control," *JPT* (September 1972) 1157-1160.
4. Stein, N., Odeh, A.S. and Jones, J.G.: "Estimating Maximum Sand-Free Production Rates From Friable Sands for Different Well Completion Geometries," *JPT* (October 1974) 1156-1158.
5. Tippie, D.B. and Kohlhaas, C.A.: "Effect of Flow Rate on Stability of Unconsolidated Producing Sands," paper SPE 4533 presented at the 48th Annual Fall Meeting of the Society of Petroleum Engineers of AIME held in Las Vegas, Nevada, 30 September - 3 October, 1973.
6. Cleary, M. P., Melvan, J. J. and Kohlhaas, C. A.: "The Effect of Confining Stress and Fluid Properties on Arch Stability in Unconsolidated Sands," paper SPE 8426 presented at the 54th Annual Fall Technical Conference and Exhibition of the Society of Petroleum Engineers of AIME held in Las Vegas, NV, 23-26 September, 1979.
7. Bratli, R. K. and Risnes, R.: "Stability and Failure of Sand Arches," paper SPE 8427 presented at the 54th Annual Fall Technical Conference and Exhibition of the Society of Petroleum Engineers of AIME held in Las Vegas, NV, 23-26 September, 1979.

8. Polillo, A.F., Vassilellis, G.D. and Graves, R. M.: "Simulation of Sand Arching Mechanics Using an Elasto-Plastic Finite Element Formulation," paper SPE 23728 presented at the 2nd Latin American Petroleum Engineering Conference, II LAPEC, of the Society of Petroleum Engineers held in Caracas, Venezuela, 8-11 March, 1992.
9. Yim, K., Dusseault, M. B. and Zhang, L.: "Experimental Study of Sand Production Processes Near an Orifice," paper SPE/ISRM 28068 presented at the SPE/ISRM Rock Mechanics in Petroleum Engineering Conference held in Delft, The Netherlands, 29-31 August, 1994.
10. Bianco, L.C.B. and Halleck, P.M.: "Mechanisms of Arch Instability and Sand Production in Two-Phase Saturated Poorly Consolidated Sand Stones," paper SPE 68932 presented at the SPE European Formation Damage Conference held in The Hague, The Netherlands, 21-22 May, 2001.
11. Antheunis, D., Vriezen, P. B., Schipper, B. A., van der Vlis, A. C.: "Perforation Collapse: Failure of Perforated Friable Sandstones," paper SPE 5750 presented at the SPE-European Spring Meeting of the Society of Petroleum Engineers of AIME held in Amsterdam, The Netherlands, 8-9 April, 1976.
12. Morita, N., Whitfill, D. L., Fedde, O. P., and Levik, T. H.: "Parametric Study of Sand Production Prediction: Analytical Approach," paper SPE 16990 presented at the at the 62nd SPE Annual Technical Conference and Exhibition held in Dallas, TX, 27-30 September, 1987.
13. Morita, N., Whitfill, D. L., Massie, I., and Knudsen, T. W.: "Realistic Sand Production Prediction: Numerical Approach," paper SPE 16989 presented at the 62nd SPE Annual Technical Conference and Exhibition held in Dallas, TX, 27-30 September, 1987.

14. Santarelli, F. J., Ouadfel, H. and Zundel, J.P.: "Optimizing the Completion Procedure to Minimize Sand Production Risk," paper SPE 22797 presented at the 66th Annual Technical Conference and Exhibition of the Society of Petroleum Engineers held in Dallas, TX, 6-9 October, 1991.
15. Tronvoll, J., Morita, N. and Santarelli, F. J.: "Perforation Cavity Stability: Comprehensive Laboratory Experiments and Numerical Analysis," paper SPE 24799 presented at the 67th Annual Technical Conference and Exhibition of the Society of Petroleum Engineers held in Washington, DC, 4-7 October, 1992.
16. Paslay, P. R. and Cheatham, J. B., Jr.: "Rock Stresses Induced by Flow of Fluids into Boreholes, " *SPEJ* (March 1963) 85-94.
17. Geertsma, J.: "Some Rock Mechanics Aspects of Oil and Gas Well Completions," paper SPE 8073 presented at the European Petroleum Conference and Exhibition held in London, U.K., 24-27 October, 1973.
18. Risnes, R. and Bratli, R. K.: "Sand Stress Around a Wellbore," paper SPE 9650 presented at the Middle East Oil Technical Conference of the Society of Petroleum Engineers held in Manama, Bahrain, 9-12 March, 1981.
19. Wang, Z., Peden, J. M. and Damasena, E. S. H.: "The Prediction of Operating Conditions to Constrain Sand Production From a Gas Well," paper SPE 21681 presented at the SPE Production Operations Symposium held in Oklahoma City, OK, 7-9 April, 1991.
20. Bradford, D. R. and Cook, J. M.: "A Semi-analytic Elastoplastic Model for Wellbore Stability with Applications to Sanding," paper SPE/ISRM 28070 presented at the SPE/ISRM Rock Mechanics in Petroleum Engineering Conference held in Delft, The Netherlands, 29-31 August, 1994.

21. Van den Hoek, P. J.: "Horizontal-Wellbore Stability and Sand Production in Weakly Consolidated Sandstones," *SPE Drill. & Completion* (December 2000) 274-283.
22. Valkó, P. and Economides, M.J.: *Hydraulic Fracture Mechanics*, Wiley, Chichester, UK. (1995).
23. Budiningsih, Y., Hareland, G., Boonyapaluk, P. and Guo, B.: "Correct Production Rates Eliminate Sand Production in Directional Wells," paper SPE 29291 presented at the SPE Asia Pacific Oil & Gas Conference held in Kuala Lumpur, Malaysia, 20-22 March, 1995.
24. El-Sayed, A-A. H.: "Maximum Allowable Production Rates From Open Hole Horizontal Wells," paper SPE 21383 presented at the SPE Middle East Oil Show held in Bahrain, 16-19 November, 1991.
25. Abousleiman, Y., Ekbote, S., and Tare, U.: "Time-Dependent Wellbore (In)Stability Predictions : Theory and Case Study," paper IADC/SPE 62796 presented at the 2000 IADC/SPE Asia Pacific Drilling Technology Conference held in Kuala Lumpur, Malaysia, 11-13 September.
26. Abousleiman, Y., Ekbote, S., Cui, L., Mody, F., Roegiers, J. C. *et al.*: "Time-Dependent Coupled Processes in Wellbore Design and Stability: PBORE-3D," paper SPE 56759 presented at the 1999 SPE Annual Technical Conference and Exhibition held in Houston, TX, Oct. 3-6 1999.
27. Vardoulakis, I., Stavropoulou, M. and Papanastasiou, P.: "Hydro-Mechanical Aspects of the Sand Production Problem," *Transport in Porous Media* (1996) **22**, 225.

28. Stavropoulou, M., Papanastasiou, P. and Vardoulakis, I.: "Coupled Wellbore Erosion and Stability Analysis," *Int. J. Numer. Anal. Mech. Geomech.* (1998) **22**, 749.
29. Papamichos, E. and Stavropoulou, M.: "An Erosion-Mechanical Model for Sand Production Rate Prediction," *Int. J. of Rock Mech. & Min. Sci.* (1998) **35**, No. 4-5, 531.
30. Papamichos, E. and Malmanger, E.M.: "A Sand Erosion Model for Volumetric Sand Predictions in a North Sea Reservoir," paper SPE 54007 presented at the 1999 SPE Latin American and Caribbean Petroleum Engineering Conference held in Caracas, Venezuela, 21-23 April.
31. Papamichos, E., Vardoulakis, I., Tronvoll, J. and Skjaerstein, A.: "Volumetric Sand Production Model and Experiment," *Intl. J. Numer. Anal. Meth. Geomech.* (2001) **25**, 789.
32. Coombe, D., Tremblay, B., Tran, D., and Ma, H.: "Coupled Hydro-Geomechanical Modeling of the Cold Production Process," paper SPE 69719 presented at the SPE International Thermal Operations and Heavy Oil Symposium held in Porlamar, Margarita Island, Venezuela, 12-14 March, 2001.
33. Wang, Y.: "Improved Production and Sand (Cold) Production in Conventional and Heavy Oil Reservoirs-A Field Case and Simulation" paper SPE 57290 presented at the 1999 SPE Asia Pacific Improved Oil Recovery Conference held in Kuala Lumpur, Malaysia, 25-28 October.
34. Wang, Y. and Tremblay, B.: "Enhanced Production in Horizontal Wells by the Cavity Failure Well Completion," paper SPE 68835 presented at the SPE Western Regional Meeting held in Bakersfield, CA, 26-30 March, 2001.

35. Wang, Y. and Lu, B.: "A Coupled Reservoir-Geomechanics Model and Applications to Wellbore Stability and Sand Prediction, " paper SPE 69718 presented at the SPE International Thermal Operations and Heavy Oil Symposium held in Porlamar, Margarita Island, Venezuela, 12-14 March, 2001.
36. Vaziri, H. H. and Byrne, P. M.: "Analysis of Stress, Flow and Stability Around Deep Wells," *Géotechnique* (1990) **40**, No. 1, 63.
37. Vaziri, H. H.: "Analytical and Numerical Procedures for Analysis of Flow-Induced Cavitation in Porous Media," *Computers & Structures* (1995) **54**, No. 2, 223.
38. Perkins, T. K. and Weingraten, J. S.: "Stability and Failure of Spherical Cavities in Unconsolidated Sand and Weakly Consolidated Rock," paper SPE 18244 presented at the Annual Technical Conference and Exhibition of the Society of Petroleum Engineers, 2-5 October, 1988.
39. Weingarten, J.S. and Perkins, T.K.: "Prediction of Sand Production in Gas Wells: Method and Gulf of Mexico Case Studies," paper SPE 24797 presented at the 67th Annual Technical Conference and Exhibition of the Society of Petroleum Engineers held in Washington, DC, 4-7 October, 1992.
40. Ong, S., Ramos, R. and Zheng, Z.: "Sand Production Prediction in High Rate, Perforated and Open-Hole Gas Wells," paper SPE 58721 presented at the 2000 SPE International Symposium on Formation Damage Control held in Lafayette, LA, 23-24 February.
41. Da Fontoura, S. A. B. and dos Santos, H. M. R.: "Modeling of the Collapse of Unconsolidated Rock Formations During Production," paper SPE 21092 presented at the SPE Latin American Petroleum Engineering Conference held in Rio de Janeiro, Brazil, 14-19 October, 1990.

42. Wang, Y. and Wu, B.: "Borehole Collapse and Sand Production Evaluation: Experimental Testing, Analytical Solutions and Field Applications," *Proc.*, The 38th U.S. Rock Mechanics Symposium, Washington, DC, 7-10 July (2002), 67-74.
43. Ewy, R. T.: "Wellbore Stability Predictions Using a Modified Lade Criterion," paper SPE 47251 presented at the 1998 SPE/ISRM Eurock'98 held in Trondheim, Norway, 8-10 July.
44. Ewy, R. T., Ray, P., Bovberg, C. A., Norman, P. D., and Goodman, H. E.: "Open Hole Stability and Sanding Predictions by 3D Extrapolation from Hole Collapse Tests," paper SPE 56592 presented at the 1999 SPE Annual Technical Conference and Exhibition held in Houston, TX, 3-6 October.
45. Zhou, S., Hillis, R. R. and Sandiford, M.: "On the Mechanical Stability of Inclined Wellbores," *SPE Drilling & Completion* (June 1996) 67-73.
46. Zhang, J. J. and Rai, C. S.: "Mechanical Strength of Reservoir Materials: Key Information for Sand Prediction," *SPE Reservoir Evaluation & Engineering* (April 2000) 127-131.
47. Awal, M. R., Azeemuddin, M., Khan, M. S., Abdulraheem, A., and Mohiuddin, M. A.: "A More Realistic Sand Production Prediction Using Pore Collapse Theory," *Proc.*, The 38th U.S. Rock Mechanics Symposium, Washington, DC, 7-10 July (2002), 35-42.
48. Abass, H. H., Wilson, J. M., Venditto, J. J., and Voss, R. E.: "Stimulating Weak Formations Using New Hydraulic Fracturing and Sand Control Approaches," paper SPE 25494 presented at the Production Operations Symposium, Oklahoma City, OK, 21-23 March, 1993.
49. Chen, W. and Mizuno, E.: *Nonlinear Analysis in Soil Mechanics – Theory and Implementation*, Elsevier, London (1990).

50. Sanfilippo, F., Ripa, G., Brignoli, M., and Santarelli, F. J.: "Economical Management of Sand Production by a Methodology Validated on an Extensive Database of Field Data," paper SPE 30472 presented at the SPE Annual Technical Conference and Exhibition held in Dallas, TX, 22-25 October, 1995.
51. Biot, M.: "General Theory of Three-Dimensional Consolidation," *Journal of Applied Physics* (1941) **12**, 155.
52. Aziz, K. and Settari, A.: *Petroleum Reservoir Simulation*, Applied Science Publishers Ltd., London (1979).
53. Smith, I. M. and Griffiths, D. V.: *Programming the Finite Element Method*, John Wiley & Sons, New York (1998).
54. Zienkiewicz, O. C., Valliappan, S. and King, I. P. : "Elasto-plastic Solutions of Engineering Problems, 'Initial-Stress' Finite Element Approach, " *Int. J. Num. Meth. Eng.* (1969) **1**, 75.
55. Zienkiewicz, O. C. and Corneau, I. C.: "Viscoplasticity, Plasticity and Creep in Elastic Solids, A Unified Numerical Solution Approach, " *Int. J. Num. Meth. Eng.* (1974) **8**, 821.
56. McLean, M. and Addis, M.: "Wellbore Stability: The Effect of Strength Criteria on Mud Weight Recommendations", paper SPE 20405 presented at the 1990 SPE Annual Technical Conference and Exhibition, New Orleans, LA, 23-26 September.
57. Hoek, E. and Brown, E.: *Underground Excavations in Rock*, The Institution of Mining and Metallurgy, London (1980).
58. Drucker, D. and Prager, W.: "Soil Mechancis and Plastic Analysis or Limit Design", *Q. Appl. Math.* (1952) **10**, 157.

59. Lade, P.: "Elasto-plastic Stress-strain Theory for Cohesionless Soil with Curved Yield Surfaces", *International Journal of Solids and Structures*, (1977) **13**, 1014.
60. Colmenares, L. and Zoback, M.: "Statistical Evaluation of Six Rock Failure Criteria Constrained by Ployaxial Test Data," *Proc.*, The 38th U.S. Rock Mechanics Symposium, Washington, DC, 7-10 July (2002), 1251-1258.
61. Colmenares, L. and Zoback, M.: "A Statistical Evaluation of Intact Rock Failure Criteria Constrained by Ployaxial Test Data for Five Different Rocks," *International Journal of Rock Mechanics & Mining Science* (2002) **39**, 695.
62. Marsala, A. F., Ragazzini, G., Meazza, O., Brignoli, M., and Santarelli, F. J.: "Basin Scale Rock Mechanics: logs and core measurements," paper SPE/ISRM 28034 presented at the SPE/ISRM Rock Mechanics in Petroleum Engineering Conference held in Delft, The Netherlands, 29-31 August, 1994.
63. Moricca, G., Ripa, G., Sanfilippo, F., and Santarelli, F. J.: "Basin Scale Rock Mechanics: Field Observations of Sand Production," paper SPE/ISRM 28066 presented at the SPE/ISRM Rock Mechanics in Petroleum Engineering Conference held in Delft, The Netherlands, 29-31 August, 1994.
64. Tronvoll, J., Papamichos, E., Skjaerstein, A., and Sanfilippo, F.: "Sand Production in Ultra-Weak Sandstones: Is Sand Control Absolutely Necessary?," paper SPE 39042 presented at the 5th Latin American and Caribbean Petroleum Engineering Conference and Exhibition held in Rio de Janeiro, Brazil, August 30-Sept. 3, 1997.
65. Kanj, M. Y. and Abousleiman, Y.: "Realistic Sanding Predictions: A Neural Approach," paper SPE 56631 presented at the SPE Annual Technical Conference and Exhibition held in Houston, TX, 3-6 October, 1999.

APPENDIX A

DERIVATION OF POROELASTOPLASTIC SOLUTION FOR THICK-WALLED HOLLOW CYLINDER-ISOTROPIC IN-SITU STRESS CASE

A.1 Poroelastic solution

Poroelastic solution is obtained by employing the momentum equilibrium equation, Hook's law and corresponding boundary conditions.

The equilibrium equation for axisymmetrical hollow-cylinder under plane strain condition is

$$\frac{\partial \sigma'_r}{\partial r} + \frac{\sigma'_r - \sigma'_\theta}{r} + \alpha_b \frac{\partial p(r, t)}{\partial r} = 0 \quad (\text{A.1})$$

where

$$\sigma'_j = \sigma_j - \alpha_b p(r, t) \quad j = r, \theta, z \quad (\text{A.2})$$

Stress-strain relation is

$$\begin{bmatrix} \sigma'_r - \sigma'_h(t_0) \\ \sigma'_\theta - \sigma'_h(t_0) \\ \sigma'_z - \sigma'_v(t_0) \end{bmatrix} = \begin{bmatrix} \lambda + 2G & \lambda & \lambda \\ \lambda & \lambda + 2G & \lambda \\ \lambda & \lambda & \lambda + 2G \end{bmatrix} \begin{bmatrix} \varepsilon_r^e \\ \varepsilon_\theta^e \\ \varepsilon_z^e \end{bmatrix} \quad (\text{A.3})$$

The relations between λ , G and Young's modulus, E , and Poisson's ratio ν are respectively

$$\lambda = \frac{E\nu}{(1+\nu)(1-2\nu)} \quad (\text{A.4})$$

$$G = \frac{E}{2(1+\nu)} \quad (\text{A.5})$$

Strain-displacement relation is

$$\begin{bmatrix} \varepsilon_r \\ \varepsilon_\theta \\ \varepsilon_z \end{bmatrix} = \begin{bmatrix} \frac{du}{dr} \\ \frac{u}{r} \\ 0 \end{bmatrix} \quad (\text{A.6})$$

The boundary conditions are

$$\sigma'_r \Big|_{r=R_e} = \sigma_h(t) - \alpha_b p(R_e, t) \quad (\text{A.7})$$

and

$$\sigma'_r \Big|_{r=R_w} = (1 - \alpha_b) P_{wf}(t) \quad (\text{A.8})$$

Using the above relations, we obtain the poroelastic solution.

The stress solution is

$$\sigma'_r = (\lambda + G)A_e - 2G \frac{B_e}{r^2} + \frac{\alpha_b}{r^2} \frac{2G}{\lambda + 2G} \int_{R_w}^r p(r, t) r dr - \alpha_b p(r, t) + \sigma'_h(t_0) \quad (\text{A.9})$$

$$\sigma'_\theta = (\lambda + G)A_e + 2G \frac{B_e}{r^2} - \frac{\alpha_b}{r^2} \frac{2G}{\lambda + 2G} \int_{R_w}^r p(r, t) r dr - \alpha_b \frac{\lambda}{\lambda + 2G} p(r, t) + \sigma'_h(t_0) \quad (\text{A.10})$$

$$\sigma'_z = \lambda A_e - \alpha_b \frac{\lambda}{\lambda + 2G} p(r, t) + \sigma'_v(t_0) \quad (\text{A.11})$$

where A_e and B_e are integration constants, which are

$$A_e = \frac{1}{\lambda + G} \frac{(P_{wf}(t) - \sigma_h'(t_0))R_w^2 - (\sigma_h(t) - \sigma_h'(t_0))R_e^2}{R_w^2 - R_e^2} + \alpha_b \frac{2G}{(\lambda + 2G)(\lambda + G)} \frac{\int_{R_w}^{R_e} p(r, t) r dr}{R_w^2 - R_e^2} \quad (A.12)$$

$$B_e = \alpha_b \frac{1}{\lambda + 2G} \frac{R_w^2}{R_w^2 - R_e^2} \int_{R_w}^{R_e} p(r, t) r dr - \frac{1}{2G} \frac{R_w^2 R_e^2}{R_w^2 - R_e^2} (\sigma_h(t) - P_{wf}(t)) \quad (A.13)$$

The displacement solution is

$$u = \frac{A_e}{2} r + \frac{B_e}{r} - \frac{\alpha_b}{r(\lambda + 2G)} \int_{R_w}^r p(r, t) r dr \quad (A.14)$$

The strain solution is

$$\varepsilon_r^e = \frac{A_e}{2} - \frac{B_e}{r^2} + \frac{\alpha_b}{r^2(\lambda + 2G)} \int_{R_w}^r p(r, t) r dr - \frac{\alpha_b}{\lambda + 2G} p(r, t) \quad (A.15)$$

$$\varepsilon_\theta^e = \frac{A_e}{2} + \frac{B_e}{r^2} - \frac{\alpha_b}{r^2(\lambda + 2G)} \int_{R_w}^r p(r, t) r dr \quad (A.16)$$

A.2 Poroelastoplastic solution

A.2.1 Mohr-Coulomb failure criterion

The Mohr-Coulomb failure criterion can be written as in the following equation and shown in **Fig. A.1**.

$$\tau = S_o + \sigma \tan \phi_f \quad (A.17)$$

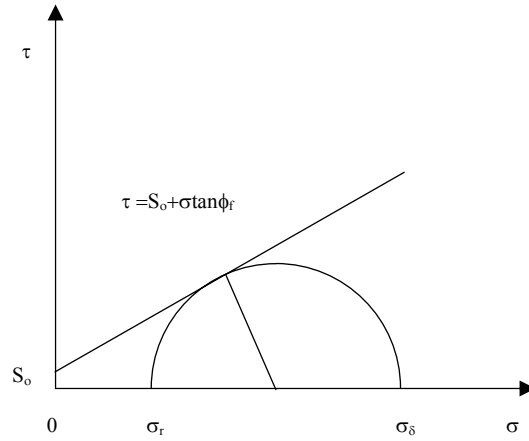


Figure A.1 Mohr-Coulomb criterion

For a producing well, we assume σ'_θ is the maximum principal stress and σ'_r is the minimum principal stress. From **Fig. A.1**, we see when the failure envelope touches the Mohr circle,

$$\frac{\sigma'_\theta - \sigma'_r}{2} = \frac{\sigma'_\theta + \sigma'_r}{2} \sin \phi_f + S_0 \cos \phi_f \quad (\text{A.18})$$

By rearranging, yield

$$\sigma'_r - \sigma'_\theta = -\frac{2 \sin \phi_f}{1 - \sin \phi_f} (\sigma'_r + S_0 \cot \phi_f) \quad (\text{A.19})$$

The above two equations indicate that failure occurs if

$$F = (1 + \sin \phi_f) \sigma'_r + \sigma'_\theta (\sin \phi_f - 1) + 2S_0 \cos \phi_f = 0 \quad (\text{A.20})$$

The flow rule associated with the above yield function is

$$d\varepsilon_j^p = d\lambda \frac{dF}{d\sigma_j} \quad (j = r, \theta, z) \quad (\text{A.21})$$

Written in matrix form, the flow rule is

$$\begin{bmatrix} d\epsilon_r^p \\ d\epsilon_\theta^p \\ d\epsilon_z^p \end{bmatrix} = d_\lambda \begin{bmatrix} 1 + \sin\phi_f \\ \sin\phi_f - 1 \\ 0 \end{bmatrix} \quad (\text{A.22})$$

where d_λ is a scalar multiplier

The flow rule can also be non-associated with the failure function if we take the failure potential function Q to be

$$Q = (1 + \sin\psi)\sigma'_r + \sigma'_\theta (\sin\psi - 1) + 2S_o \cos\psi \quad (\text{A.23})$$

where ψ is dilation angle.

The flow rule is therefore

$$\begin{bmatrix} d\epsilon_r^p \\ d\epsilon_\theta^p \\ d\epsilon_z^p \end{bmatrix} = d\lambda \begin{bmatrix} 1 + \sin\psi \\ \sin\psi - 1 \\ 0 \end{bmatrix} \quad (\text{A.24})$$

Here in this appendix, we assume the non-associated flow rule. If one wants to use the associated flow rule, just set $\psi = \phi_f$.

A.2.2 Stress solution in the plastic region

In the plastic region, both the Mohr-Coulomb failure criterion and the equilibrium equation are satisfied. Combining equations (A.1) and (A.19), using the following boundary conditions

$$\sigma'_r \Big|_{r=R_p} = \sigma'_p \quad (\text{A.25})$$

$$\sigma'_r \Big|_{r=R_w} = (1 - \alpha_b)P_{wf}(t) \quad (\text{A.26})$$

The stress solution in the plastic region is

$$\sigma'_r = -\alpha_b r^m \int_{R_w}^r \frac{\partial p(r,t)}{\partial r} r^{-m} dr + C_{hc} r^m - S_o \cot \phi_f \quad (\text{A.27})$$

$$\sigma'_\theta = -\alpha_b q r^m \int_{R_w}^r \frac{\partial p(r,t)}{\partial r} r^{-m} dr + C_{hc} q r^m - S_o \cot \phi_f \quad (\text{A.28})$$

$$\sigma'_z = \frac{\lambda}{\lambda + G} \left[-\alpha_b \frac{1+q}{2} r^m \int_{R_w}^r \frac{\partial p(r,t)}{\partial r} r^{-m} dr + C_{hc} \frac{1+q}{2} r^m - S_o \cot \phi_f - \sigma'_h(t_0) \right] + \sigma'_v(t_0) \quad (\text{A.29})$$

where

$$m = \frac{2 \sin \phi_f}{1 - \sin \phi_f} \quad (\text{A.30})$$

$$q = \frac{1 + \sin \phi_f}{1 - \sin \phi_f} \quad (\text{A.31})$$

In equations (A.27)-(A.29), C_{hc} is integration constant which is determined by the inner boundary condition (A.26), which results in

$$C_{hc} = \frac{S_o \cot \phi_f + (1 - \alpha_b) P_{wf}(t)}{R_w^m} \quad (\text{A.32})$$

A.2.3 Strain solution in the plastic region

A.2.3.1 Elastic strain solution

In the plastic region, the elastic strain and stress still satisfy the Hook's law, equation (A.3). Using the stresses derived in equations (A.27)-(A.29), the elastic strain is solved.

$$\begin{aligned} \varepsilon_r^e = & \alpha_b \left(\frac{\lambda}{4G(\lambda+G)} q - \frac{\lambda+2G}{4G(\lambda+G)} \right) r^m \int_{R_w}^r \frac{\partial p(r,t)}{\partial r} r^{-m} dr + C_{hc} \left(\frac{\lambda+2G}{4G(\lambda+G)} q - \frac{\lambda}{4G(\lambda+G)} \right) r^m \\ & - \frac{S_o \cot \phi_f + \sigma'_h(t_0)}{2(\lambda+G)} \end{aligned} \quad (A.33)$$

$$\begin{aligned} \varepsilon_\theta^e = & \alpha_b \left(\frac{\lambda}{4G(\lambda+G)} - \frac{\lambda+2G}{4G(\lambda+G)} q \right) r^m \int_{R_w}^r \frac{\partial p(r,t)}{\partial r} r^{-m} dr + C_{hc} \left(\frac{\lambda+2G}{4G(\lambda+G)} q - \frac{\lambda}{4G(\lambda+G)} \right) r^m \\ & - \frac{S_o \cot \phi_f + \sigma'_h(t_0)}{2(\lambda+G)} \end{aligned} \quad (A.34)$$

A.2.3.2 Plastic strain solution

From the flow rule, equation (A.24), we notice that

$$d\varepsilon_r^p + n d\varepsilon_\theta^p = 0 \quad (A.35)$$

$$d\varepsilon_z^p = 0 \quad (A.36)$$

where

$$n = \frac{1 + \sin \psi}{1 - \sin \psi} \quad (A.37)$$

Integrating the equations results in

$$\varepsilon_r^p + n \varepsilon_\theta^p = 0 \quad (A.38)$$

$$\varepsilon_z^p = 0 \quad (A.39)$$

The compatibility equation is

$$r \frac{\partial \varepsilon_\theta}{\partial r} + \varepsilon_\theta - \varepsilon_r = 0 \quad (\text{A.40})$$

Since

$$\varepsilon_r = \varepsilon_r^e + \varepsilon_r^p, \quad \varepsilon_\theta = \varepsilon_\theta^e + \varepsilon_\theta^p, \quad \varepsilon_z = \varepsilon_z^e + \varepsilon_z^p = 0 \quad (\text{A.41})$$

Substituting the corresponding items in (A.41) to (A.40) and using (A.38), yields

$$r \frac{\partial \varepsilon_\theta^p}{\partial r} + (n+1)\varepsilon_\theta^p = \varepsilon_r^e - \varepsilon_\theta^e - r \frac{\partial \varepsilon_\theta^e}{\partial r} \quad (\text{A.42})$$

The right hand side of equation (A.42) is evaluated through equations (A.33) and (A.34). The boundary condition associated with equation (A.42) is

$$\varepsilon_\theta^p \Big|_{r=R_p} = 0 \quad (\text{A.43})$$

The solution is then

$$\varepsilon_\theta^p = r^{-(n+1)} \left[\alpha_b C_1 \int_{R_w}^r \left[r^{m+n} \int_{R_w}^r \frac{\partial p(r,t)}{\partial r} r^{-m} dr \right] dr + \alpha_b C_2 \int_{R_w}^r \frac{\partial p(r,t)}{\partial r} r^{n+1} dr + C_3 \frac{r^{m+n+1}}{m+n+1} + C_4 \right] \quad (\text{A.44})$$

where

$$C_1 = \frac{1}{2G} (q-1) - m \left(\frac{\lambda}{4G(\lambda+G)} - \frac{\lambda+2G}{4G(\lambda+G)} q \right) \quad (\text{A.45})$$

$$C_2 = \frac{\lambda+2G}{4G(\lambda+G)} q - \frac{\lambda}{4G(\lambda+G)} \quad (\text{A.46})$$

$$C_3 = \frac{C_{hc}}{2G} (1-q) - C_{hc} m \left(\frac{\lambda+2G}{4G(\lambda+G)} q - \frac{\lambda}{4G(\lambda+G)} \right) \quad (\text{A.47})$$

$$C_4 = -\alpha_b C_1 \int_{R_w}^{R_p} \left[r^{m+n} \int_{R_w}^r \frac{\partial p(r, t)}{\partial r} r^{-m} dr \right] dr - \alpha_b C_2 \int_{R_w}^{R_p} \frac{\partial p(r, t)}{\partial r} r^{n+1} dr - C_3 \frac{R_p^{m+n+1}}{m+n+1}$$
(A.48)

From equation (A.38), we solve for ε_r^p

$$\varepsilon_r^p = -n\varepsilon_\theta^p$$
(A.49)

which results in

$$\varepsilon_r^p = -nr^{-(n+1)} \left[\alpha_b C_1 \int_{R_w}^r \left[r^{m+n} \int_{R_w}^r \frac{\partial p(r, t)}{\partial r} r^{-m} dr \right] dr + \alpha_b C_2 \int_{R_w}^r \frac{\partial p(r, t)}{\partial r} r^{n+1} dr + C_3 \frac{r^{m+n+1}}{m+n+1} + C_4 \right]$$
(A.50)

A.2.4 Displacement solution in the plastic region

Since

$$\varepsilon_\theta = \varepsilon_\theta^e + \varepsilon_\theta^p = \frac{u}{r}$$
(A.51)

Substituting equations (A.34) and (A.44) into (A.51), yields the displacement,

$$u = -\alpha \left(\frac{\lambda + 2G}{4G(\lambda + G)} q - \frac{\lambda}{4G(\lambda + G)} \right) r^{m+1} \int_{R_w}^r \frac{\partial p(r, t)}{\partial r} r^{-m} dr + C_{hc} \left(\frac{\lambda + 2G}{4G(\lambda + G)} q - \frac{\lambda}{4G(\lambda + G)} \right) r^{m+1} - \frac{S_o \cot \phi + \sigma'_h(t_0)}{2(\lambda + G)} r + r^{-n} \left[\alpha C_1 \int_{R_w}^r \left(r^{m+n} \int_{R_w}^r \frac{\partial p(r, t)}{\partial r} r^{-m} dr \right) dr + \alpha C_2 \int_{R_w}^r \frac{\partial p(r, t)}{\partial r} r^{n+1} dr + C_3 \frac{r^{m+n+1}}{m+n+1} + C_4 \right]$$
(A.52)

A.2.5 Stress, strain and displacement solutions in elastic region

Compared with the linear elastic solution, equations (A.9)-(A.16), the elastic solution is derived by changing the inner boundary condition to

$$\sigma'_r \Big|_{r=R_p} = \sigma'_p \quad (\text{A.53})$$

The solutions are

$$\sigma'_r = (\lambda + G)A_{ep} - 2G \frac{B_{ep}}{r^2} + \frac{\alpha_b}{r^2} \frac{2G}{\lambda + 2G} \int_{R_p}^r p(r, t) r dr - \alpha_b p(r, t) + \sigma'_h(t_0) \quad (\text{A.54})$$

$$\sigma'_\theta = (\lambda + G)A_{ep} + 2G \frac{B_{ep}}{r^2} - \frac{\alpha_b}{r^2} \frac{2G}{\lambda + 2G} \int_{R_p}^r p(r, t) r dr - \alpha_b \frac{\lambda}{\lambda + 2G} p(r, t) + \sigma'_h(t_0) \quad (\text{A.55})$$

$$\sigma'_z = \lambda A_{ep} - \alpha_b \frac{\lambda}{\lambda + 2G} p(r, t) + \sigma'_v(t_0) \quad (\text{A.56})$$

where A_{ep} and B_{ep} are integration constants, which are

$$A_{ep} = \frac{1}{\lambda + G} \frac{(\sigma_p - \sigma_h(t_0))R_p^2 - (\sigma_h(t) - \sigma_h(t_0))R_e^2}{R_p^2 - R_e^2} + \alpha_b \frac{2G}{(\lambda + 2G)(\lambda + G)} \frac{\int_{R_p}^{R_e} p(r, t) r dr}{R_p^2 - R_e^2} \quad (\text{A.57})$$

$$B_{ep} = \alpha_b \frac{1}{\lambda + 2G} \frac{R_p^2}{R_p^2 - R_e^2} \int_{R_p}^{R_e} p(r, t) r dr - \frac{1}{2G} \frac{R_p^2 R_e^2}{R_p^2 - R_e^2} (\sigma_h(t) - \sigma_p) \quad (\text{A.58})$$

The displacement solution is

$$u = \frac{A_{ep}}{2} r + \frac{B_{ep}}{r} - \frac{\alpha_b}{r(\lambda + 2G)} \int_{R_p}^r p(r, t) r dr \quad (\text{A.59})$$

The strain solution is

$$\varepsilon_r^e = \frac{A_{ep}}{2} - \frac{B_{ep}}{r^2} + \frac{\alpha_b}{r^2(\lambda + 2G)} \int_{R_p}^r p(r, t) r dr - \frac{\alpha_b}{\lambda + 2G} P(r, t) \quad (A.60)$$

$$\varepsilon_\theta^e = \frac{A_{ep}}{2} + \frac{B_{ep}}{r^2} - \frac{\alpha_b}{r^2(\lambda + 2G)} \int_{R_p}^r p(r, t) r dr \quad (A.61)$$

A.2.6 Plastic region radius R_p and the radial stress at the boundary of elastic and plastic region

The radial stress at the plastic and elastic region boundary must be equal to each other. Therefore, from equation (A.27)

$$\sigma'_p = \sigma_p - \alpha P(R_p, t) = -\alpha R_p^m \int_{R_w}^{R_p} \frac{\partial p(r, t)}{\partial r} r^{-m} dr + C_{hc} R_p^m - S_o \cot \phi \quad (A.62)$$

The tangential stress must also be equal to each other. By equating (A.28) and (A.55), yield

$$\begin{aligned} & -\alpha_b q R_p^m \int_{R_w}^{R_p} \frac{\partial p(r, t)}{\partial r} r^{-m} dr + C_{hc} q R_p^m - C_o \cot \phi_f \\ & = (\lambda + G) A_{ep} + 2G \frac{B_{ep}}{R_p^2} - \alpha_b \frac{\lambda}{\lambda + 2G} p(R_p, t) + \sigma'_h(t_0) \end{aligned} \quad (A.63)$$

APPDENDIX B

DERIVATION OF POROELASTIC SOLUTION FOR THICK-WALLED HOLLOW CYLINDER-ANISOTROPIC IN-SITU STRESS CASE

If the external stresses around a borehole/perforation tunnel are anisotropic, the Kirsch solution²² provides the stresses around such cavity, which is

$$\sigma_r = \frac{\sigma_H(t) + \sigma_h(t)}{2} \left(1 - \frac{R_w^2}{r^2}\right) + \frac{\sigma_H(t) - \sigma_h(t)}{2} \left(1 - 4\frac{R_w^2}{r^2} + 3\frac{R_w^4}{r^4}\right) \cos(2\theta) \quad (\text{B.1})$$

$$\sigma_\theta = \frac{\sigma_H(t) + \sigma_h(t)}{2} \left(1 + \frac{R_w^2}{r^2}\right) - \frac{\sigma_H(t) - \sigma_h(t)}{2} \left(1 + 3\frac{R_w^4}{r^4}\right) \cos(2\theta) \quad (\text{B.2})$$

$$\tau_{r\theta} = -\frac{\sigma_H(t) - \sigma_h(t)}{2} \left(1 + 2\frac{R_w^2}{r^2} - 3\frac{R_w^4}{r^4}\right) \sin(2\theta) \quad (\text{B.3})$$

If there is presence of fluid flow, by using the solution derived in **Appendix A**, we know that the fluid flow induced stress is

$$\sigma'_r = (\lambda + G)A_e - 2G \frac{B_e}{r^2} - \alpha_b p(r, t) \quad (\text{B.4})$$

$$\sigma'_\theta = (\lambda + G)A_e + 2G \frac{B_e}{r^2} - \alpha_b \frac{\lambda}{\lambda + 2G} p(r, t) \quad (\text{B.5})$$

If linear elasticity is assumed, the superposition concept applies. The cumulative stress is the summation of stresses caused by in-situ stresses and fluid flow, therefore

$$\begin{aligned} \sigma'_r = & (\lambda + G)A_e - 2G \frac{B_e}{r^2} + \frac{\alpha_b}{r^2} \frac{2G}{\lambda + 2G} \int_{R_w}^r p(r, t) r dr - \alpha_b p(r, t) \\ & + \frac{\sigma_H(t) + \sigma_h(t)}{2} \left(1 - \frac{R_w^2}{r^2}\right) + \frac{\sigma_H(t) - \sigma_h(t)}{2} \left(1 - 4\frac{R_w^2}{r^2} + 3\frac{R_w^4}{r^4}\right) \cos(2\theta) \end{aligned} \quad (\text{B.6})$$

$$\begin{aligned} \sigma'_\theta = & (\lambda + G)A_e + 2G \frac{B_e}{r^2} - \frac{\alpha_b}{r^2} \frac{2G}{\lambda + 2G} \int_{R_w}^r p(r, t) r dr - \alpha_b \frac{\lambda}{\lambda + 2G} p(r, t) \\ & + \frac{\sigma_H(t) + \sigma_h(t)}{2} \left(1 + \frac{R_w^2}{r^2}\right) - \frac{\sigma_H(t) - \sigma_h(t)}{2} \left(1 + 3 \frac{R_w^4}{r^4}\right) \cos(2\theta) \end{aligned} \quad (B.7)$$

$$\tau_{r\theta} = -\frac{\sigma_H(t) - \sigma_h(t)}{2} \left(1 + 2 \frac{R_w^2}{r^2} - 3 \frac{R_w^4}{r^4}\right) \sin(2\theta) \quad (B.8)$$

where

$$A_e = \frac{1}{\lambda + G} \frac{P_{wf}(t) R_w^2}{R_w^2 - R_e^2} + \alpha_b \frac{2G}{(\lambda + 2G)(\lambda + G)} \frac{\int_{R_w}^{R_e} p(r, t) r dr}{R_w^2 - R_e^2} \quad (B.9)$$

$$B_e = \alpha_b \frac{1}{\lambda + 2G} \frac{R_w^2}{R_w^2 - R_e^2} \int_{R_w}^{R_e} p(r, t) r dr + \frac{1}{2G} \frac{R_w^2 R_e^2}{R_w^2 - R_e^2} P_{wf}(t) \quad (B.10)$$

APPENDIX C

FINITE ELEMENT FORMULATION OF 3D STRESS MODEL

C.1 Element stiffness matrix⁵³

$$\mathbf{K}^e = \iiint_{\Omega_e} \mathbf{B}^T \mathbf{D} \mathbf{B} \, dx dy dz \quad (\text{C.1})$$

where

$$\mathbf{B} = \begin{bmatrix} \frac{\partial}{\partial x} & 0 & 0 \\ 0 & \frac{\partial}{\partial y} & 0 \\ 0 & 0 & \frac{\partial}{\partial z} \\ \frac{\partial}{\partial y} & \frac{\partial}{\partial x} & 0 \\ 0 & \frac{\partial}{\partial z} & \frac{\partial}{\partial y} \\ \frac{\partial}{\partial z} & 0 & \frac{\partial}{\partial x} \end{bmatrix} \begin{bmatrix} N_1 & 0 & 0 & \dots & \dots & N_{nn} & 0 & 0 \\ 0 & N_1 & 0 & \dots & \dots & 0 & N_{nn} & 0 \\ 0 & 0 & N_1 & \dots & \dots & 0 & 0 & N_{nn} \end{bmatrix}$$

$$= \begin{bmatrix} \frac{\partial N_1}{\partial x} & 0 & 0 & \dots & \dots & \frac{\partial N_{nn}}{\partial x} & 0 & 0 \\ 0 & \frac{\partial N_1}{\partial y} & 0 & \dots & \dots & 0 & \frac{\partial N_{nn}}{\partial y} & 0 \\ 0 & 0 & \frac{\partial N_1}{\partial z} & \dots & \dots & 0 & 0 & \frac{\partial N_{nn}}{\partial z} \\ \frac{\partial N_1}{\partial y} & \frac{\partial N_1}{\partial x} & 0 & \dots & \dots & \frac{\partial N_{nn}}{\partial y} & \frac{\partial N_{nn}}{\partial x} & 0 \\ 0 & \frac{\partial N_1}{\partial z} & \frac{\partial N_1}{\partial y} & \dots & \dots & 0 & \frac{\partial N_{nn}}{\partial z} & \frac{\partial N_{nn}}{\partial y} \\ \frac{\partial N_1}{\partial z} & 0 & \frac{\partial N_1}{\partial x} & \dots & \dots & \frac{\partial N_{nn}}{\partial z} & 0 & \frac{\partial N_{nn}}{\partial x} \end{bmatrix} \quad (\text{C.2})$$

where N is a function of local coordinates (ξ, η, ζ) and therefore the above derivatives need to be calculated indirectly.

$$\begin{bmatrix} \frac{\partial N_1}{\partial x} & \frac{\partial N_2}{\partial x} & \dots & \dots & \frac{\partial N_{n-1}}{\partial x} & \frac{\partial N_n}{\partial x} \\ \frac{\partial N_1}{\partial y} & \frac{\partial N_2}{\partial y} & \dots & \dots & \frac{\partial N_{n-1}}{\partial y} & \frac{\partial N_n}{\partial y} \\ \frac{\partial N_1}{\partial z} & \frac{\partial N_2}{\partial z} & \dots & \dots & \frac{\partial N_{n-1}}{\partial z} & \frac{\partial N_n}{\partial z} \end{bmatrix} = \mathbf{J}^{-1} \begin{bmatrix} \frac{\partial N_1}{\partial \xi} & \frac{\partial N_2}{\partial \xi} & \dots & \dots & \frac{\partial N_{n-1}}{\partial \xi} & \frac{\partial N_n}{\partial \xi} \\ \frac{\partial N_1}{\partial \eta} & \frac{\partial N_2}{\partial \eta} & \dots & \dots & \frac{\partial N_{n-1}}{\partial \eta} & \frac{\partial N_n}{\partial \eta} \\ \frac{\partial N_1}{\partial \zeta} & \frac{\partial N_2}{\partial \zeta} & \dots & \dots & \frac{\partial N_{n-1}}{\partial \zeta} & \frac{\partial N_n}{\partial \zeta} \end{bmatrix} \quad (\text{C.3})$$

The Jacobian matrix \mathbf{J} is

$$\mathbf{J} = \begin{bmatrix} \frac{\partial x}{\partial \xi} & \frac{\partial y}{\partial \xi} & \frac{\partial z}{\partial \xi} \\ \frac{\partial x}{\partial \eta} & \frac{\partial y}{\partial \eta} & \frac{\partial z}{\partial \eta} \\ \frac{\partial x}{\partial \zeta} & \frac{\partial y}{\partial \zeta} & \frac{\partial z}{\partial \zeta} \end{bmatrix} = \begin{bmatrix} \frac{\partial N_1}{\partial \xi} & \frac{\partial N_2}{\partial \xi} & \dots & \dots & \frac{\partial N_{n-1}}{\partial \xi} & \frac{\partial N_n}{\partial \xi} \\ \frac{\partial N_1}{\partial \eta} & \frac{\partial N_2}{\partial \eta} & \dots & \dots & \frac{\partial N_{n-1}}{\partial \eta} & \frac{\partial N_n}{\partial \eta} \\ \frac{\partial N_1}{\partial \zeta} & \frac{\partial N_2}{\partial \zeta} & \dots & \dots & \frac{\partial N_{n-1}}{\partial \zeta} & \frac{\partial N_n}{\partial \zeta} \end{bmatrix} \begin{bmatrix} x_1 & y_1 & z_1 \\ x_2 & y_2 & z_2 \\ \vdots & \vdots & \vdots \\ \vdots & \vdots & \vdots \\ x_{n-1} & y_{n-1} & z_{n-1} \\ x_n & y_n & z_n \end{bmatrix} \quad (\text{C.4})$$

The element stiffness matrix obtained from the above transformation is very complex and is generally integrated through the Gaussian quadrature

$$\mathbf{K}^e = \int_{-1}^1 \int_{-1}^1 \int_{-1}^1 \mathbf{B}^T \mathbf{D} \mathbf{B} |\mathbf{J}| d\xi d\eta d\zeta = \sum_{i=1}^{n_{ip}} [\mathbf{B}^T \mathbf{D} \mathbf{B} |\mathbf{J}|]_i w_i \quad (\text{C.5})$$

C.2 Element nodal force

If both surface force and body force are considered

$$\mathbf{F}_f^e = \iiint_{\Omega_e} \mathbf{N}^T \mathbf{f} dx dy dz + \iint_S \mathbf{N}^T \mathbf{T} dS - \iiint_{\Omega_e} \mathbf{B}^T \boldsymbol{\sigma}_0' dx dy dz \quad (\text{C.6})$$

where

$$\mathbf{f} = \begin{bmatrix} \alpha_b \frac{\partial p}{\partial x} \\ \alpha_b \frac{\partial p}{\partial y} \\ -\gamma_b + \alpha_b \frac{\partial p}{\partial z} \end{bmatrix} \quad (\text{C.7})$$

$$\mathbf{N} = \begin{bmatrix} N_1 & 0 & 0 & \cdots & \cdots & N_{n_n} & 0 & 0 \\ 0 & N_1 & 0 & \cdots & \cdots & 0 & N_{n_n} & 0 \\ 0 & 0 & N_1 & \cdots & \cdots & 0 & 0 & N_{n_n} \end{bmatrix} \quad (\text{C.8})$$

C.2.1 Body force

$$\mathbf{F}_b^e = \iiint_{\Omega_e} \mathbf{N}^T \mathbf{f} dx dy dz \quad (\text{C.9})$$

$$\begin{aligned} \mathbf{F}_b^e &= \int_{-1}^1 \int_{-1}^1 \int_{-1}^1 \begin{bmatrix} N_1 & 0 & 0 \\ 0 & N_1 & 0 \\ 0 & 0 & N_1 \\ \vdots & \vdots & \vdots \\ \vdots & \vdots & \vdots \\ N_{n_n} & 0 & 0 \\ 0 & N_{n_n} & 0 \\ 0 & 0 & N_{n_n} \end{bmatrix} \begin{bmatrix} \alpha_b \frac{\partial p}{\partial x} \\ \alpha_b \frac{\partial p}{\partial y} \\ -\gamma_b + \alpha_b \frac{\partial p}{\partial z} \end{bmatrix} |\mathbf{J}| d\xi d\eta d\zeta \\ &= \sum_{i=1}^{n_{ip}} \begin{bmatrix} N_1 & 0 & 0 \\ 0 & N_1 & 0 \\ 0 & 0 & N_1 \\ \vdots & \vdots & \vdots \\ \vdots & \vdots & \vdots \\ N_{n_n} & 0 & 0 \\ 0 & N_{n_n} & 0 \\ 0 & 0 & N_{n_n} \end{bmatrix}_i \begin{bmatrix} \alpha_b \sum_{k=1}^{n_n} \frac{\partial N_k}{\partial x} p_k \\ \alpha_b \sum_{k=1}^{n_n} \frac{\partial N_k}{\partial y} p_k \\ -\gamma_b + \alpha_b \sum_{k=1}^{n_n} \frac{\partial N_k}{\partial z} p_k \end{bmatrix}_i |\mathbf{J}|_i w_i \end{aligned} \quad (\text{C.10})$$

C.2.2 Surface force

If forces act on surface $\xi=\pm 1$

$$\mathbf{F}_s^e = \iint_S \mathbf{N}^T \mathbf{T} dS = \int_{-1}^1 \int_{-1}^1 \mathbf{N}^T \mathbf{T} A \, d\eta \, d\zeta = \sum_{i=1}^{n_{ipa}} (\mathbf{N}^T \mathbf{T} A)_i \mathbf{w}_i, \quad \mathbf{A} = \begin{vmatrix} \mathbf{i} & \mathbf{j} & \mathbf{k} \\ \frac{\partial x}{\partial \eta} & \frac{\partial y}{\partial \eta} & \frac{\partial z}{\partial \eta} \\ \frac{\partial x}{\partial \zeta} & \frac{\partial y}{\partial \zeta} & \frac{\partial z}{\partial \zeta} \end{vmatrix} \quad (\text{C.11})$$

If forces act on surface $\eta=\pm 1$

$$\mathbf{F}_s^e = \iint_S \mathbf{N}^T \mathbf{T} dS = \int_{-1}^1 \int_{-1}^1 \mathbf{N}^T \mathbf{T} A \, d\xi \, d\zeta = \sum_{i=1}^{n_{ipa}} (\mathbf{N}^T \mathbf{T} A)_i \mathbf{w}_i, \quad \mathbf{A} = \begin{vmatrix} \mathbf{i} & \mathbf{j} & \mathbf{k} \\ \frac{\partial x}{\partial \xi} & \frac{\partial y}{\partial \xi} & \frac{\partial z}{\partial \xi} \\ \frac{\partial x}{\partial \zeta} & \frac{\partial y}{\partial \zeta} & \frac{\partial z}{\partial \zeta} \end{vmatrix} \quad (\text{C.12})$$

If forces act on surface $\zeta=\pm 1$

$$\mathbf{F}_s^e = \iint_S \mathbf{N}^T \mathbf{T} dS = \int_{-1}^1 \int_{-1}^1 \mathbf{N}^T \mathbf{T} A \, d\xi \, d\eta = \sum_{i=1}^{n_{ipa}} (\mathbf{N}^T \mathbf{T} A)_i \mathbf{w}_i, \quad \mathbf{A} = \begin{vmatrix} \mathbf{i} & \mathbf{j} & \mathbf{k} \\ \frac{\partial x}{\partial \xi} & \frac{\partial y}{\partial \xi} & \frac{\partial z}{\partial \xi} \\ \frac{\partial x}{\partial \eta} & \frac{\partial y}{\partial \eta} & \frac{\partial z}{\partial \eta} \end{vmatrix} \quad (\text{C.13})$$

C.2.3 Initial stress induced body force

$$\mathbf{F}_{\sigma_0}^e = -\iiint_{\Omega_e} \mathbf{B}^T \boldsymbol{\sigma}_0' \, dx \, dy \, dz = -\int_{-1}^1 \int_{-1}^1 \int_{-1}^1 \mathbf{B}^T \boldsymbol{\sigma}_0' |\mathbf{J}| \, d\xi \, d\eta \, d\zeta = -\sum_{i=1}^{n_{ip}} [\mathbf{B}^T \boldsymbol{\sigma}_0' |\mathbf{J}|]_i \mathbf{w}_i \quad (\text{C.14})$$

where

$$\boldsymbol{\sigma}_0' = \begin{Bmatrix} \sigma_H'(z, t_0) \\ \sigma_h'(z, t_0) \\ \sigma_v'(z, t_0) \\ 0 \\ 0 \\ 0 \end{Bmatrix} \quad (\text{C.15})$$

Nodal displacement \mathbf{u} is related to element stiffness matrix and element node force through the following equation

$$\mathbf{K}^e \mathbf{u}^e = \mathbf{F}_f^e \quad (\text{C.16})$$

APPENDIX D

FINITE ELEMENT FORMULATION OF 3D TRANSIENT FLUID FLOW MODEL

The finite element formulation for a 3D transient fluid flow model is⁵³

$$\mathbf{K}_p^e \mathbf{p}^e + \mathbf{P}_M^e \frac{\partial \mathbf{p}^e}{\partial t} = \mathbf{q}^e \quad (\text{D.1})$$

where

$$\mathbf{K}_p^e = \iiint_{\Omega_e} \mathbf{T}_T^T \mathbf{K}_K \mathbf{T}_T dx dy dz \quad (\text{D.2})$$

$$\mathbf{P}_M^e = \iiint_{\Omega_e} \frac{\phi C_t}{B_f} \mathbf{N}^T \mathbf{N} dx dy dz \quad (\text{D.3})$$

in which

$$\mathbf{T}_T = \begin{bmatrix} \frac{\partial N_1}{\partial x} & \frac{\partial N_2}{\partial x} & \dots & \frac{\partial N_{n_n}}{\partial x} \\ \frac{\partial N_1}{\partial y} & \frac{\partial N_2}{\partial y} & \dots & \frac{\partial N_{n_n}}{\partial y} \\ \frac{\partial N_1}{\partial z} & \frac{\partial N_2}{\partial z} & \dots & \frac{\partial N_{n_n}}{\partial z} \end{bmatrix} = \mathbf{J}^{-1} \begin{bmatrix} \frac{\partial N_1}{\partial \xi} & \frac{\partial N_2}{\partial \xi} & \dots & \frac{\partial N_{n_n}}{\partial \xi} \\ \frac{\partial N_1}{\partial \eta} & \frac{\partial N_2}{\partial \eta} & \dots & \frac{\partial N_{n_n}}{\partial \eta} \\ \frac{\partial N_1}{\partial \zeta} & \frac{\partial N_2}{\partial \zeta} & \dots & \frac{\partial N_{n_n}}{\partial \zeta} \end{bmatrix} \quad (\text{D.4})$$

$$\mathbf{K}_K = \begin{bmatrix} \frac{k_x}{\mu_f B_f} & 0 & 0 \\ 0 & \frac{k_y}{\mu_f B_f} & 0 \\ 0 & 0 & \frac{k_z}{\mu_f B_f} \end{bmatrix} \quad (\text{D.5})$$

The Jacobian matrix \mathbf{J} is

$$\mathbf{J} = \begin{bmatrix} \frac{\partial x}{\partial \xi} & \frac{\partial y}{\partial \xi} & \frac{\partial z}{\partial \xi} \\ \frac{\partial x}{\partial \eta} & \frac{\partial y}{\partial \eta} & \frac{\partial z}{\partial \eta} \\ \frac{\partial x}{\partial \zeta} & \frac{\partial y}{\partial \zeta} & \frac{\partial z}{\partial \zeta} \end{bmatrix} = \begin{bmatrix} \frac{\partial N_1}{\partial \xi} & \frac{\partial N_2}{\partial \xi} & \dots & \dots & \frac{\partial N_{n-1}}{\partial \xi} & \frac{\partial N_n}{\partial \xi} \\ \frac{\partial N_1}{\partial \eta} & \frac{\partial N_2}{\partial \eta} & \dots & \dots & \frac{\partial N_{n-1}}{\partial \eta} & \frac{\partial N_n}{\partial \eta} \\ \frac{\partial N_1}{\partial \zeta} & \frac{\partial N_2}{\partial \zeta} & \dots & \dots & \frac{\partial N_{n-1}}{\partial \zeta} & \frac{\partial N_n}{\partial \zeta} \end{bmatrix} \begin{bmatrix} x_1 & y_1 & z_1 \\ x_2 & y_2 & z_2 \\ \vdots & \vdots & \vdots \\ \vdots & \vdots & \vdots \\ x_{n-1} & y_{n-1} & z_{n-1} \\ x_n & y_n & z_n \end{bmatrix} \quad (\text{D.6})$$

\mathbf{q}^e may include the effect of gravity and boundary flux.

$$\mathbf{q}^e = \mathbf{q}_g^e + \mathbf{q}_f^e \quad (\text{D.7})$$

The gravity part of \mathbf{q}^e is

$$\mathbf{q}_g^e = - \iiint_{\Omega_e} \mathbf{T}_T^T \mathbf{K}_K \mathbf{T}_T \gamma_f H dx dy dz \quad (\text{D.8})$$

If flow through surface $\xi = \pm 1$

$$\mathbf{q}_f^e = \iint_S \mathbf{N}^T \mathbf{v}_f dS = \int_{-1}^1 \int_{-1}^1 \mathbf{N}^T \mathbf{v}_f A d\eta d\zeta = \sum_{i=1}^{n_{psa}} (\mathbf{N}^T \mathbf{v}_f A)_i w_i, \quad A = \begin{vmatrix} \mathbf{i} & \mathbf{j} & \mathbf{k} \\ \frac{\partial x}{\partial \eta} & \frac{\partial y}{\partial \eta} & \frac{\partial z}{\partial \eta} \\ \frac{\partial x}{\partial \zeta} & \frac{\partial y}{\partial \zeta} & \frac{\partial z}{\partial \zeta} \end{vmatrix} \quad (\text{D.9})$$

If flow through surface $\eta = \pm 1$

$$\mathbf{q}_f^e = \iint_S \mathbf{N}^T \mathbf{v}_f dS = \int_{-1}^1 \int_{-1}^1 \mathbf{N}^T \mathbf{v}_f A d\xi d\zeta = \sum_{i=1}^{n_{psa}} (\mathbf{N}^T \mathbf{v}_f A)_i w_i, \quad A = \begin{vmatrix} \mathbf{i} & \mathbf{j} & \mathbf{k} \\ \frac{\partial x}{\partial \xi} & \frac{\partial y}{\partial \xi} & \frac{\partial z}{\partial \xi} \\ \frac{\partial x}{\partial \zeta} & \frac{\partial y}{\partial \zeta} & \frac{\partial z}{\partial \zeta} \end{vmatrix} \quad (\text{D.10})$$

If flow through surface $\zeta = \pm 1$

$$\mathbf{q}_f^e = \iint_S \mathbf{N}^T \mathbf{v}_f dS = \int_{-1}^1 \int_{-1}^1 \mathbf{N}^T \mathbf{v}_f A d\xi d\eta = \sum_{i=1}^{n_{ipa}} (\mathbf{N}^T \mathbf{v}_f A)_i \mathbf{w}_i, \mathbf{A} = \begin{vmatrix} \mathbf{i} & \mathbf{j} & \mathbf{k} \\ \frac{\partial x}{\partial \xi} & \frac{\partial y}{\partial \xi} & \frac{\partial z}{\partial \xi} \\ \frac{\partial x}{\partial \eta} & \frac{\partial y}{\partial \eta} & \frac{\partial z}{\partial \eta} \end{vmatrix} \quad (\text{D.11})$$

APPENDIX E

DERIVATION OF TENSILE STRESS INDUCED SANDING ONSET PREDICTION MODEL AFTER SHEAR FAILURE

E.1 Fluid flow model

If we assume fluid density and pressure satisfies a power-law relation³⁹⁻⁴⁰, see equation (E.1), and assume steady state flow from reservoir boundary to perforation tunnel/wellbore or perforation tip, the pressure distribution around a cavity is derived.

$$\rho_f = \gamma p^{m_d} \quad (E.1)$$

For open-hole wellbore or perforation tunnel, the pressure distribution is

$$p^{m_d+1} = \left[(P_e^{m_d+1} - P_{wf}^{m_d+1}) \frac{\ln x}{\ln \frac{R_e}{R_w}} + P_{wf}^{m_d+1} \right] \quad (E.2)$$

For perforation tip, the pressure distribution is

$$p^{m_d+1} = \left[(P_e^{m_d+1} - P_{wf}^{m_d+1}) \left(1 - \frac{R_w}{r}\right) + P_{wf}^{m_d+1} \right] \quad (E.3)$$

E.2 Stress model

The equilibrium equation is

$$\frac{\partial \sigma'_r}{\partial r} + C_N \frac{\sigma'_r - \sigma'_\theta}{r} + \alpha \frac{\partial p(r, t)}{\partial r} = 0 \quad (E.4)$$

where $C_N=1$ for wellbore or perforation tunnel, $C_N=2$ for perforation tip.

If tangential stress is maximum principal stress and radial stress is minimum principal stress, using Mohr-Coulomb criterion at failure, yields

$$\sigma'_r - \sigma'_\theta = -\frac{2\sin\phi_f}{1 - \sin\phi_f} (\sigma'_r + S_o \cot\phi_f) \quad (\text{E.5})$$

The inner boundary condition is

$$\sigma'_r = (1 - \alpha_b) P_{wf} \quad (\text{E.6})$$

The radial stress solution is

For perforation tunnel or open hole

$$\sigma'_r = -\alpha_b r^m \int_{R_w}^r \frac{\partial p(r, t)}{\partial r} r^{-m} dr + C_{hc} r^m - S_o \cot\phi_f \quad (\text{E.7})$$

where

$$m = \frac{2\sin\phi_f}{1 - \sin\phi_f} \quad (\text{E.8})$$

$$C_{hc} = \frac{S_o \cot\phi_f + (1 - \alpha_b) P_{wf}(t)}{R_w^m} \quad (\text{E.9})$$

For perforation tip

$$\sigma'_r = -\alpha_b r^{2m} \int_{R_w}^r \frac{\partial p(r, t)}{\partial r} r^{-2m} dr + C_{hs} r^{2m} - S_o \cot\phi_f \quad (\text{E.10})$$

where

$$C_{hs} = \frac{S_o \cot\phi_f + (1 - \alpha_b) P_{wf}(t)}{R_w^{2m}} \quad (\text{E.11})$$

E.3 Tensile stress induced sanding onset model

The sanding onset condition is

$$\left. \frac{d\sigma'_r}{dr} \right|_{r=R_w} \leq 0 \quad (\text{E.12})$$

which indicates that sanding occurs when tensile stress is induced near the cavity.

Substituting (E.7) and (E.10) into (E.12), yields

For perforation tunnel or open hole

$$\alpha_b \left. \frac{\partial p(r, t)}{\partial r} \right|_{r=R_w} = \frac{2\sin\phi_f}{1-\sin\phi_f} \frac{S_o \cot\phi_f + (1-\alpha_b)P_{wf}(t)}{R_w} \quad (\text{E.13})$$

If α_b is one, then

$$\left. \frac{\partial p(r, t)}{\partial r} \right|_{r=R_w} = \frac{C_o}{R_w} \quad (\text{E.14})$$

Substituting (E.2) into (E.14), yields

$$C_o \ln \frac{R_e}{R_w} = \frac{1}{m_d + 1} \left[\frac{P_e^{m_d+1} - P_{wf}^{m_d+1}}{P_{wf}^{m_d}} \right] \quad (\text{E.15})$$

For perforation tip,

$$\alpha_b \left. \frac{\partial p(r, t)}{\partial r} \right|_{r=R_w} = 2 \frac{2\sin\phi_f}{1-\sin\phi_f} \frac{S_o \cot\phi_f + (1-\alpha_b)P_{wf}(t)}{R_w} \quad (\text{E.16})$$

If α_b is one, then

$$\left. \frac{\partial p(r, t)}{\partial r} \right|_{r=R_w} = \frac{2C_o}{R_w} \quad (\text{E.17})$$

Substituting (E.3) into (E.17), yields

$$2C_o = \frac{1}{m_d + 1} \left[\frac{P_e^{m_d+1} - P_{wf}^{m_d+1}}{P_{wf}^{m_d}} \right] \quad (\text{E.18})$$

VITA

Name: Xianjie Yi

Born: September 26 1974
Gong'an, Hubei, P. R. China

Permanent Address: No. 34 E. Heping Rd.
Nanchong, Sichuan 637000
P. R. China

Education: Texas A&M University, College Station, Texas, USA
Doctor of Philosophy Degree in Petroleum Engineering
August 2003
Southwest Petroleum Institute, Nanchong, Sichuan, China
Master of Science Degree in Petroleum Engineering
July 1999
Southwest Petroleum Institute, Nanchong, Sichuan, China
Bachelor of Science Degree in Petroleum Engineering
July 1996

Experience: Intern, Well Services, Schlumberger, Sugar Land, TX, USA
June 2002-January 2003